Modeling nanoscale transport phenomena: Implications for the continuum

Ganesh Balasubramanian

Dissertation submitted to Virginia Polytechnic Institute and State University
in partial fulfillment of the requirements for the degree of

Doctor of Philosophy
in
Engineering Mechanics

Ishwar K. Puri, Chairman
Romesh C. Batra
Scott T. Huxtable
Roop L. Mahajan
Saad A. Ragab

April 20, 2011
Blacksburg, Virginia

Keywords: Nanoscale transport, molecular dynamics, multiscale simulation

Modeling nanoscale transport phenomena: Implications for the continuum

Ganesh Balasubramanian

Abstract

Transport phenomena at the nanoscale can differ from that at the continuum because the large surface area to volume ratio ($\approx 10^8$ m^{-1}) significantly influences material properties. While the modeling of many such transport processes have been reported in the literature, a few examples exist that integrate molecular approaches into the more typical macroscale perspective. This thesis extends the understanding of nanoscale transport governed by charge, mass and energy transfer, comparing these phenomena with the corresponding continuum behavior where applicable. For instance, molecular simulations enable us to predict the solvation structure around ions and describe the diffusion of water in salt solutions. In another case, we find that in the absence of interfacial effects, the stagnation flow produced by two opposing nanojets can be suitably described using continuum relations. We also examine heat conduction within solids of nanometer dimensions due to both the ballistic propagation of lattice vibrations in small confined dimensions and a diffusive behavior that is observed at larger length scales. Our simulations determine the length dependence of thermal conductivity for these cases as well as effects of isotope substitution in a material. We find that a temperature discontinuity at interfaces between dissimilar materials arises due to interfacial thermal resistance. We successfully incorporate these interfacial nanoscale effects into a continuum model through a modified heat conduction approach and also by a multiscale computational scheme. Finally, our efforts at integrating research with education are described through our initiative for developing and implementing a nanotechnology module for freshmen, which forms the first step of a spiral curriculum.

Dedicated to my alma maters,

South Point High School, Jadavpur University & Virginia Tech

Acknowledgments

I am indeed very fortunate to have Professor Puri as my research advisor and mentor. He is truly a smart researcher, a sincere professional, an excellent philosopher and guide, but above all a great human being, second to none. I am indebted to the intellectually stimulating discussions we have had that immensely contributed to my research, some of which are presented in my thesis. I am grateful for his inspiration and encouragement towards my academics, community service, and personal life. Though words cannot express my gratitude for his role in my life, I thank him from the bottom of my heart.

I thank Professors Batra, Huxtable, Mahajan, and Ragab for serving on my committee and providing useful feedback about my research. Their accomplishments have always motivated me to perform better and solve challenging problems that would be useful to the scientific community.

Professor Hajj's support and belief in my abilities have been instrumental for me throughout my graduate education. It has always been a pleasure to interact with Professor Lohani, who has educated me about the subtle issues associated with academic life and research. Professor Murad is a great mentor and his contribution to my research is enormous; he has taught me the salient features of molecular simulations that only a specialist can ever know. I thank the many collaborators who have shared their time and expertise, enhancing the very interesting research projects of this dissertation. I extend my appreciation to all the VT professors who have taught me the various scientific and engineering subjects.

The members of the ESM-MuRG team that I have known throughout the years deserve my gratitude. While my time with Soumik, Sayan, Ashok, and Anindya was brief, I am still grateful for their introduction to the various facets of graduate life. I thank my current

labmates, Monrudee, Suvojit, Ravi, and Souvik, for all of their help and support at every time of need. They have been great friends. Thanks also to my JU mentors, Professors Swarnendu Sen, Achintya Mukhopadhyay, and Koushik Ghosh, for their confidence in my competency. I am grateful to Professor H. P. Mazumdar at ISI Kolkata for his faith in my abilities to be a scientific researcher. My teachers in high school, Parthasarathi Mukhopadhyay and Bhaskar Bose, were two individuals who sowed the seed behind my idea of becoming a future academician.

Life away from home can become difficult. But members of the ESM family have made Blacksburg my home away from home. Anne-Marie has always been a great support and our strong friendship has helped me through difficult times. Lisa and Linda are two wonderful people who made my life easier than it could ever be. Pat and Mark have always helped me with technical issues that I have faced. I would like to especially thank Tim for his magnificent assistance with supercomputing, including his going out of the way at times to get my programs running, that has enabled my research to be completed in good time.

The Graduate School has made a profound impact on my life. The recognition I have received for my participation in the university activities has humbled me. I thank Dean DePauw for her encouragement to me and all the graduate students on campus, Monika and Lauren for facilitating with events, and the Graduate Student Assembly and Alpha Epsilon Lambda, and its officers for enhancing my leadership and teamwork skills through all of our work together. Great thanks also belong to Robert Mayorga, one of my dearest friends and confidantes, who has always stimulated me to "release the encapsulated value" of any activity that I am working on, as a sculptor puts all of his energy into chipping away at a block of marble to expose the beauty hidden within.

The Table Tennis Club at VT made it possible for me to continue with my recreation and passion for the sport. The many friends and well-wishers that I found here have made my stay in Blacksburg most enjoyable. Thanks to all the members of "Oakbridge-JU Association" for the Friday night gossips and dinners that always helped me unwind after a long week.

Friends are important, and thankfully I made so many of them. My closest friends included Grant, Tom, Mehdi, Giovanni, Mike, Mohsen, Pankaj-bhai, Gautam, Vasileios, Udit, Naik, Matt, Tridib-da, Saugata-da, Dulal, Hao-Hsiang, Shree, Amanda, Krishna, Abhra-da,

Seemant-bhai, Arjun, Cody, Chris, Keyes, Kohei, Oak and others, and my buddies in India, Soham, Shuvro, Souvik, Debmalya and others. Hopefully, someday I will join Facebook and not be the member of an extinct species!

My mother and father have sacrificed a lot to bring me up. My achievements have been, and will continue to be, a reflection of their love. Words of gratitude will never justify their contribution. I know they are very proud of me, and that gives me much happiness. My maternal uncles always wanted me to reach the uppermost echelons of the educated society. It feels great that their beliefs have come to fruition.

Tanumita has stood by me throughout thick and thin, kept me thoroughly focused on my goals, and supported me unconditionally. Her love, dedication, and encouragement give me strength everyday. I love her and look forward to our many wonderful years together.

GB

Blacksburg

04/2011

Thanks to all my collaborators:

- Jadavpur University
  - Professor Swarnendu Sen
- Science Applications International Corporation
  - Jennifer A. Tomlin, William P. Wong
- Technical University of Darmstadt
  - Professor Michael C. Böhm
  - Dr. Frédéric Leroy
- University of Illinois at Chicago
  - Professor Sohail Murad
- University of Tennessee at Knoxville
  - Professor Peter K. Liaw
  - Li Li
- Virginia Tech
  - Professors Scott W. Case, Daniel M. Dudek, Muhammad R. Hajj, Scott T. Huxtable, Vinod K. Lohani, Roop L. Mahajan, Saad A. Ragab
  - Dr. Soumik Banerjee
  - Mehdi Ghommem, Ravi Kappiyoor, Hao-Hsiang Liao, Nitin C. Shukla, Chun-Hsien Wu

Attribution

Professor Puri is my research advisor and committee chair. He provided guidance and support for all of the work presented in this dissertation, as well as contributing significantly with the written communication of the research.

Professor Murad provided guidance on the simulations of aqueous ionic solutions (Chapters 2 and 3), was involved with discussion of the results and writing. Ravi Kappiyoor assisted with setting up of the topology and molecular parameters.

Professor Ragab helped with the fundamentals of fluid dynamics and thermodynamics for the project on nanoscale jets (Chapter 4), and provided useful insight during our discussions on the results.

Professor Sen shared his idea for the investigation of rheology of fluid-particle suspensions (Chapter 5), and was involved in subsequent discussions.

Professor Böhm and Dr. Leroy contributed to the project on thermal conductivity reduction by isotope substitution (Chapter 6) through their idea and development of the analytical model, subsequent discussions and writing.

Professors Huxtable, Liaw, and the graduate students Hao-Hsiang Liao, Li Li, Nitin C. Shukla and Chun-Hsien Wu contributed to the experimental investigation of the thermal conductivity of Ni-Fe alloy (Chapter 7), and were involved with the writing part of their contribution to the project.

Dr. Banerjee mentored me on atomistic simulations and contributed to the comparison of the molecular dynamics results with continuum analysis for the research on interfacial heat transfer (Chapter 8).

Professors Case, Lohani, Mahajan shared their vision about nanotechnology undergradu-

ate education (Chapter 10). Professor Lohani guided with the development, implementation and assessment of the module as well as with the writing.

Professor Hajj, Mehdi Ghommem, Jennifer A. Tomlin and William P. Wong collaborated on research involving thermochemical energy storage in salt hydrates, which is not part of this dissertation. Likewise, I collaborated with Professor Dudek and Ravi Kappiyoor on elastomechanical properties of resilin, not part of this dissertation.

Copyright permissions from the publishers of the different journals to use the contents of my published archival articles are available with the dissertation.

Contents

List of Figures

List of Tables

Chapter 1

Introduction

¨ There's Plenty of Room at the Bottom: An Invitation to Enter a New Field of Physics ¨
— Richard P. Feynman

1.1 Nanoscale transport: The bottoms-up approach

Research in nanotechnology has grown by leaps and bounds over the last decade, and with that questions have emerged about suitably employing the knowledge gained from scientific explorations at the atomistic scale to the utilization of mankind. Unlike the age old tradition of trying to improve things top-down, and in turn squandering useful resources, as Michelangelo did when chipping away the pieces of a rock to carve a beautiful sculpture, I believe that the approach should be bottoms-up; assimilating the salient details at the nanoscale and implementing them for a cohesive benefit at the continuum is the way to go. My doctoral research, which involves investigation of charge, mass and thermal transport at the nanoscale, as well as the development of a multiscale model to understand heat transfer in mesoscale devices by coupling together the fundamentals of nanoscale interfacial effects with a continuum model, has been one such attempt. Learning the mechanism from the fundamentals to the bulk, for instance, how molecules of water can coalesce to form a stable droplet, can have path-breaking insinuations towards solving several scientific and engineering challenges currently facing us.

Atoms are the elementary forms of matter. Their chemical orientation and how they

interact amongst themselves determines the phase (solid/liquid/gas) and characterizes their capability for significant transport mechanisms. While strong interatomic bonds in solids fix the relative positions of the atoms even in absence of external forces, the weak forces of interactions and large interatomic distances in fluids eliminate the possibility of such a coherent arrangement.

When system sizes are reduced to the nanoscale, the surface area to volume ratio is typically a factor of 10^6 higher than that at the continuum. Thus, transport processes across the boundary and interfacial surfaces of contact between similar or dissimilar materials play a significant role in governing the overall transport. Hence, it is important to understand these phenomena from a fundamental perspective. While theoretical and experimental investigations exist for many such cases, molecular dynamics simulations, based on the classical Newton's laws of motion, are able to provide a basis for understanding nanoscale transport mechanisms, and means to suitably incorporate them into a macroscale model to characterize the processes across different length scales.

For example, in order to understand and devise long-term thermal storage strategies, salt hydrates are considered as potential candidates for accumulating solar heat during the hot summer months and releasing the collected energy to warm homes in winter (N'Tsoukpoe et al., 2009). Salt hydrates dissociate into anhydrous salts (or lower hydrates) and water vapor upon heating. An anhydrous salt has relatively higher energy content than its hydrated counterpart and can be stably stored over long durations and transported at ambient temperatures. In their anhydrous form, these salts are generally hygroscopic, and absorption and adsorption of water molecules can occur even at room temperature, leading to a usable thermal release of the stored energy. Thermal energy can be released by allowing water vapor to flow across the anhydrous salt, which transforms its chemically stored heat into a perceivable form. The fundamental roots for these energy conversion processes can be ascribed to the hydration characteristics of the ionic salts. The interactions between ions and polar water molecules forming coordination structures release the enthalpy of hydration (heat release), while energy supplied to break these bonds can be stored by dehydrating them (heat storage). Hence a molecular level understanding of chemical transport in such ionic salt solutions can help predict their capabilities in flow based energy applications.

Atoms in a solid oscillate about their mean positions when energy is supplied to them. This initiates a thermal wave or lattice vibration, also called a phonon, that transports (or conducts) energy through the medium (Chen, 2005; Nitzan, 2007). However, in fluids, due to absence of periodic lattice structures, phonons do not exist and hence heat transfer occurs through random atom-atom collisions only. Temperature is proportional to the average kinetic energy of the atoms (or molecules). It is essential to remember that in fluid flows only the thermal velocity of the atoms (due to oscillatory motion of atoms and not that due to bulk translation of the fluid) contribute towards the molecular kinetic energies (and hence temperature) of the corresponding system, and should not be misinterpreted with the kinetic energy of the flow due to momentum flux. Constitutive relations like Fourier's law of heat conduction are employed to describe thermal transport at the continuum (Incropera, 2007) level. Such empirical models depend only on the bulk material properties like density, specific heat, thermal conductivity, but not on the mechanisms at the atomistic scale.

When system sizes are shrunk to nanoscale dimensions, the length scales are comparable with the mean free path of the energy carriers, phonons and electrons (in conductors) (Cahill et al., 2003; Chen, 2005; Heyes and March, 1996). Phonons travel ballistically in such systems, but are subject to scattering at boundaries and interfaces, where they lose their energy, resulting in low thermal conductivities (Schelling et al., 2002, 2004); at larger length scales, scattering phenomena between the energy carriers occurs throughout the material, and a diffusive transport mechanism is predominant there (Cahill et al., 2003). At the contact surface between dissimilar materials, acoustic impedance (due to differences in density and sound speed) causes phonons traveling from one material to reflect or refract through the other material across the interface. This gives rise to interfacial thermal resistance and a temperature discontinuity is observed at the interface (Kapitza, 1941; Pollack, 1969; Swartz and Pohl, 1989). However, macroscale models are incapable of reproducing this interfacial temperature jump. Incorporating such temperature discontinuities at the interfaces of dissimilar materials into the overall thermal transport model and integrating its contribution towards the estimation of transport properties of a heterogeneous system is essential. It can provide strong insights into energy losses that occur in composite structures, like superlattices, and present constructive recommendations for thermal management in devices relevant

to thermoelectrics, power electronics, heat transfer fluids, drug targeting and thermal treatment (Antia et al., 2007; Cahill et al., 2003; Chen, 2000a, 2006; Chen et al., 2004; Chen, 2005; Darabi, 2002; Eastman et al., 2004; Majumdar, 2000; Pop, 2010; Poulikakos et al., 2003) etc.

1.2 Computational tool: Molecular Dynamics simulations

Computer experiments are fascinating in that tens of thousands of numerical investigations can be undertaken for any potential research problem with a favorable use of time and resources, a benefit that physical experimental setups cannot provide. Parametric studies of systems and transport phenomena can illuminate novel features that could be used for tuning material properties at the molecular level to impart significant influence at the continuum. Molecular dynamics (MD) simulations (Allen and Tildesley, 1987; Haile, 1997) have been successfully employed for investigations of static as well dynamic properties of a wide variety of nanoscale systems and transport phenomena (Malani et al., 2006, 2010; Maruyama and Kimura, 1999; Murad and Puri, 2007a,b, 2008a,b; Schelling et al., 2002). MD is a deterministic simulation technique that solves Newton's second law of motion for all individual atoms or molecules in the system and examines the time evolution of the system through relations for translation motion,

$$m\frac{\partial^2 r}{\partial t^2} = F = -\frac{\partial U}{\partial r} \tag{1.1}$$

where U is an interaction potential that describes the pairwise or multibody interactions between atoms and molecules. The basic constituents of a typical potential model are shown in Figure 1.1a.

The accuracy of MD simulations depends on the accuracies of the associated potential functions that are used. Therefore, the form of U must be carefully selected. Intermolecular interactions in liquid water can be modeled, for example, using the simple point charge (SPC) model of Berendsen et al. (1987) that specifies a three-site rigid water molecule that has polar charges assigned to each of its three atoms (hydrogen, hydrogen and oxygen) and a Lennard-Jones potential (Allen and Tildesley, 1987; Haile, 1997) between oxygen sites. Accurate modeling of solid atoms requires the incorporation of many-body interactions, such as a three-body interaction Stillinger-Weber (Stillinger and Weber, 1985), Tersoff potentials

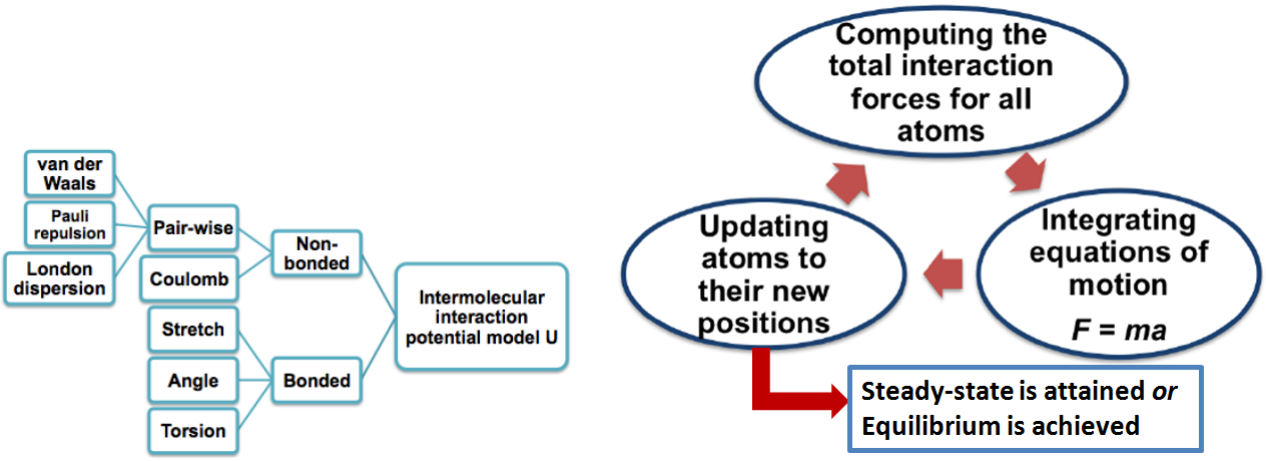

(a) (b)

Figure 1.1: (a) The different interaction forces that contribute to the potential model. (b) A typical simulation strategy in MD.

(Tersoff, 1988, 1989), etc. Solid-fluid and dissimilar solid-solid or fluid-fluid atom interactions can be represented through the empirical Lennard-Jones function with the parameters obtained through the Lorentz-Berthelot rule (Allen and Tildesley, 1987). MD is particularly advantageous in the case of solids, high-density fluids, such as gases under high pressure, or liquids, since the larger number of atoms or molecules in the system provides better statistics for averaging the bulk properties.

The basics of the computation scheme (Allen and Tildesley, 1987; Haile, 1997) include

- Setting up the simulation geometry and the assigning the set of potential functions and parameter values for the different materials in the system
- Defining a suitable ensemble that governs the macroscopic thermodynamic state of the system
- Equilibrating the system to a minimum energy configuration
- Computing the forces on the atoms, integrating the equations of motions and updating the atoms to the new positions (shown in Figure 1.1b)
- Calculating the static and/or dynamic properties as the system evolves over time

1.3 Research initiatives

The research investigations presented here provide some examples of nanoscale transport due to motion of charged ions and polar water molecules, movement of fluid molecules or mass transport, and thermal energy transfer within materials and across interfaces. The problems discussed are (Chapters 2 and 3) hydration of ions and diffusion of the solvent and solute in aqueous salt solutions, charge dominated phenomena, (Chapter 4) dynamics of impinging nanoscale jets, a fluid flow problem, (Chapters 5, 6 and 7) calculation of transport coefficients for fluids and solids, and (Chapters 8 and 9) interfacial thermal transport across interfaces of dissimilar materials, heat transfer related investigations. Each of the above chapters contains a brief review of the current literature and novel aspects of the presented research, followed by details of the simulation methodology and finally a discussion of the results, which includes comparison with earlier studies where applicable. Subsequently, the implementation of multiscale computational technique to model heat transfer in mesoscale devices is proposed and details of a heterogeneous computational scheme are discussed (Chapter 9).

In addition, initiatives taken to integrate research with education are presented (Chapter 10), where a novel concept for teaching emerging technologies like nanoscale science and engineering is described and the details of a curriculum, developed and implemented over several semesters of a large freshman engineering class, are discussed.

Chapter 2

Ionic hydration: Coordination behavior in aqueous salt solution

Equilibrium molecular dynamics simulations have been performed to examine the hydration characteristics of Mg^{2+} and SO_4^{2-} ions over a range of salt concentrations in the solution. While the hydration structure of the monatomic cation agrees with previous reports in the literature, the larger and more complex anion exhibits hitherto unreported novel coordination features. These result from its low charge density as well as the charge distribution over the five active sites. While the number of water molecules that hydrate the ions below the hydration limit is almost constant, this number rapidly reduces as the solution becomes saturated and ion-pairs are formed.

G. Balasubramanian, S. Murad, R. Kappiyoor and I. K. Puri, Chemical Physics Letters, 2011 (in press)

2.1 Motivation and objectives

The heat supplied to dehydrate salt hydrates (like magnesium sulfate heptahydrate $MgSO_4.7H_2O$) accumulates in the anhydrous salt once the coordinated water molecules are released (Balasubramanian et al., 2010b; van Essen et al., 2009). This form of thermochemical energy conversion can be used, for instance, for long-term thermal storage (N'Tsoukpoe et al., 2009). The capability of aqueous ionic salt solutions to store thermochemical energy depends upon their solvation characteristics (Malani et al., 2006; Mountain, 2007). The hydration structure of Mg^{2+} (Guardia et al., 1999; Obst and Bradaczek, 1996) and the polyatomic SO_4^{2-} (Cannon et al., 1994; Gao and Liu, 2004; Vchirawongkwin et al., 2007) ion is available in the literature. However, previous investigations have not comprehensively examined either the consequence of the formation of ion-pairs when the solution is saturated (the solubility of $MgSO_4$ is $\approx 21\%$ by weight at room temperature (Rodríguez Fernández-Alba, 2005)) or the effect of concentration on the structure of either hydrated ion. We address these issues by investigating the molecular level changes in an aqueous $MgSO_4$ solution as its concentration is varied. We also employ an atomistic model for SO_4^{2-} rather than the primitive model often used. This allows us to determine the effects of the charge distribution in the SO_4^{2-} ion on hydration and ion-pair formation.

2.2 Simulation details

Equilibrium molecular dynamics (MD) simulations (Allen and Tildesley, 1987; Haile, 1997) are employed to study a 7 nm $\times$ 7 nm $\times$ 7 nm cuboid (x-y-z) that contains an equal number of randomly distributed Mg^{2+} and SO_4^{2-} ions, with water molecules filling the remainder of the space. The density of the system is adjusted to reflect the composition of the specific solution being simulated. The solution composition at different salt concentrations is presented in Table 2.1. The system is initialized at 300 K with a Maxwell distribution of the molecular velocities. We perform a series of canonical (NVT) simulations over 10^6 timesteps using the leap-frog integrator and a timestep of 0.002 picoseconds (ps). The system temperature is maintained constant at 300 K during each simulation by rescaling the molecular velocities after every 0.1 ps.

Table 2.1: Number of ions and water molecules present in the system at different salt concentrations (weight%) of the solution.

Concentration (weight %)	Number of molecules/ions			Concentration (weight %)	Number of molecules/ions		
	Water	Mg^{2+}	SO_4^{2-}		Water	Mg^{2+}	SO_4^{2-}
0.00	11410	0	0	7.22	10736	125	125
0.12	11406	2	2	8.61	10653	150	150
0.35	11385	6	6	10.04	10490	175	175
0.59	11363	10	10	11.43	10358	200	200
1.17	11315	20	20	16.91	9854	300	300
1.75	11254	30	30	22.24	9353	400	400
2.33	11200	40	40	27.49	8819	500	500
2.91	11150	50	50	32.66	8272	600	600
3.48	11114	60	60	37.48	7809	700	700
4.64	10982	80	80	42.09	7359	800	800
5.79	10877	100	100	50.84	6466	1000	1000

The MD simulations are based on the parallel GROMACS code (Hess et al., 2008; van der Spoel et al., 2005). The VMD (Humphrey et al., 1996) and RasMol (Sayle and Milnerwhite, 1995) codes are used to postprocess the results. The "flexible" simple point charge (SPC) potential that we use to model water molecules (Berendsen et al., 1981; Chandrasekhar and Jorgensen, 1982; Guardia and Padro, 1990; Jorgensen et al., 1983; Mizan et al., 1994; Oostenbrink et al., 2004) is known to realistically represent experimental geometries, energies of ion-water complexes and energies of solvation (Chandrasekhar and Jorgensen, 1982; Jorgensen et al., 1983). The parameters (σ_{ij} and ϵ_{ij}) used for the nonbonded pairwise Lennard-Jones and charge (q_i, q_j) interactions (potential U_{ij} between atoms i and j) of the Mg^{2+} and SO_4^{2-} sites (separated by distance r_{ij}) correctly reproduce their free enthalpies of solvation in cyclohexane and water (Oostenbrink et al., 2004).

$$U_{ij} = 4\epsilon_{ij}\left[(\frac{\sigma_{ij}}{r_{ij}})^{12} - (\frac{\sigma_{ij}}{r_{ij}})^{6}\right] + \frac{q_i q_j}{r_{ij}} \tag{2.1}$$

Table 2.2 lists these parameters as well as the bond and angle interaction potentials for all species. Compared with a rigid water model (Berendsen et al., 1981), the flexibility in the bond and angle interactions (Oostenbrink et al., 2004) provides a more accurate representation of orientational correlation times, improved dielectric behavior, and more stable hydration shells around ions (Guardia and Padro, 1990; Mizan et al., 1994). Lorentz-Berthelot mixing rules (Allen and Tildesley, 1987) are used to model cross-interactions. All simulations use a constant cut-off distance of 1.5 nm. Electrostatic interactions are handled using a Coulombic potential function and long range corrections are accounted for by employing a larger cut-off radius ($>$ 1.0 nm) for the pairwise interactions. In discussing our results, we define the hydration limit as the concentration at which ion-pairs begin to form and the solubility limit as the concentration above which only ion-pairs exist.

Table 2.2: The nonbonded (Lennard-Jones and Coulomb) and bonded (bonds, angles) interaction parameters for Mg^{2+}, SO_4^{2-} (Oostenbrink et al., 2004) and water that is modeled using the SPC potential (Berendsen et al., 1981; Oostenbrink et al., 2004).

Sites	σ_{ij} (nm)	ϵ_{ij} (kJ mol^{-1})	q(e)
Mg^{2+}	0.1933	0.3126	+2.000
S(in SO_4^{2-})	0.3308	1.9043	+0.540
O(in SO_4^{2-})	0.2626	1.7245	-0.635
OW(in H_2O)	0.3166	0.6503	-0.820
H(in H_2O)	0.0000	0.0000	+0.410
Bond-type	Interaction function	r_0 (nm)	k_b
S-O	$\frac{1}{4}k_b(r^2 - {r_0}^2)^2$	0.150	8.37×10^6 kJ mol^{-1} nm $^{-4}$
OW-H	$\frac{1}{4}k_b(r - r_0)^2$	0.100	3.45×10^5 kJ mol^{-1} nm $^{-2}$
Angle-type	Interaction function	θ_0 (degrees)	k_θ
O-S-O	$\frac{1}{2}k_\theta(cos\theta - cos\theta_0)^2$	109.50	520.00 kJ mol^{-1}
H-OW-H	$\frac{1}{4}k_\theta(\theta - \theta_0)^2$	109.47	383.00 kJ mol^{-1} rad^{-2}

2.3 Outcomes of the investigation

We investigate the changes in the structure of the hydrated ions as the salt concentration is increased from 0-50.84 weight%. Figure 2.1a presents changes in the radial distribution function (RDF) g(r) for Mg^{2+}- water, and coordination number (CN) of water around the cation (Mg^{2+}) as the salt concentration is varied. The RDF of an ion with water is actually the RDF of the ion with the oxygen site (OW) of water. CN is typically determined by calculating how many OW sites, hence water molecules, lie within the given radius extending from the ion. The dominant $g_{MgOW}(r)$ peak at 0.195 nm represents the location of the first hydration shell as can be seen in Figure 2.1b. This is followed by a region with zero $g_{MgOW}(r)$ where there is an absence of water molecules. Thereafter, the $g_{MgOW}(r)$ again increases to a value above unity ($\approx$ 1.88 - 1.46) at approximately 0.415 nm for salt concentrations between 1.16 - 50.84 weight% respectively.

The negatively charged oxygen sites of the water molecules in the first hydration shell are oriented towards the cation. This results in a net positive charge on the outside of this shell due to the hydrogen sites of water. This attracts other water molecules in the vicinity towards the shell. As a consequence, the $g_{MgOW}(r)$ increases above unity to produce the weak second hydration shell. It is difficult to visualize this weak second hydration shell since the $g_{MgOW}(r)$ peak is small, but it is evident upon observation of the CN_{MgOW} curve shown in Figure 2.1(a). While the CN_{MgOW} curve has a flat shoulder-like region or plateau after the first $g_{MgOW}(r)$ peak, signifying a strongly bound first hydration shell and lack of any water molecules in its vicinity, after the second $g_{MgOW}(r)$ peak, it has a somewhat weak shoulder around 0.425 - 0.450 nm, especially for the dilute solutions.

With increasing concentrations, the value of the first $g_{MgOW}(r)$ peak decreases from 18.76 for a 1.16 weight% $MgSO_4$ solution to 17.77 for a 16.91% solution to 16.98 at 50.84 weight%. This decrease in g(r) corresponds to changes in the cation hydration structure, as we will discuss later. With increasing salt concentration, the CN_{MgOW}, calculated as the integral of the $g_{MgOW}(r)$, decreases from a value of 6 at lower concentrations, which is in agreement with the literature (Guardia et al., 1999; Obst and Bradaczek, 1996), to $\approx$ 3 for a 50.84 weight% $MgSO_4$ solution. Figures 2.1b, c and d present the corresponding structural changes in the

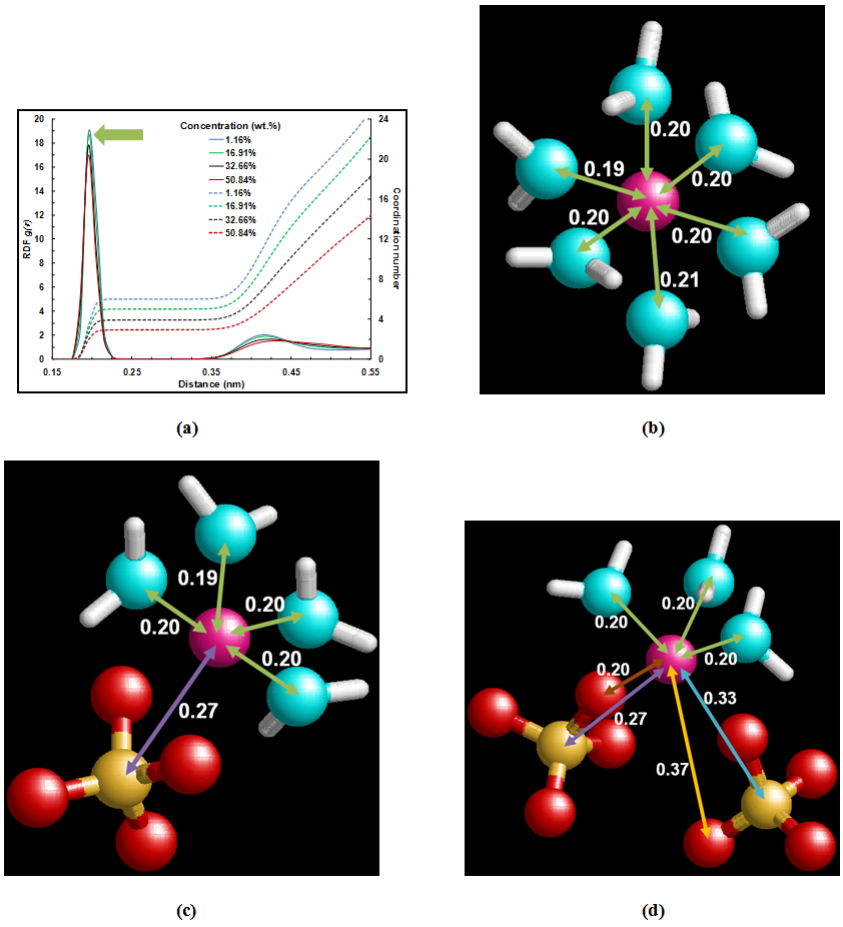

Figure 2.1: (a) The radial distribution function (RDF), drawn with continuous lines, and coordination number, drawn with dashed lines, for Mg^{2+} and water at different salt concentrations. The locations of the various species around Mg^{2+} for (b) 1.16%, (c) 32.66% and (d) 50.84% salt concentrations by weight are represented in nm (nanometer) using the following color scheme: (i) the green arrow labels the distance between a Mg^{2+} ion and a coordinating water molecule and corresponds to the peak RDF in Figure 2.1a denoting the first hydration shell; (ii) purple and blue arrows label the distances between Mg^{2+} and S(of SO_4^{2-}) and, respectively, correspond to the two peaks in the RDF in Figure 2.2a) for the two ion-pair shells; (iii) brown and yellow arrows label the distances between Mg^{2+} and O(of SO_4^{2-}) and, respectively, correspond to the two peaks in the RDF in Figure 2.2c.

hydration of the Mg^{2+} ion as the salt concentration varies. At a 1.16% salt concentration (Figure 2.1b), six water molecules create a cage around the cation to form the first hydration shell. Increasing the concentration leads to ion-pair formation, as shown in Figure 2.1c. Thus, the proximity of Mg^{2+} to SO_4^{2-} at ≈ 0.265 nm leads to the formation of hydrated ion-pairs which lowers the CN_{MgOW} in more concentrated solutions, as observed earlier in Figure 2.1a. As the salt concentration increases much above its solubility limit to about 50%, almost all ions are present as ion-pairs, as shown in Figure 2.1d. Here, we show as an example, a cation surrounded by two anions. It clearly reveals that ion-pair formation further lowers the CN_{MgOW}.

The cation-anion pair formation is evident from the Mg^{2+}-S(of SO_4^{2-}) RDF presented in Figure 2.2a. For concentrations below the hydration limit, $g_{MgS}(r)$ is zero upto separations of 0.395 nm, implying that oppositely charged ions are not in the vicinity of each other. The highest $g_{MgS}(r)$ peak is observed at approximately 0.265 nm and is followed by another peak at 0.330 nm, which shows the existence of two ion-pair shells. A weaker $g_{MgS}(r)$ peak observed at around 0.235 nm, which gets smaller as the concentration increases, arises due to the charge distribution and structural configuration of the pentatomic SO_4^{2-} ion. One such orientation of the ion-pair is presented in Figure 2.2b for a 32.66 weight% solution with matching colors used to indicate the corresponding peaks in Figure 2.2b. The locations of the sulfate ions around a Mg^{2+} ion are also shown in Figures 2.2c and d. The CN_{MgS} curve has a plateau when the $g_{MgS}(r)$ profile lies in a valley as it transitions through a minimum.

At salt concentrations above the bulk solubility limit of ≈ 21 weight%, salt precipitation, which we identify as ion-pairs with lower hydration ($CN_{MgOW} < 4.5$), is observed. This can also be seen from the reduced ion-water CNs, that we show later. Increase in ion-pairs with increasing salt concentration also results in raising the CN_{MgO} between Mg^{2+}- O(of SO_4^{2-}) as shown in Figure 2.2c. The locations of the corresponding oxygen sites are presented in Figure 2.1d.

The larger size of the SO_4^{2-} ion, which has a molecular diameter ≈ 0.447 nm, contributes to its low charge density. The distribution of charges among the various sites of the pentatomic ion leads to its unique behavior. We present $g_{SOW}(r)$ and CN_{SOW} in Figure 2.3a which shows that there are two discrete hydration shells for the S in the SO_4^{2-} ion. This is

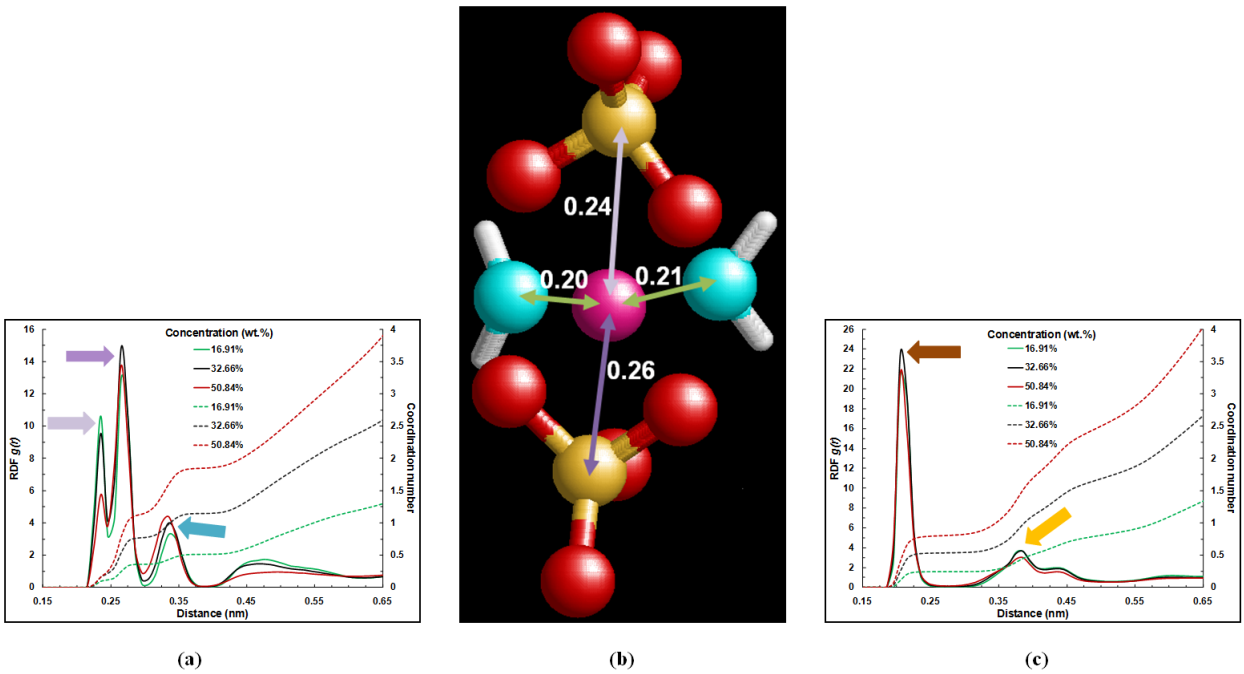

Figure 2.2: The radial distribution function, drawn with continuous lines, and coordination number, drawn with dashed lines, for Mg^{2+} and SO_4^{2-} with (a) S and (c) O sites of the cation at different salt concentrations. (b) The locations of various species around Mg^{2+} at 32.66% salt concentration by weight are represented in nm with the following color scheme: the green arrow labels the distance between a Mg^{2+} ion and a coordinating water molecule; purple (light and dark) arrows label the distances between Mg^{2+} and S(of SO_4^{2-}) and, respectively, correspond to the two peaks at 0.235 nm and 0.265 nm in the RDF in Figure 2.2a.

apparent through the peaks in $g_{SOW}(r)$ that occur around 0.355 nm and 0.405 nm. The low concentration $g_{SOW}(r)$ behavior agrees with that reported in the literature (Cannon et al., 1994; Vchirawongkwin et al., 2007). The tetrahedral anion structure attracts about nine coordinating water molecules in its first hydration shell, while almost five water molecules are associated with the peak at 0.405 nm. A selection of these water molecules around a SO_4^{2-} ion are shown in Figure 2.3b. While the number of coordinating water molecules decreases with increasing concentration, there is no well-defined plateau in the CN_{SOW} profile. This absence of the plateau can be attributed to the dissimilar charge distribution in the SO_4^{2-}

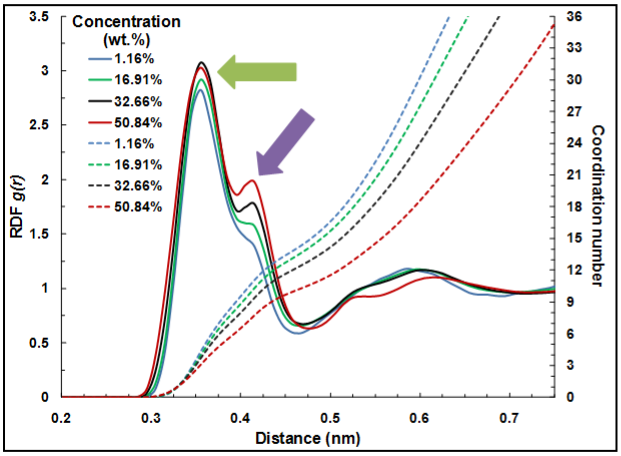

(a)

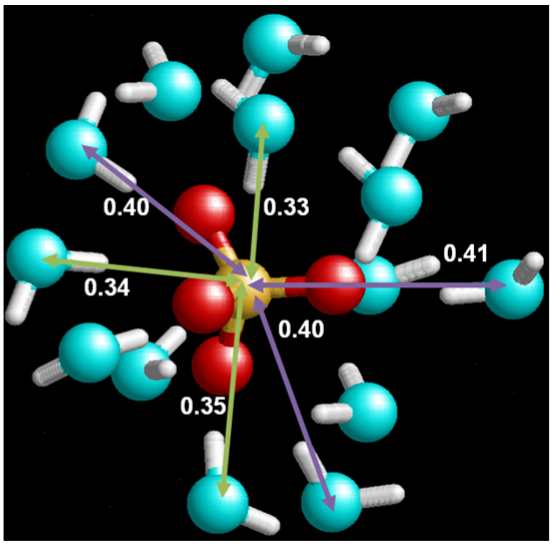

(b)

Figure 2.3: (a) The radial distribution function (RDF), drawn with continuous lines, and coordination number, drawn with dashed lines, for S(of SO_4^{2-}) and water at different salt concentrations. (b) The locations of water molecules around S at 1.16% salt concentration by weight are represented in nm with the following color scheme: the green and purple arrows label the distances between S(of SO_4^{2-}) and a coordinating water molecule and, respectively, correspond to the two peaks in the RDF in Figure 2.3a for the two hydration shells.

ion from that of the monatomic Mg^{2+} ion. Water molecules hydrating the S interfere with those that hydrate the O sites so that a distinct shoulder-like region in the CN_{SOW} curve is now absent. The decrease in the CN_{SOW} of the SO_4^{2-} ion with increasing concentration occurs due to formation of ion-pairs in a similar manner to the results described for Mg^{2+} in Figures 2.1c, d, 2.2a and b.

The RDF ($g_{OOW}(r)$) of the oxygen in SO_4^{2-} and the water molecules in the vicinity of this ion are next examined in order to understand the effect of the distributed charges in SO_4^{2-}. Again, the low concentration distribution of $g_{OOW}(r)$ agrees with previous studies (Cannon et al., 1994; Vchirawongkwin et al., 2007). Figure 2.4a shows three separate peaks (or maxima) for the O(of SO_4^{2-}) - water RDF at 0.285, 0.395 and 0.485 nm. The second

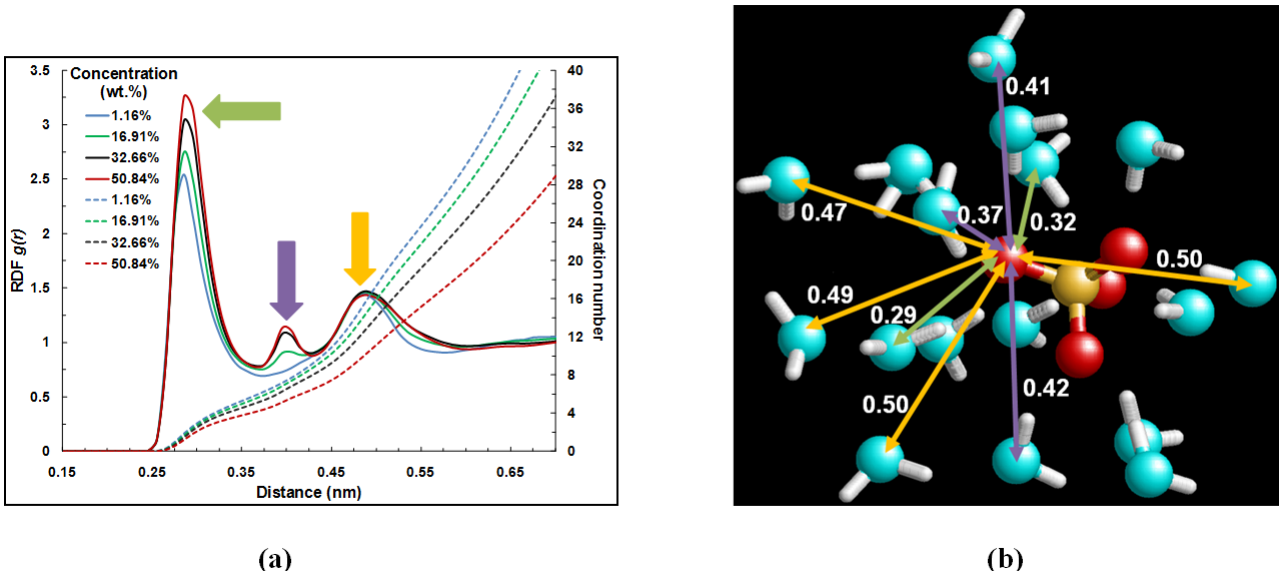

(a) **(b)**

Figure 2.4: (a) The radial distribution function (RDF), drawn with continuous lines, and coordination number, drawn with dashed lines, for O(of SO_4^{2-}) and water at different salt concentrations. (b) The locations of water molecules around O at 16.91% salt concentration by weight are represented in nm with the following color scheme: the green, purple and yellow arrows label the distances between an O(of SO_4^{2-}) and a coordinating water molecule and, respectively, correspond to the three peaks in the RDF in 2.4a.

of these peaks is conspicuous only at solutions above 32 weight%. The hydrating water molecules around an O site of a SO_4^{2-} are shown in Figure 2.4b for a representative simulation of a solution with a salt concentration of 16.91 weight%. Each SO_4^{2-} ion has four O sites surrounding the S. Hence, the probability that a water molecule lies in the vicinity of an O(of SO_4^{2-}) is higher than for the water to be in proximity of the S. This is also observed from the coordination numbers around the first peaks (cf. Figures 2.3a and 2.4a). Since the O sites now surround the S, there is less room for water molecules to hydrate the latter.

As the salt concentration increases, Mg^{2+} ions form ion-pairs with SO_4^{2-}. The structure of SO_4^{2-} is such that a single cation can interact across one plane of the 3-D tetrahedron (SO_4^{2-}) forming an ion-pair, while water molecules still continue to populate the other locations. Since both Mg^{2+} and S are positively charged sites, an ion-pair can stimulate stronger

attraction from the water molecules across the other planes of the tetrahedron at higher salt concentrations. This explains the increase in magnitude of the first $g_{OOW}(r)$ peak for O(of SO_4^{2-}) and water with increasing salt concentration in Figure 2.4a. For a 32.66% salt solution, the Mg^{2+} ion is typically hydrated by four water molecules as shown in Figure 2.1c. These water molecules promote the formation of a second hydration shell (which is the second peak in the $g_{OOW}(r)$) around O that is not noticeable for concentrations below the solubility limit.

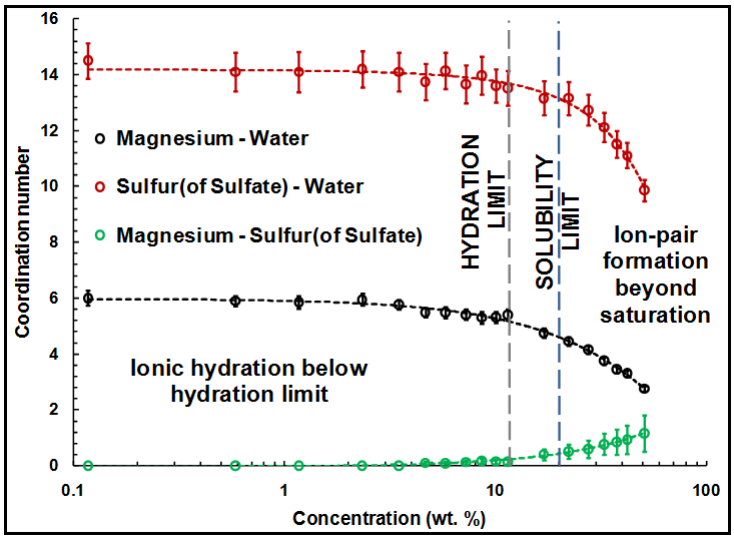

Figure 2.5: The variation in the coordination characteristics of different pairs of species with changes in salt concentration. The open circles correspond to the values for coordination number (CN) obtained from the simulations while dashed lines highlight the changes in CN with salt concentration (plotted on a logarithmic scale). The error bars represent the local standard deviations. These are calculated from the CN values recorded after every 1 ps during the last 0.5×10^6 timesteps of the simulation.

Figure 2.5 presents the variation in the CN for different pairs of species with changing concentration. As expected, the CN is constant until the hydration limit of the aqueous $MgSO_4$ solution at room temperature is reached at $\approx 11\%$. Beyond this salt concentration, as the solution gradually proceeds towards saturation, there is an abrupt decrease above the solubility limit in the CNs for hydrated ions, while the CN_{MgS} for Mg^{2+}- S(of SO_4^{2-}) increases due to the formation of ion-pairs. The hydration shells that previously encapsu-

lated individual ions gradually disappear with increasing salt concentration. This is due to diminishing numbers of water molecules in the concentrated solution so that more ion-pairs are simultaneously formed. At concentrations between ≈ 11 - 21 weight% (i.e., between the hydration and bulk solubility limits), although individual ions with hydration shells are not often observed, ion-pairs continue to be hydrated by the surrounding water molecules.

2.4 Summary

We find that while monatomic Mg^{2+} has hydration characteristics that are typical of a charged ion in an aqueous solution, the larger and heavier SO_4^{2-} anion behaves significantly differently. This is due to its lower and more complex charge density that arises from the charge distribution among its five sites. With increasing salt concentration, the number of coordinating water molecules for Mg^{2+} decreases from 6 to 3 due to the formation of Mg^{2+}-SO_4^{2-} ion-pairs. The cation-anion RDF shows that there are two ion-pair shells above the hydration limit. The coordination of water to SO_4^{2-} is influenced by the presence of charges on both the S and O sites, the impact of which is more prominent at higher salt concentrations. The coordination behavior of the ions changes after the hydration limit, which occurs at a concentration lower than the bulk salt solubility limit of the anhydrous $MgSO_4$.

Chapter 3

Enhanced mobility of water: Diffusion rates in aqueous salt solutions

We investigate the diffusion of ions and water in an aqueous magnesium sulfate solution using classical molecular dynamics (MD) simulations. The hydration of ions increases their effective size and mass. Thus, hydrated ion structures move significantly slower than the nonhydrating water molecules. Increasing ion concentrations should therefore reduce the average self-diffusion coefficient for water. Our simulations, however, show an increase in this self-diffusion coefficient for salt concentrations ranging from ≈ 0 - 2.3 weight%. While this behavior is not reported in the simulation literature, a few experiments have previously observed it. Some studies have attributed it to quantum effects related to the changes in energy levels created by the nuclear spins of the atoms constituting a water molecule, while others offer classical explanations that relate the distortion of stable structure of water to its enhanced diffusion rate. Our results, unlike the earlier empirical findings, point to a simpler explanation through a rigorous quantitative theoretical analysis. If the water in the solution is separated into two groups, one associated with ion hydration (Zone 1) and the remainder that is 'free' water in Zone 2, the self-diffusion coefficient of water in Zone 2 increases with ion

G. Balasubramanian, S. Murad, R. Kappiyoor and I. K. Puri, under review

concentration (as a result of fewer hydrogen bonds) while that for Zone 1 is either constant or decreases. The fractions of water molecules in Zones 1 and 2 vary with ion concentration, leading to the unusual initial concentration dependence of the overall diffusion rate of water. The self-diffusion coefficient of 'free' water follows an Arrhenius equation in which the activation energy for diffusion depends on the hydrogen bond energy of water, further pointing to the dependence of diffusion on water hydrogen bonds.

3.1 Mobility of water in ionic solutions

Apart from fundamental interest, the diffusion of water and ions in aqueous electrolyte solutions plays an important role in several industrial processes, e.g., ion separation and exchange, water treatment, energy storage, surface treatment (Auerbach, 2000; Balasubramanian et al., 2010b; Malani et al., 2006; Wang et al., 2007b) etc. In dilute aqueous solutions, ions are hydrated by the water molecules that surround them (Malani et al., 2006; Mountain, 2007). A hydrated ion remains structurally stable because of its large enthalpy of desolvation (Chandrasekhar and Jorgensen, 1982). Its motion is expected to be sluggish compared to that of nonhydrating free water since its effective size and mass are larger due to the hydrating water molecules that move along with it (Wang, 1954). As ion concentration in the solution increases, the fraction of water molecules associated with the ions also increase while the relative amount of free water decreases. Thus, the average diffusion of water is expected to be lower with increasing solute concentration (Chandra, 2000; Emel'yanov, 1965; McCall and Douglass, 1965). Here, using molecular dynamics simulations we investigate the effects of concentration on the diffusion of ions and water in an aqueous $MgSO_4$ (magnesium sulfate) solution. Our choice of the solute is motivated by its thermochemical energy storage capability (Balasubramanian et al., 2010b), which depends upon its solvation characteristics.

3.2 Simulation details

We employ equilibrium MD simulations (Allen and Tildesley, 1987) using the parallel GROMACS code (Hess et al., 2008; van der Spoel et al., 2005) on a 7 nm $\times$ 7 nm $\times$ 7 nm cuboid (x-y-z) system. This system contains an equal number of randomly distributed Mg^{2+} and SO_4^{2-} ions, and water molecules fill the remainder of the volume. The density of the system is adjusted to reflect the composition of the specific solution being simulated (Balasubramanian et al., 2011). The system is initialized at 300 K with a Maxwell distribution of the molecular velocities. We perform a series of canonical (NVT) simulations over 10^6 timesteps using the leap-frog integrator and a timestep of 0.002 picoseconds (ps). The system temperature is maintained constant during each simulation by rescaling the molecular velocities after every 0.1 ps.

The simple point charge (SPC) potential is used to model water molecules (Berendsen et al., 1981), since it can realistically represent experimental geometries, energies of ion-water complexes and energies of solvation (Guardia and Padro, 1990; Jorgensen et al., 1983). The parameters used for the nonbonded pairwise Lennard-Jones and Coulomb charge interactions of the Mg^{2+} and SO_4^{2-} sites have correctly reproduced their free enthalpies of solvation in cyclohexane and water (Oostenbrink et al., 2004). Table 2.2 lists these parameters as well as the bond and angle interaction potentials for all species (Berendsen et al., 1981; Guardia and Padro, 1990; Oostenbrink et al., 2004). Lorentz-Berthelot mixing rules (Allen and Tildesley, 1987) are used to reproduce cross-interactions. All simulations use a constant and relatively longer cut-off distance of 1.5 nm to account for long range effects. The self-diffusion coefficients of the different species in the system are calculated through the Einstein relation (Allen and Tildesley, 1987) using the mean square displacements computed every 1 ps during the last 2.5×10^5 timesteps of each simulation. Employing a thermostat in NVT simulations has been found not to significantly influence the diffusion coefficients in such ionic solutions (Shao et al., 2008). The self-diffusion coefficient of 4.22×10^{-9} m^2s^{-1} for pure water at 300 K obtained from our simulations concurs with the simulation literature (Mark and Nilsson, 2001). While the self-diffusion coefficient of SPC water does not agree quantitatively with experimental measurements, the potential model nevertheless reproduces the dependence of the self-diffusion coefficient on thermodynamic state variables, such as temperature and pressure, quite well (Jorgensen et al., 1983; Mark and Nilsson, 2001). In discussing our results, we define the hydration limit as the concentration at which ion-pairs begin to form and the solubility limit as the concentration above which only ion-pairs exist.

3.3 Comparison with earlier experiments and a quantitative theoretical analysis

Figure 3.1 presents the self-diffusion coefficients obtained for water, Mg^{2+} and SO_4^{2-} ions as a function of concentration up to 50.84 weight%. The results show that for low concentrations the self-diffusion coefficient of the ions is relatively high ($>\approx 0.25 \times 10^{-9}$ m^2s^{-1}) until a concentration of about 3 weight%. This coefficient decreases because of the increase in

their effective size due to the shared water molecules between adjacent hydrated ions. At concentrations above the hydration limit, ion pairs form, which further increases the effective size and mass of the ion clusters and decreases the self-diffusion coefficient of the ions. It reaches a limiting value of $\approx 0.01\times10^{-9}$ m^2s^{-1} beyond the $MgSO_4$ solubility limit of ≈ 21 weight%. The diffusion coefficient of water is significantly higher than that of the ions since it involves the diffusion of smaller and weaker hydrogen bonded water clusters as compared to hydrated ions.

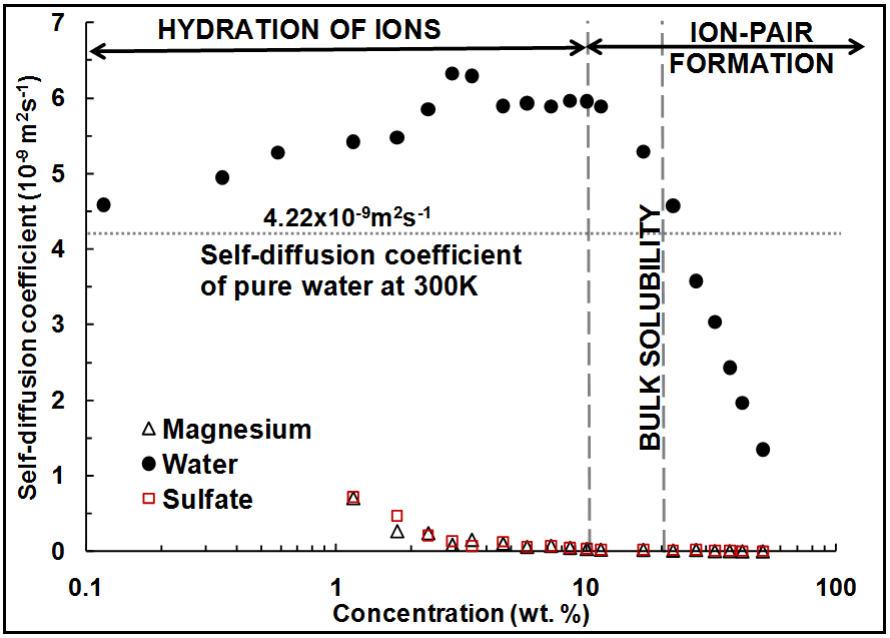

Figure 3.1: The variation in the self-diffusion coefficients of the different species (filled circles for water, open triangles for Mg^{2+}, and open red squares for SO_4^{2-}) in the solution with changes in salt concentration (plotted on a logarithmic scale). The dotted straight horizontal line denotes the value for the self-diffusion coefficient of pure water ($= 4.22\times10^{-9}$ m^2s^{-1} at 300 K). The dashed straight vertical lines respectively correspond to the initiation of ion-pair formation at ≈ 11.43 weight% and to the bulk solubility limit for $MgSO_4$ in water at ≈ 21 weight%. The maximum relative standard error for the self-diffusion coefficient of water is ±1%, while that for the ions is ±15%.

The simulations show an increase in the diffusion coefficient of water for concentrations up to ≈ 2.3 weight%. Thereafter, water diffuses at a constant rate up to a salt concentration of ≈ 11.43 weight%, which is approximately the hydration limit for the ions in the solution (Balasubramanian et al., 2011). As the ion concentration increases further, the fraction of water molecules associated with these ions also increases, which reduces the average self-diffusion coefficient of water further for concentrations above ≈ 11.43 weight%. Beyond the bulk solubility limit, almost all water molecules are associated with the ions which leads to a further substantial decrease in the mobility of water.

A literature review showed that no previous simulations have reported this concentration dependence, but some experiments (Emel'yanov, 1965; Krotenko et al., 1992; Lokotosh et al., 2010; McCall and Douglass, 1965; Sazonov et al., 1973; Wang, 1954) have reported this behavior (although others have not (Emel'yanov et al., 1969; McCall and Douglass, 1965; Sazonov et al., 1973)). Some experimental investigations explain this behavior on the basis of quantum effects. These suggest that different energy levels are created by the nuclear spins of the atoms constituting a water molecule in a magnetic field applied by an ion in the vicinity of water. A secondary magnetic field that is induced by motion of an electron cloud around a water molecule opposes this applied field. This alters the nuclear spin energy levels due to changes in the electron distribution so that the nuclei are effectively shielded by the diminished magnetic field that now acts on them. According to this explanation (McCall and Douglass, 1965), when the shielding increases with ionic concentration so does the self-diffusion of water. As the number of cations in the solution increases, the magnetic field energy associated with the vibrational and rotational motions of the solvent nuclei also increases. Longer nuclear magnetic spin-lattice relaxation times are required by the water molecules in the neighborhood of the ions to dissipate the additional energies gained from the enhanced vibrational and rotational motions and restore equilibrium. This is thought to augment the self-diffusion coefficient of water (Sazonov et al., 1973).

The relative standard errors for data in Figure 3.1 are estimated from the mean and the standard deviation calculated from the data recorded every 1 ps during the last 2.5×10^5 timesteps of each simulation. The self-diffusion coefficients of Mg^{2+} and SO_4^{2-} at low concentrations are not presented since the values calculated from the corresponding simulations have significantly large errors due to averages that must be taken over a relatively small number of ions.

Other studies have explained this unexpected concentration dependence of water diffusion at a classical (molecular/atomistic) level. They ascribe the increase in water diffusion obtained from experimental measurements of ionic solutions (Wang, 1954) and the simulations of water at different densities (Sciortino et al., 1992), to distortions in the structure of water. While they demarcate the water molecules in the ionic solution into different zones with respect to their configuration around the ions (Easteal et al., 1989; Wang, 1954), only empirical suggestions are provided to describe the enhanced mobility of water, since no direct or independent measurements of the water diffusion rates in those different zones were possible. Others hypothesize that the reduced local viscosity of water in the neighborhood of the structure-breaking ions augments its self-diffusion (Lokotosh et al., 2010). The size of the ions, as compared to the intermolecular distance between nearest neighbors in pure water, can influence the water mobility in electrolyte solutions (Lokotosh et al., 2010).

Through our investigation, we show, *for the first time in a molecular simulation study*, this unexpected concentration dependence of diffusion of water, and present a simple yet 'rigorous' quantitative analysis, neither easily possible experimentally nor reported in previous theoretical studies, to describe the phenomenon. We explain this behavior based on the hydration characteristics (Balasubramanian et al., 2011) of Mg^{2+} and SO_4^{2-}. All water molecules whose centers do not lie within a spherical region of 0.5 nm radius from the center of a Mg^{2+} or within a 0.9 nm radius sphere from the center of a SO_4^{2-} ion are classified as 'free' water (Zone 2), i.e., these water molecules do not hydrate any ions, while those that lie within this region, Zone 1, are classified as hydrating water molecules. The water molecules hydrating the ions in Zone 1 are expected to move slower at the diffusion rate of the associated ions than those that reside outside the hydration zones of these ions in Zone 2. We calculate the values for water diffusion rates in these zones directly via our simulations, which was not possible in earlier experiments, and provide a quantitative theoretical justification, unlike earlier investigations, to explain the phenomenon.

If N refers to the number of cations (or anions, since they are in equal number) in the solution, and C_{Mg} and C_{SO_4} denote the coordination number (Balasubramanian et al., 2011) of Mg^{2+} and SO_4^{2-}, respectively, at the specified concentration, then the average self-diffusion coefficient of all water molecules (H_O) can be expressed as

$$D_{H_2O} = \frac{NC_{Mg}}{N_{H_2O}} D_{Mg} + \frac{NC_{SO_4}}{N_{H_2O}} D_{SO_4} + \frac{N_{H_2O} - NC_{Mg} - NC_{SO_4}}{N_{H_2O}} D_{free} \tag{3.1}$$

where D_i represents the self-diffusion coefficient, $i = [Mg, SO_4, H_2O,$'free' water] and N_{H_2O} the total number of water molecules in the solution. Though a similar approach has been previously suggested (Easteal et al., 1989), the magnitude of the water diffusion rates in these zones and the influence of hydrogen bonds on them, as we discuss later, has not been previously reported. Equation 3.1 follows from the definition of the self-diffusion coefficient based on the mean squared displacement and the Einstein relationship (Allen and Tildesley, 1987), since our computational times are much longer than typical orientational times for water (Guardia and Padro, 1990). Since the average self-diffusion coefficient of water D_{H_2O} and that for the ions D_{Mg} and D_{SO_4} is obtained from the simulations, calculation of D_{free} using equation 3.1 is relatively straightforward. Values for D_{free} are reported in Table 3.1. The distribution of the diffusion rates for water in Zones 1 and 2 of the solution is presented in Figure 3.2. For concentrations below 2.33 weight% we fix $D_{Mg} = 0.242\times10^{-9}$ m^{2}s^{-1} and $D_{SO_4} = 0.210\times10^{-9}$ m^{2}s^{-1}, which are values obtained from a simulation with 2.33 weight% of salt. We do so because the self-diffusion coefficients averaged over the very small numbers of ions at low concentrations ($<$ 2.33 weight%) have large relative standard errors because only a few ions are available for the averaging. The results are based on sampling data recorded every 1 ps during the last 2.5×10^5 timesteps of each simulation.

Based on this analysis we find that D_{free} (or D_{Zone-1}) monotonically increases with salt concentration from a value of 4.60×10^{-9} m^{2}s^{-1} at 0.12 weight% to 9.27×10^{-9} m^{2}s^{-1} at 11.43 weight%. Thus the increase in D_{H_2O} between 0.12 - 2.33 weight% shown in Figures 3.1 and 3.2 as well as its subsequent constant value (which is higher than for pure water) up to 11.43 weight% both occur due to the enhanced mobility of 'free' water. Prior to ion-pair formation, a large number of 'free' water molecules exist in the solution. Hence, the contribution of D_{free} dominates the weighted average calculation of D_{H_2O} in equation 3.1. This explains the initial increase in the average self-diffusion coefficient of water obtained from our simulations, which is followed by the expected decrease in D_{H_2O} with increasing salt concentration.

The increase in D_{free} with increasing salt concentration should only occur if increasing the ion concentration also promotes the formation of smaller and weaker water clusters outside

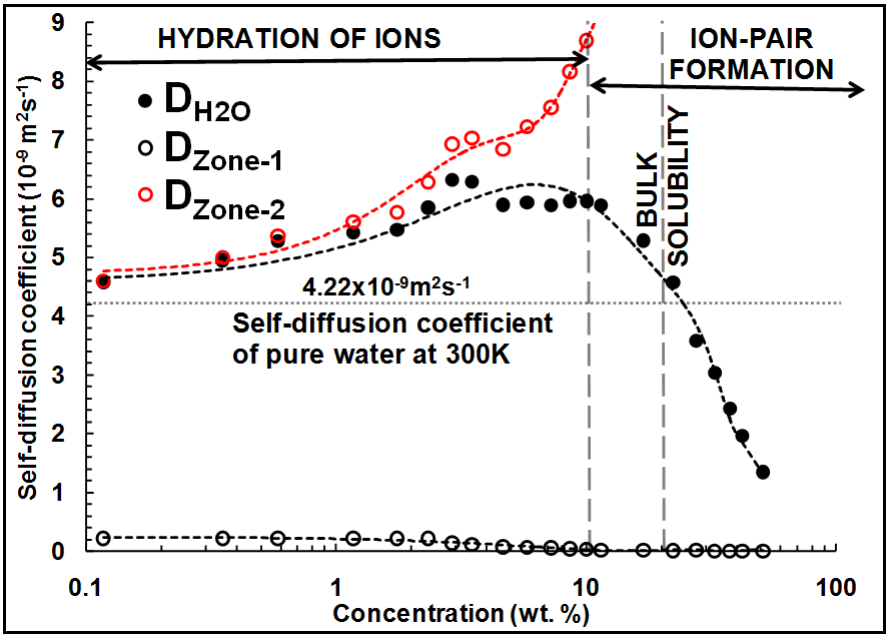

Figure 3.2: The variation in the self-diffusion coefficients of water in the entire solution D_{H_2O} (filled circles), within the hydration structures of the ions D_{Zone-1}(open circles), and 'free' water D_{Zone-2} (open red circles) with changes in salt concentration (plotted on a logarithmic scale). The diffusion rate of 'free' water is significant only at concentrations for which ion-pairs do not exist and so D_{Zone-2} is not presented for higher concentrations. The dotted straight horizontal line denotes the value for the self-diffusion coefficient of pure water (= 4.22×10^{-9} m^2s^{-1} at 300 K). The dashed straight vertical lines respectively correspond to the initiation of ion-pair formation at ≈ 11.43 weight% and to the bulk solubility limit for $MgSO_4$ in water at ≈ 21 weight% (Rodríguez Fernández-Alba, 2005). The dashed curves represent the variation in the respective self-diffusion coefficients with increasing concentration. The maximum relative standard error for D_{H_2O} is $\pm1\%$. Since D_{Zone-1} and D_{Zone-2} are derived from the self-diffusion coefficients of Mg^{2+}, SO_4^{2-} and water in the solution, we approximate the error percentage in their estimation as the maximum of those calculated for D_{Mg}, D_{SO_4} and D_{H_2O}, to be $\pm15\%$.

the hydration structures of the ions that enhances the mobility of the 'free' water molecules. A smaller water cluster implies one with fewer hydrogen bonds within the 'free' water molecules.

To verify this, we calculate the number of hydrogen bonds among the water molecules in the entire solution (System), in the hydration structures of the ions (Zone 1) as well as in the 'free' water (Zone 2).

Table 3.1: The coordination number of the ions, the self-diffusion coefficient of all the species in the system, and the number of hydrogen bonds per water molecule are listed for the simulations performed at different salt concentrations (by weight%). For concentrations below 2.33 weight% we fix $D_{Mg} = 0.242\times10^{-9}$ m^2s^{-1} and $D_{SO_4} = 0.210\times10^{-9}$ m^2s^{-1} (which are the values obtained from a simulation with 2.33 weight% of salt). This is done because the self-diffusion coefficients sampled over small number ions at low concentrations provide large relative standard errors.

Concentration (weight %)	Number of molecules/ions			Coordination number (CN)		Diffusion Coefficient ($10^{-9}m^2s^{-1}$)				Hydrogen bonds per water molecule		
	Water	Mg^{2+}	SO_4^{2-}	Mg^{2+}	SO_4^{2-}	Water	Mg^{2+}	SO_4^{2-}	Free water	System	Zone 1	Zone 2
0.12	11406	2	2	6	14.1	4.586	0.242	0.210	4.602	3.45	3.14	3.45
0.35	11385	6	6	6	14.1	4.950	0.242	0.210	5.001	3.43	3.34	3.44
0.59	11363	10	10	6	14.1	5.278	0.242	0.210	5.368	3.42	3.33	3.42
1.17	11315	20	20	6	14.1	5.421	0.242	0.210	5.611	3.39	3.27	3.39
1.75	11254	30	30	5.9	14.1	5.476	0.242	0.210	5.772	3.37	3.02	3.35
2.33	11200	40	40	5.9	14.2	5.848	0.242	0.210	6.285	3.34	3.03	3.33
2.91	11150	50	50	5.8	14.1	6.327	0.154	0.133	6.933	3.29	3.24	3.32
3.48	11114	60	60	5.8	14.1	6.294	0.103	0.126	7.036	3.27	3.25	3.29
4.64	10982	80	80	5.5	13.8	5.896	0.089	0.068	6.844	3.20	3.15	3.26
5.79	10877	100	100	5.5	14.1	5.933	0.074	0.070	7.224	3.15	3.11	3.22
7.22	10736	125	125	5.4	13.7	5.891	0.060	0.055	7.556	3.08	3.06	3.14
8.61	10653	150	150	5.3	13.9	5.961	0.048	0.042	8.165	3.03	3.01	3.12
10.04	10490	175	175	5.3	13.6	5.960	0.033	0.031	8.695	2.95	2.95	2.95
11.43	10358	200	200	5.3	13.5	5.892	0.022	0.023	9.270	2.90	2.89	2.93

Our definition of a hydrogen bond is based on its structural configuration: two water molecules are hydrogen bonded if (1) their inter-oxygen distance is smaller than 0.35 nm, which corresponds to the first minimum in the radial distribution function of water modeled

with SPC potentials (Chandra, 2000), and (2) the oxygen-oxygen-hydrogen angle is smaller than 30 (Hess et al., 2008; van der Spoel et al., 2005). The number of hydrogen bonds per water molecule, listed in Table 3.1, decreases in both Zones 1 and 2 with increasing salt concentration. This confirms our hypothesis that the reduction in the cluster size of 'free' water improves its self-diffusion coefficient. The number of hydrogen bonds per 'free' water molecule in Zone 2 decreases gradually from 3.45 at 0.12 weight% to 3.12 at 8.61 weight%, and then more rapidly to 2.95 at 10.04 weight% due to ion-pair initiation. Since no ion-pairs are formed in solutions at salt concentrations below 10.04 weight%, the dynamics of hydrogen bonding govern the mobility of 'free' water.

Diffusion is often expressed as an activation energy driven process using the Arrhenius equation

$$D(T) = D_0 exp(\frac{-\alpha E}{RT}) \tag{3.2}$$

where the activation energy for diffusion E is related to the energy of the solution (Holz et al., 2000; Philibert, 1991), and R denotes the universal gas constant. For our system, the self-diffusion of the 'free' water is expected to be most sensitive to the hydrogen bond energy of water. Figure 3.3 presents the variation of D_{free} with the normalized total activation energy $n_{Hb}E_{Hb}/(RT)$ for the self-diffusion of water, where n_{Hb} denotes the number of hydrogen bonds per water molecule in Zone 2, and the hydrogen bond formation energy for water E_{Hb} = 23.3 kJ mol^{-1} (Chaplin, 2010). The results show that the self-diffusion coefficient of 'free' water is well represented by equation 2 which confirms the dependence of the diffusion rate on the size and stability of the water clusters in the system. For the self-diffusion of 'free' water,

$$D_{free} \propto exp(\frac{-0.162 n_{Hb} E_{Hb}}{RT}) \tag{3.3}$$

The variation in the diffusion rates of water with changes in temperature for a solution concentration of 0.59 weight% are shown in Figure 3.4. The results, which are intuitive, show that with increasing temperature motion of water molecules also becomes faster. Temperature rise manifests in enhanced kinetic energy, thereby providing higher velocities for the

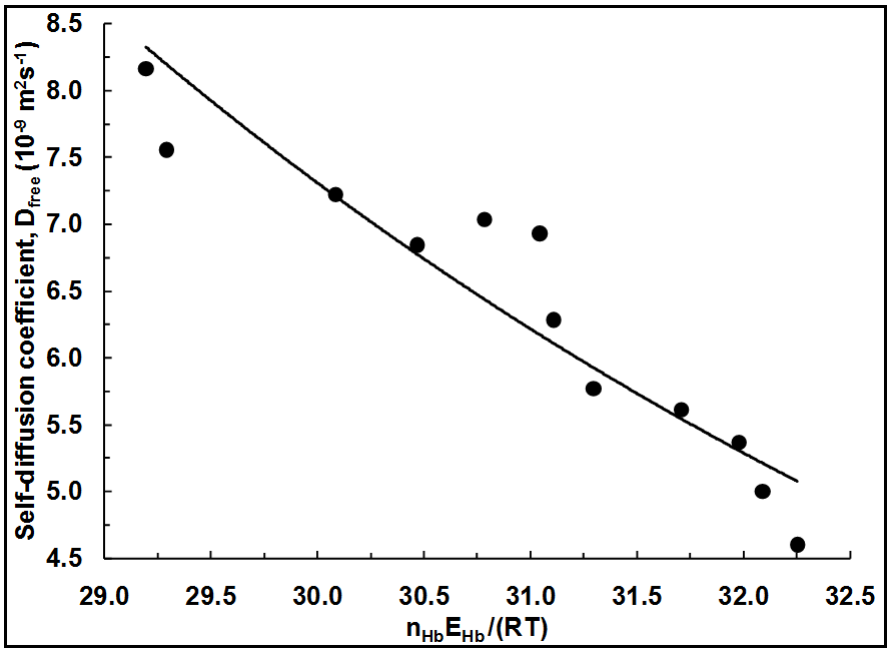

Figure 3.3: The variation in the self-diffusion coefficient of 'free' water in the solution with the normalized hydrogen bond formation energies of water. A fit (continuous curve) to the data shows that the diffusion of 'free' water is inversely proportional to the exponential of the hydrogen bond formation energies according to the Arrhenius' type relation $D_{free} = Aexp(\frac{-Bn_{Hb}E_{Hb}}{RT})$, where $A = 936.59\times10^{-9}$ m^2s^{-1}, $B = 0.162$ and $T = 300$ K. These energies decrease with increasing salt concentration as the number of hydrogen bonds per water molecule decreases. Since D_{free} is derived from the self-diffusion coefficients of Mg^{2+}, SO_4^{2-} and water in the solution, we approximate the error percentage in the estimation of D_{free} as the maximum of those calculated for D_{Mg}, D_{SO_4} and D_{H_2O}, to be $\pm15\%$.

movement of the solvent molecules. Thus, water molecules are able to diffuse in the solution rapidly and have a monotonically increasing self-diffusion with increasing temperature.

3.4 Summary

We find that the initial increase in the self-diffusion coefficient of water in an aqueous $MgSO_4$ solution at low salt concentrations occurs due to the enhanced mobility of water

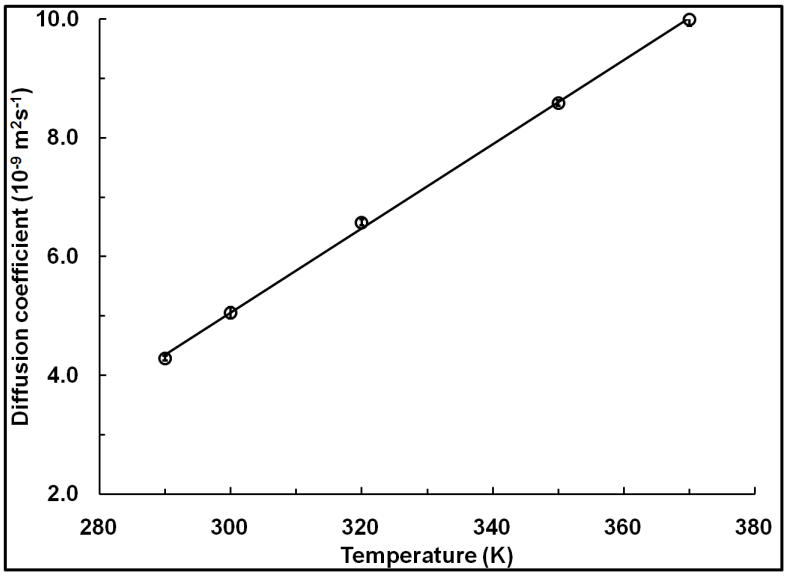

Figure 3.4: Variation in the diffusion coefficient of water with temperature for a dilute $MgSO_4$ solution. The relative standard errors (error bars) are estimated from the mean and the standard deviation calculated from the data recorded every 1 ps during the last 2.5×10^5 timesteps of each simulation.

molecules that reside outside the hydration zones of the ions. When the number of ions is increased in an aqueous solution, smaller clusters with fewer hydrogen bonds are formed in regions that contain non-ion-hydrating water. The increase in their self-diffusion coefficient D_{free} can be represented through an Arrhenius relationship where the diffusion barrier is related to the hydrogen bonding energy of water. In contrast, the slower movement of hydrated ions reduces the diffusion of the water molecules associated with them. Thus, the initial nonmonotonic response of D_{H_2O} to increasing salt concentration is simply the consequence of averaging of two self-diffusion coefficients in different zones of the solution, one that increases and another which decreases, and accounting for varying fractions of water molecules corresponding to the two contributions. When the salt concentration increases beyond its hydration limit, the fraction of water molecules that are associated with the ions also increases significantly. This decreases the self-diffusion rate of the ions as well as of water considerably beyond this limit.

Chapter 4

Collision of nanojets: A stagnation flow problem at the nanoscale

Molecular dynamics simulations are employed to describe the collision of two opposed liquid argon (Ar) nanojets and examine the subsequent stagnation flow. The streamwise and transverse velocity profiles in the proximity of the stagnation point are in agreement with macroscale continuum relations $u = \alpha x$, $v = -\alpha y$ for impinging laminar streams. Jet exit velocities are highest for non-wetting surfaces and decrease as solid-liquid interactions are enhanced. The work done to produce the nanojet dissipates at jet exits, increasing the local temperature. The fluid temperature is lowered through cooling as jets exit through the non-periodic boundaries. In comparison, water nanojets have higher exit velocities with relatively lower pressure drops across the reservoir and cavity.

G. Balasubramanian, I. K. Puri and S. A. Ragab, Chemical Physics Letters 491 (4-6), 177-182 (2010)

4.1 Dynamics of nanoscale jets

The molecular modeling of nanoscale jet formation and collision can involve length and time scales of $\bigcirc(10^{-10}$ m and 10^{-12} s) (Murad and Puri, 2007a,b), and high kinetic energy flow (Moseler and Landman, 2000; Murad and Puri, 2007a,b). The fluid dynamics at these small scales differs from continuum predictions if there are strong interfacial effects (which are enhanced by the large surface area to volume ratios) or binary intermolecular interactions. While the techniques adopted for ejection of nanoscale jets and their subsequent break-up have been described in literature (Dai and Chang, 2009; Fang et al., 2003, 2004; Shin and Yoon, 2008; Shin et al., 2008), and analytical (Eggers, 2002) and molecular investigations used to understand the physics behind the capillary instability and break-up of nanojets due to thermal fluctuations (Choi et al., 2006; Hanasaki et al., 2009; Shin et al., 2005), a discussion of the fundamental fluid mechanics involving the interactions between two impinging nanojets and the resulting stagnation flow problem is still absent. Molecular dynamics (MD) simulations (Allen and Tildesley, 1987) are employed to describe the collision of two opposed nanojets (Balasubramanian et al., 2010a) and examine the subsequent stagnation flow using continuum relations (Schlichting, 1968) that have been shown to be applicable at much larger scales (Puri and Seshadri, 1986).

4.2 Simulation details

The simulation configuration, described in Figure 4.1, consists of a 280 Å × 270 Å × 50 Å cuboid with two 85 Å × 250 Å × 50 Å reservoirs which include 20,953 pressurized liquid argon molecules with a density of 1350 kg m^{-3} at 100 K. Each reservoir is restrained between a 10 Å × 250 Å × 50 Å translatable solid wall and a 15 Å × 250 Å × 50 Å immovable solid membrane which can have varying exit slit widths W (= 25, 27.5 and 30 Å) along its mid-plane. Solid membranes, measuring 110 Å × 10 Å × 50 Å restrain the reservoir liquid in the transverse y-direction. The cavity between the reservoirs is 60 Å wide and is initially fully evacuated. The solid walls of each reservoir extend from -140 to -130 Å on one side of the center symmetry plane and from 130 to 140 Å on the other in the x-direction. The outer wall of each reservoir is squeezed towards the slit facing it with a constant velocity of

25 ms^{-1}. The pressure inside each reservoir builds up as its outer wall is pushed towards the corresponding slit in the inner membrane. This ejects two nanojets from the opposing slits into the cavity with velocities ranging between 100-130 ms^{-1} The nanojet exit Reynolds numbers for these flows (using a kinematic viscosity $\nu = 1.5\times10^{-7}$ m^2s^{-1} (Lemmon et al., retrieved February 1, 2009)) are in the range $Re \approx$ 1.8-2.2 so that the simulations involve laminar jets. Despite the relatively high nanojet exit velocities, based on a sound speed $c =$ 800 ms^{-1} the Mach number $Ma \approx$ 0.12-0.17 (Lemmon et al., retrieved February 1, 2009). The temperature of the liquid in the two reservoirs is held constant at 100 K during the entirety of the simulations by rescaling the molecular velocities (Balasubramanian et al., 2008) every timestep.

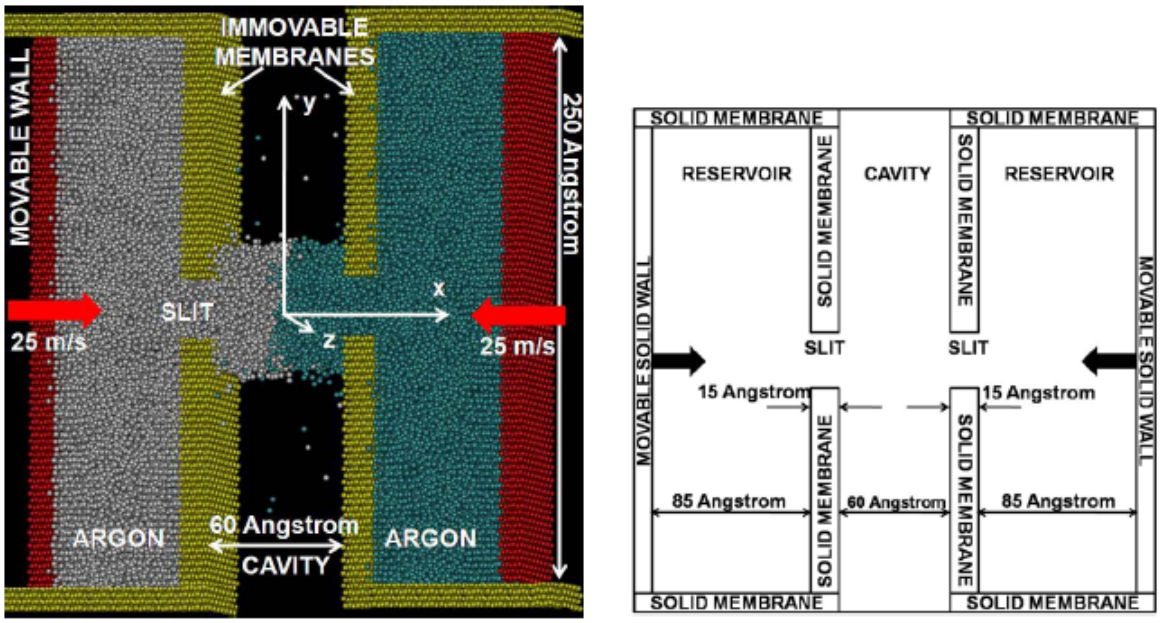

(a) (b)

Figure 4.1: (a) A 3D view of the MD simulation domain. Liquid argon molecules (represented by cyan and gray spheres) that are restrained between the movable walls (red) and immovable membranes (yellow) of two reservoirs emerge in the form of nanojets into an initially evacuated cavity. (b) Schematic 2D representation of the simulated system. The image lies in the $x-y$ plane while the $z-$direction is normal to the image plane.

The empirical pairwise Lennard-Jones (LJ) potential function

$$U_{ij} = 4\epsilon_{ij}\Big[(\frac{\sigma_{ij}}{r_{ij}})^{12} - (\frac{\sigma_{ij}}{r_{ij}})^{6}\Big] \tag{4.1}$$

is used to describe interactions between different pairs of (solid-liquid, liquid-liquid) molecules, where r_{ij} denotes the scalar distance between sites i and j, and σ_{ij} and ϵ_{ij} are the LJ interaction parameters. $\sigma_{ij} = 3.4$ Å and $\epsilon_{ij} = 0.0103$ eV for Ar ($i = j$). Since the focus is on the fluid physics in the vicinity of the stagnation plane, for simplicity the upstream solid walls are modeled with a face centered cubic (fcc) crystalline structure (lattice constant = 5.814 Å), the molecules of which interact as LJ sites that are tethered to their equilibrium positions. The energy parameter for the solid membrane-liquid interactions ${\epsilon^m}_{S-L} = \eta\epsilon_{S-L}$, where η is varied between 0.05-2 to understand the influence of surface wetting of the wall surfaces through liquid-solid intermolecular interactions on the jet exit velocities. A constant cut-off distance of 10 Å is maintained for all LJ interactions. The velocity-Verlet scheme is employed to perform the time integration of the molecular dynamics.

Periodic boundary conditions are applied in the streamwise $x-$ and spanwise $z-$directions. This permits a molecule exiting from one face of the simulation domain along the $x-$wise direction (or $z-$wise direction) to reenter from the other side. Nonperiodic fixed boundaries are assumed in the transverse $y-$direction to ensure that molecules that exit the cavity through one face cannot reenter it from the opposite boundary. The simulation domain is sufficiently large in the $y-$direction to allow the resulting stagnation flow to completely develop. The parallel LAMMPS code is used (Plimpton, 1995) to simulate the flows and employ a time step of 0.1 femtosecond. The liquid molecules are initially located at the vertices of an fcc lattice. This arrangement is allowed to equilibrate for an initial 2×10^5 simulation steps after which the molecules are found to behave freely as a liquid would. Thereupon, the solid reservoir walls are squeezed. The predominant contributor to the fluid velocity at the slit exit is through streamwise motion. The streamwise jet exit velocity U_e increases during the subsequent 10^6 steps of the simulation, but approaches a constant value thereafter as the system approaches quasiequilibrium. Each simulation typically runs for about 1.5×10^6 time steps.

4.3 Discussion of the findings

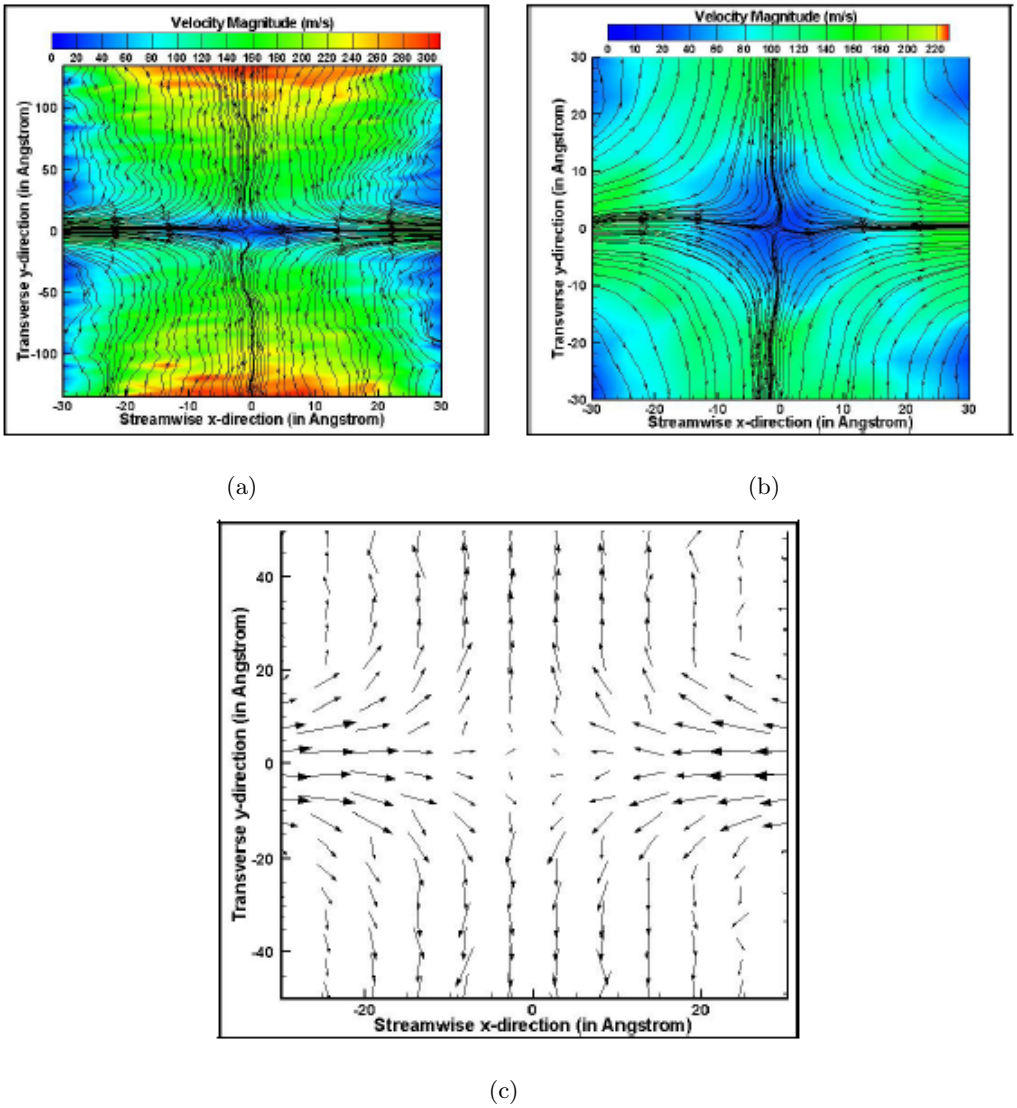

Figure 4.2: (a) Streamlines and contours of the velocity magnitudes for the stagnation flow formed due to impinging nanojets, both of which emerge through slit openings $W = 30$ Å; (b) Magnified view of (a) in the vicinity of the stagnation point (0, 0); (c) The flow velocity vectors. Periodic boundary conditions are applied along the $x-$wise and $z-$wise directions while nonperiodic fixed boundaries exist in the transverse $y-$direction. Magnified figures are provided in Appendix A.

The space enclosed between the two membranes is evenly divided into 648 cuboids, each of 5 Å × 5 Å × 50 Å volume, that penetrate the domain in the $z-$direction. The averaged velocity of all Ar molecules within each of these volumes is sampled at uniform time intervals. The streamlines for interactions modeled with $\eta = 1$ and $W = 30$ Å simulations are presented in Figure 4.2a. The contours in the figure represent the magnitudes $m = (u^2 + v^2)^{1/2}$, where u and v respectively denote the velocities (averaged over all atoms in a cuboid) along the $x-$ and $y-$directions. A stagnation plane develops at half the separation distance between the nanojet exits and deflects the opposing streams symmetrically, inducing transverse motion. The value of m is largest at the nanojet exit and its lowest values lie around the stagnation point (0,0) as shown in Figure 4.2b. The flow divergence seen in Figure 4.2c decreases u as it approaches the stagnation plane. At large transverse displacements, the contribution of v is dominant.

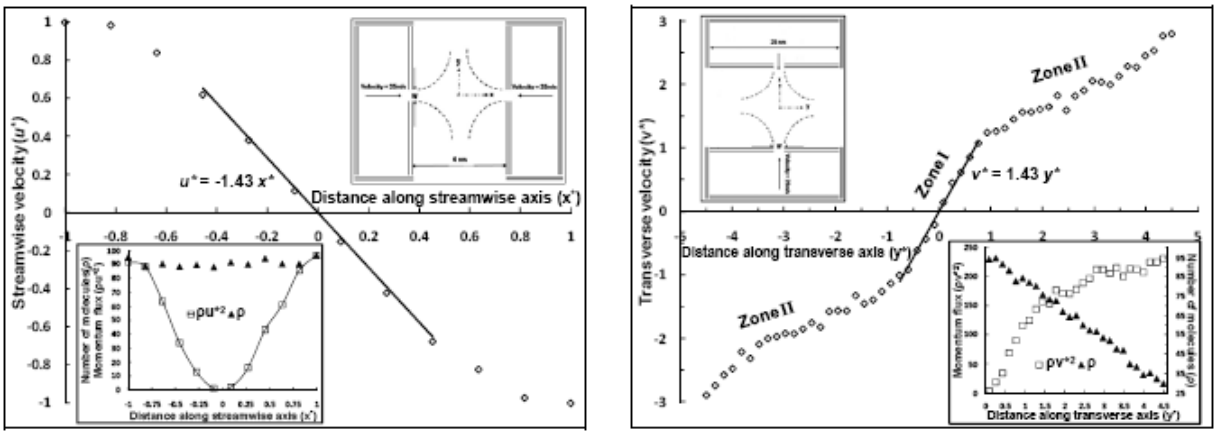

(a) (b)

Figure 4.3: Profiles of (a) streamwise velocity u^*, and (b) transverse velocity v^* for nanojets exiting through a $W = 30$ Å wide slit. The inset represents the distribution of the number of Ar molecules ρ and the momentum fluxes ρu^{*2} and ρv^{*2} along the midplane of the nanojets and the stagnation plane, respectively. The boundary conditions are identical to those described in Figure 4.2. Magnified figures are provided in Appendix A.

W and U_e are used to define the dimensionless coordinates $x^*= x/W$ and $y^*= y/W$, and velocities $u^*= u/U_e$ and $v^*= v/U_e$. Figures 4.3a and 4.3b present the u^* and v^* profiles

with respect to x^* and y^*. These profiles are symmetric with respect to the stagnation plane and the midplane bisecting the two nanojets, respectively. u^* decreases monotonically from the jet exit to the stagnation plane, in the vicinity of which it decreases according to the relation u^*= -1.43x^*. The inset shows the distributions of the numbers of molecules ρ and the momentum flux ρu^{*2} in slabs along x^*. Argon molecules are evenly distributed along the axis, i.e., $\rho \approx$ constant, so that the momentum distribution follows the u^{*2} profile. Figure 4.3b presents the evolution of the v^* profile. In Zone I in the vicinity of the system midplane, v^*= 1.43y^*. At larger $y-$distances from this midplane, ρ decreases towards the cavity exit. Thus, while the product ρv^{*2} initially increases linearly, its rate of increase declines for larger y^* in Zone II, which also implicitly decreases the rate of increase in v^*. The u^* and v^* profiles in the proximity of the stagnation point are in agreement with macroscale continuum relations u^*=αx^* and v^*=βy^* for impinging laminar streams with β = -α (Davey, 1961; Libby, 1967; Puri and Seshadri, 1986). The detailed derivation is given in Appendix A. The results for various parametric cases are listed in Table 4.1. The minor differences in the values of α and β are attributed to the averaging of sometimes relatively small ρ values. Very high velocity magnitudes occur near the $y-$boundaries as the fluid expands and the Ar molecules exit into vacuum.

Table 4.1: List of parameters and simulation results for various cases corresponding to different slit widths. α and β denote the dimensionless velocity gradients in the neighborhood of the stagnation point.

Case	Slit width W (Å)	Jet exit velocity U_e (ms^{-1})	α	β
I	30	100.59	-1.43	1.43
II	27.5	104.52	-1.36	1.37
III	25	129.69	-1.15	1.17

When the jets are of unequal velocities, the location of the stagnation plane shifts along the jet midplane. The results presented in Table 4.2 show that the location of the stagnation plane along the jet midplane is governed by the ratio of the jet exit velocities. Jets with

higher velocities and kinetic energies, shift the stagnation plane towards the lower velocity jet exit.

Table 4.2: Variation in the location of the stagnation plane with jet exit velocities. U_R and U_L are the jet exit velocities from $x^* = 1$ and $x^* = -1$ respectively, while L_R and L_L are the corresponding distances of the stagnation plane from the slits along the jet midplane.

U_L/U_R	0.4	0.8	1.0	1.2	1.6	2.0
L_L/L_R	0.28	0.56	1.0	1.78	3.55	13.28

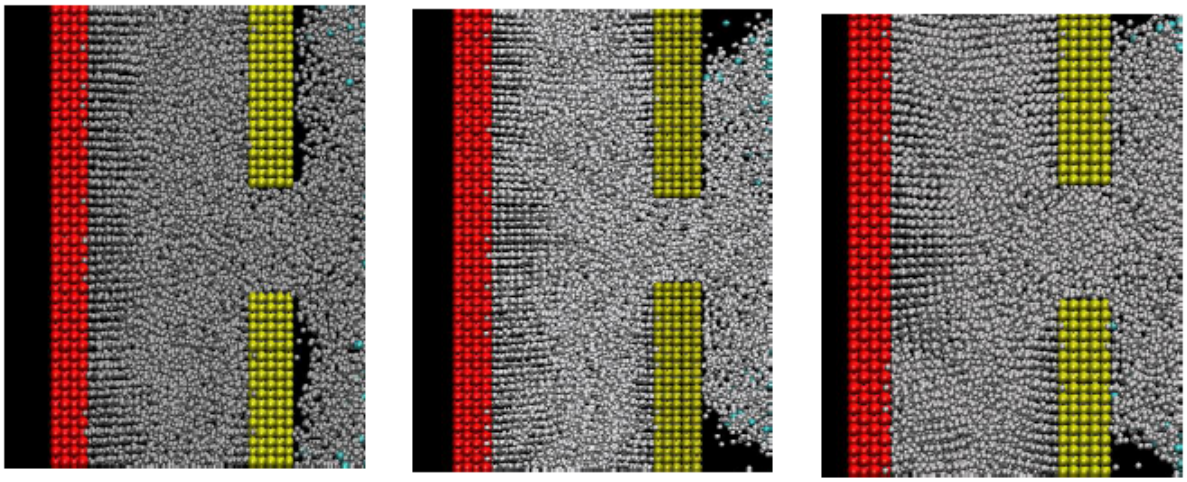

(a) (b) (c)

Figure 4.4: A 2D view of the MD simulation domain in the proximity of the slit exit. Liquid argon molecules (represented by cyan and gray spheres) are restrained between the movable walls (red) and immovable membranes (yellow) of the reservoir. The different cases shown present (a) non-wetting $\eta = 0.05$, (b) moderately wetting $\eta = 0.5$ and (c) strongly wetting $\eta = 2$ characteristics due to the liquid-solid interactions.

The effect of liquid wetting of the membrane surfaces on the jet exit velocities is investigated by varying η between 0.05-2. Larger values of η represent increasing attraction between the solid and liquid molecules causing wetting of the membrane surfaces. For smaller values,

e.g., when $\eta = 0.05$ (Figure 4.4a), the Ar molecules are phobic towards the membrane (although the high pressure inside (shown later) the reservoir counters this behavior by forcing liquid molecules closer to the membrane). For $\eta = 0.5$ (Figure 4.4b), the liquid is moderately wetting and forms layers on the surface. Figure 4.4c presents interactions for a strongly argonphilic surface with $\eta = 2$. In this case, dense layers of liquid molecules adhere to the solid membrane due to the enhanced intermolecular attraction between them. The solid-liquid interaction influences the jet exit velocities (Murad and Puri, 2007a). Figure 4.5 shows that U_e is larger for argon-phobic surfaces but much smaller when the solid-liquid interactions are enhanced. For smaller η, Ar molecules emerge from the slits with higher velocities due to their preferential binding. When η is larger, the affinity between the membrane and argon holds the liquid molecules back into quasi-crystalline layers (Balasubramanian et al., 2008), which reduces the jet exit velocity according to the relation $U_e \propto \eta^{-0.067}$.

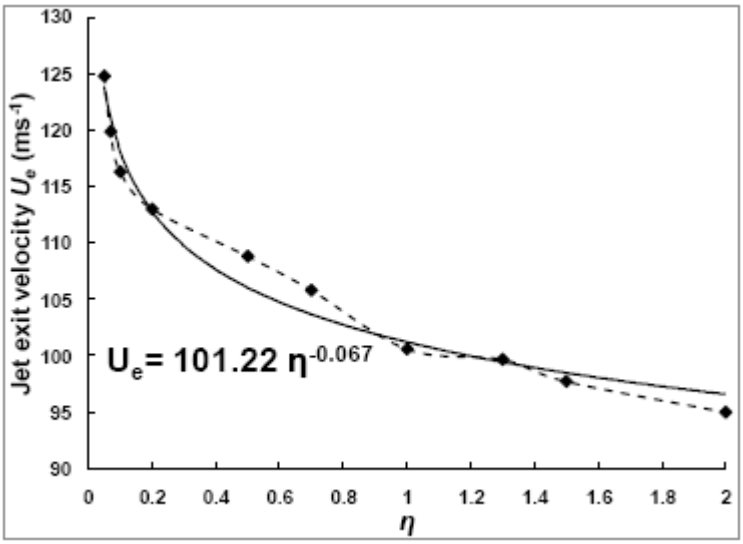

Figure 4.5: Changes in the jet exit velocity U_e due to varying values of η representing non-wetting (low values of η) and wetting (high values of η) regimes due to liquid-solid interactions.

Next, the system thermodynamics are monitored in terms of the average pressure and temperature in different slabs along both the streamwise and transverse directions for η = 1 and W = 30 Å. The entire volume is now divided evenly into 5 Å × 30 Å × 50 Å

$(x \times y \times z)$ slabs to calculate the pressure (from the stress on the atoms (Plimpton, 1995) in a slab) and temperature (from the molecular kinetic energy (Plimpton, 1995)). Figures 4.6(a) and 4.6(b) present the pressure and temperature distributions in the $x-$direction during different simulation times (after 80, 100, 120 and 140 picoseconds (ps)). Squeezing the outer walls of the two reservoirs inwards increases the pressure inside them so that Ar molecules are forced out through the slits. The local fluid pressure decreases as fluid emerges from each slit, increasing the jet exit velocities as shown in Table 4.1. The narrower the slit width, the greater the pressure drop and the larger is the velocity of the exiting liquid. The pressure inside the cavity remains constant along the jet midplane but increases over time since molecules accumulate there.

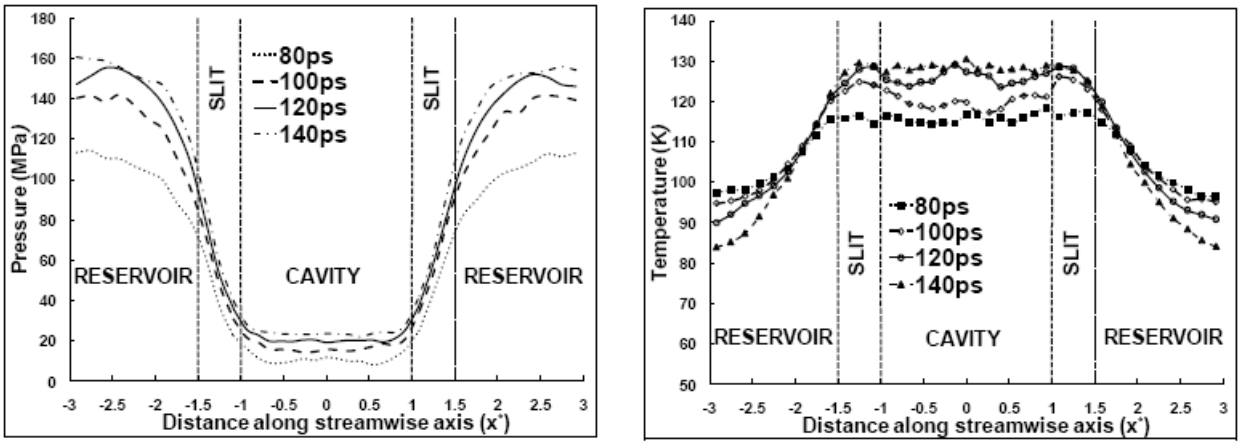

(a) (b)

Figure 4.6: (a) Pressure and (b) temperature distribution along the streamwise axis after 80, 100, 120 and 140 picoseconds of the simulation for nanojets exiting through a W = 30 wide slit with the boundary conditions identical to those for Figure 4.2.

The temperature distributions presented in Figure 4.6b are determined after first subtracting the mean flow velocity from the corresponding molecular velocities and then computing the average kinetic energy of the molecules in a slab. The average temperature of each reservoir is maintained constant through velocity rescaling. The reservoir temperature near the slit increases due to increased internal friction caused by enhanced intermolecular interactions. Some of the work done on the system to squeeze the outer walls of the reservoirs

inwards is dissipated at the jet exit, raising the local temperatures. Over time, this energy input increases the molecular kinetic energies and thus the overall temperature inside the cavity. Although the temperature increases over time, at any instant the temperature within the cavity is relatively uniform.

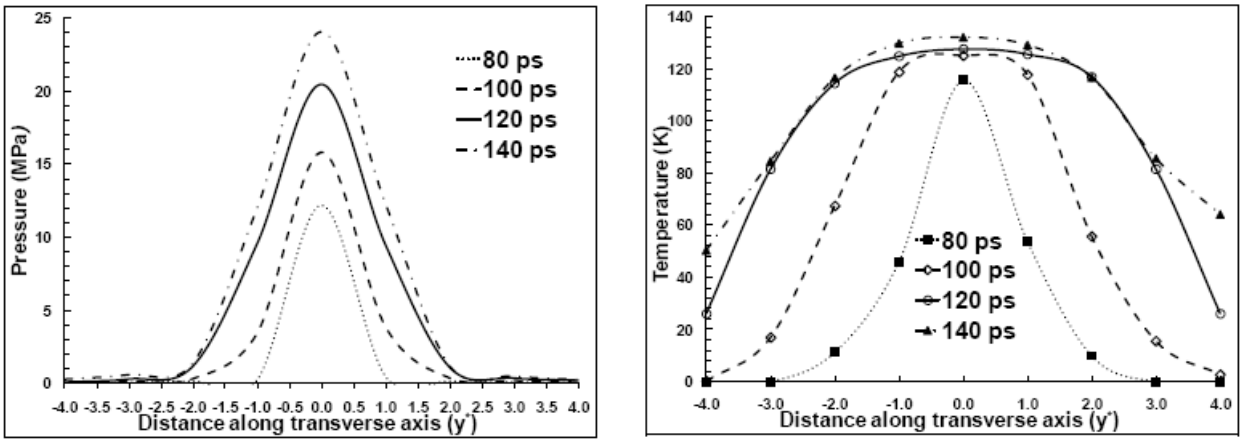

(a) (b)

Figure 4.7: (a) Pressure and (b) temperature distribution along the transverse axis ($x^* = 0$) after 80, 100, 120 and 140 picoseconds of the simulation for nanojets exiting through a W = 30 Å wide slit with the boundary conditions identical to those for Figure 4.2.

Figure 4.7a shows that the pressure along the y-direction increases over time as additional molecules interact inside the cavity. Thus, since the number of molecules in the stagnation region increases over time, so does the pressure. The intermolecular interactions, that are largest where the jets collide, also contribute to the high values around the stagnation zone. The fluid pressure at locations removed from the stagnation zone is considerably lower due to the far lower local densities (reflected in Figure 4.3b) and temperature (shown later in Figure 4.7b). The nonperiodic boundaries simulate a vacuum outside the cavity where the pressure is zero.

The temperature distribution along the $y-$axis, presented in Figure 4.7b, also reaches a maximum at the stagnation point and gradually decreases towards the cavity exit as the molecules expand into a low pressure region. The intermolecular distances increase due to the expansion, increasing the potential energy of fluid. Since there is no net energy exchange

along the stagnation plane and the overall energy of the fluid in the cavity is conserved, the increase in potential energy decreases the molecular kinetic energy. Thus, the jet temperature decreases in the $y-$direction moving away from the stagnation streamline.

The thermodynamics for two impinging Ar nanojets are compared with that of corresponding water jets by replacing argon with a saturated liquid-vapor mixture of water (with an initial 40% vapor volume fraction) at 300 K in the reservoir. Interactions between water molecules are modeled using the SPC potential parameters (Murad and Puri, 2007b), which include the Columbic interactions due to charges in addition to the Van der Waals forces modeled by the pairwise LJ potential function. The jets exit the reservoirs with velocities of about 270 ms^{-1}, which are much higher than those for liquid Ar.

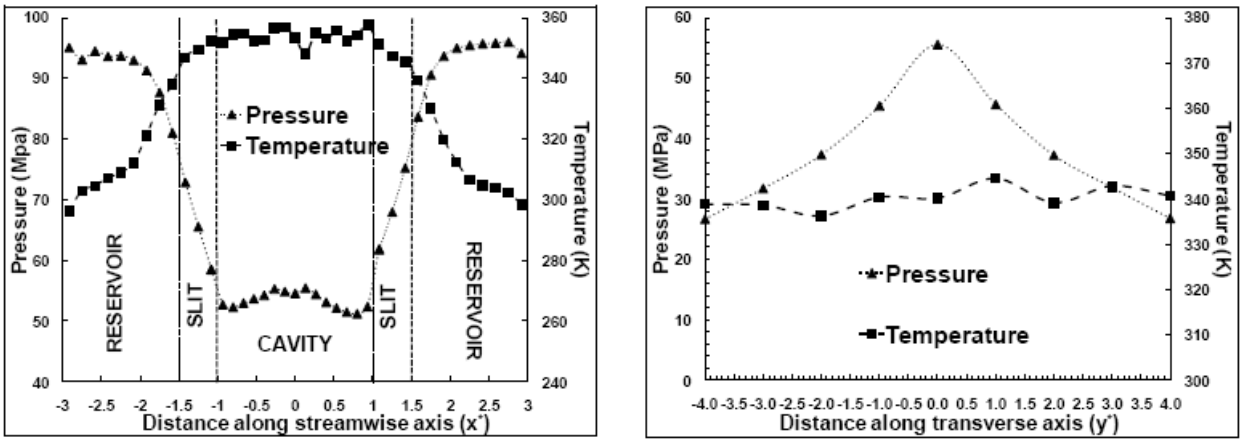

(a) (b)

Figure 4.8: Averaged pressure and temperature distribution along the (a) streamwise axis and the (b) transverse axis for the simulation of water nanojets exiting through a W = 30 Å wide slit with the boundary conditions identical to those for Figure 4.2.

The average temperature and pressure distributions along the x-axis for the colliding water nanojets are presented in Figure 4.8a. As seen earlier in Figure 4.6a, squeezing of the outer reservoir walls increases pressure, forcing water into the cavity through the slits. While the pressure drops as water exits the slits, it remains almost constant inside the cavity with a small increase near the stagnation zone. Unlike for liquid argon, where pressure drops as large as 130 MPa are computed, a much lower pressure difference of $\approx$ 45 MPa is observed

between the reservoir and the cavity when water is used. The higher kinetic energies of the fluid molecules (1) require a smaller pressure to squeeze them from the reservoir, and (2) lead to higher velocity collisions at the stagnation plane, which raise the local pressures inside the cavity. Again, the reservoir temperature near the slit increases due to enhanced intermolecular interactions that arise from the dissipation of the work to squeeze the fluid. This also raises the local temperature inside the cavity. The temperature difference between the reservoir and the cavity is ≈ 60 K, and larger than the 40 K rise for Ar nanojets. Figure 4.8b shows that the pressure along the $y-$direction is largest near the stagnation zone where the jets collide and gradually decreases as the jets exit the cavity through the boundaries. Since water molecules are released with higher jet exit velocities, they also require less time to reach the stagnation plane. Hence, the cavity fills with water molecules faster than it does with argon molecules. Thus, even at locations further removed from the stagnation zone, the fluid molecules have a finite pressure and the higher kinetic energies of the molecules raise the local temperatures, which remains relatively uniform inside the cavity along the transverse direction.

4.4 Summary

The streamwise (u^*) and transverse (v^*) velocity profiles in the proximity of the stagnation point formed by the collision of opposing nanojets agree with the macroscale continuum relations for impinging laminar streams. While this is always the case for the streamwise $x-$velocity, the transverse $y-$velocity profile exhibits a different behavior, which follows continuum predictions closer to the midplane of the nanojets but does not at larger displacements. In the latter region, high velocities are observed as molecules exit into vacuum. The wetting of the solid by liquid Ar influences the jet exit velocities according to the relation $U_e \propto \eta^{-0.067}$. The fluid pressure decreases as the molecules move from the pressurized reservoir into the cavity. Some of the work done on the system to squeeze the reservoirs is dissipated as an increase in the internal energy of the fluid at the jet exits, raising the overall temperature inside the cavity. The pressure is highest at the stagnation point and decreases in the transverse direction towards the cavity exit as molecules expand into the vacuum imposed by

the nonperiodic fixed boundaries. Subsequent cooling along the stagnation plane lowers the fluid temperatures along the y-direction. Nanoscale jets consisting of saturated liquid-vapor mixtures of water emerge from the slits with higher jet exit velocities and hence require less time to completely fill the cavity. The pressure drop across the reservoir and the cavity is lower than that for argon nanojets, while the temperature increase is larger. The temperature distribution in the transverse direction is relatively uniform, while the pressures are highest in the stagnation zone where the jets collide.

Chapter 5

Shear viscosity enhancement: Effects of introducing a nanoparticle suspension in a liquid

Equilibrium molecular dynamics simulations characterize the increase in shear viscosity of water that includes a suspended silicon dioxide nanoparticle. The layering of water on the solid surface increases the fraction of less mobile and more viscous fluid molecules adjacent to them, thereby increasing the shear viscosity. We identify the contribution of the relative nanoparticle surface area to this rheological behavior through an empirical model. This model successfully reproduces the high volume fraction shear viscosity predictions from the atomistic simulations and previous experimental measurements.

G. Balasubramanian, S. Sen and I. K. Puri, under review

5.1 Rheology of fluids with solid suspensions

The shear viscosity of a fluid increases in the presence of nanoparticle suspensions (Chow, 1993; Eastman et al., 2004; Hughes, 1954; Sandhu, 2007). Experimental (Chevalier et al., 2007, 2009; Das et al., 2003; Namburu et al., 2007; Venerus et al., 2010; Wang and Mujumdar, 2008) and theoretical (Keblinski et al., 2002; Masoumi et al., 2009; Wang et al., 2003; Wang and Mujumdar, 2008) investigations have reasoned that the layering of fluid molecules on the nanoparticle surfaces as well as aggregation of these solid suspensions into larger masses influence the fluid rheology. The fluid viscosity η_{fluid} increases above its base value $\eta_{base-fluid}$ with increasing nanoparticle volume fraction (or concentration)ϕ that compares the total volume of all the nanoparticles to the total volume of the fluid and the suspension. Even for small ϕ when agglomeration effects are negligible, η_{fluid} can be significantly different from the low ($< 2\%$) nanoparticle concentration prediction of the Einstein equation $\eta_{rel} = 1+2.5\phi$, where the relative viscosity $\eta_{rel} = \eta_{fluid}/\eta_{base-fluid}$ (Hughes, 1954; Prasher et al., 2006b; Tavman et al., 2008).

The volume fraction increases with larger numbers of suspended nanoparticles or when those with larger dimensions are introduced. While spheres are the common particle shapes employed in experiments, a naturally occurring crystal lattice is typically of cuboid origin, which is rarely accounted for in quantitative predictions of the fluid viscosity (Wang et al., 1999). Previous atomistic simulations to determine the fluid viscosity in nanochannels (Pozhar, 2000; Pozhar et al., 2002; Zhang et al., 2009) and of colloidal suspensions (Bastea, 2007; in't Veld et al., 2009) have used elementary parametric potentials to describe the molecular interactions, making quantitative comparisons with experiments difficult. Here, we use equilibrium molecular dynamics (MD) simulations to determine particle size and surface area effects on the shear viscosity of a physically realizable system that contains water surrounding a suspended silicon dioxide nanoparticle. Since we simulate a realistic nanoparticle with established potential models for the solid and the fluid intermolecular interactions, we accurately characterize the influence of the particle on the surrounding water, and calculate the actual shear viscosity that is compared with previous experimental measurements. A model for the effective viscosity increase is proposed whose predictions are in close agreement with

empirical relations obtained through experiments.

5.2 Simulation details

A crystalline silicon dioxide cuboid is placed at the center of a 9.0 nm × 9.0 nm × 9.0 nm (x-y-z) simulation cell with water molecules filling the remainder of the space. The particle dimensions are listed in Table 5.1. Changing the y- and z-dimensions of the particle varies the volume fraction ϕ. The system is initialized at 1 atm. and 300 K with a Gaussian distribution of the molecular velocities. Equilibrium isothermal-isobaric (NPT) simulations are performed followed by canonical (NVT) simulations. Each of these are conducted over 10^5 timesteps using the velocity-Verlet integrator and a timestep of 0.001 picoseconds (ps) in order to release the internal stresses and equilibrate the system to its actual density. Non-Hamiltonian Nose-Hoover equations of motion are employed with a coupling time of 0.1 ps to maintain the system temperature (300 K) and pressure (1 atm.) constant. Upon equilibration, microcanonical (NVE) simulations are performed for a further 0.5×10^6 timesteps when the fluid is allowed to behave freely. Concurrently, the off-diagonal components of the pressure tensor (P_{ij}, i≠j: x, y, z) are sampled at an interval of 5 timesteps to obtain their average autocorrelation ($< P_{ij}(t_o)P_{ij}(t+t_o) >_{to}$) every 0.2 ps. η_{fluid} is calculated through the time integration of the average autocorrelation using the Green-Kubo formula

$$\eta_{ij} = \frac{V}{k_B T} \int_0^\infty \{< P_{ij}(t_o)P_{ij}(t+t_o) >_t\} dt \tag{5.1}$$

and $\eta_{fluid} = < \eta_{ij} >$ (Gonzalez and Abascal, 2010; Pozhar, 2000).

The MD simulations are based on the parallel LAMMPS code (Plimpton, 1995). The 3-site TIP3P model (with harmonic bond and angle interactions), which is able to realistically represent experimental geometries, intermolecular energies and heat of vaporization of water, is used to simulate the base fluid (Jorgensen et al., 1983). The Tersoff potential is employed to model interactions of silicon dioxide (Munetoh et al., 2007) while Lennard-Jones parameters with Lorentz-Berthelot mixing rules are used to model cross-interactions (Murad and Puri, 2009a) between water and the nanoparticle. A particle-particle particle-mesh (PPPM) solver is implemented to account for long-range effects due to charges.

Table 5.1: Values for the shear viscosity η_{fluid} obtained for different sizes (volume fractions) of the nanoparticle. The particle lengths are increased in the y and z dimensions to increase the volume fraction (ϕ). Viscosity increases with increasing ϕ. Typically, the shear component of viscosity for a nanoparticle with a larger surface area is relatively larger than of the other components. η_{fluid} values reported are averages over values recorded every 0.2 ps between 350 - 450 ps of the MD simulations. The standard deviation for each case is smaller than $\pm 0.5\%$.

Particle dimensions	Aspect ratio		No. of molecules in the particle	Volume fraction	η_{xy}	η_{xz}	η_{yz}	η	$\frac{\eta}{\eta_{\text{TIP3P}}}$
H(nm)× B(nm)× L(nm)	B/H	L/H			(mPa.s)				
2.49× 1.99× 2.78	0.799	1.116	960	0.019	0.324	0.339	0.292	0.318	1.026
2.49× 2.49× 3.47	1.000	1.394	1500	0.030	0.306	0.341	0.358	0.335	1.081
2.49× 2.99× 4.17	1.201	1.675	2160	0.043	0.351	0.439	0.438	0.409	1.319
2.49× 2.99× 4.86	1.201	1.952	2520	0.050	0.379	0.466	0.481	0.442	1.426
2.49× 3.48× 4.86	1.398	1.952	2940	0.057	0.404	0.544	0.518	0.487	1.571
2.49× 3.48× 5.56	1.398	2.233	3360	0.066	0.405	0.556	0.587	0.516	1.665
2.49× 3.98× 5.56	1.598	2.233	3840	0.076	0.473	0.613	0.614	0.567	1.829
2.49× 3.98× 6.25	1.598	2.510	4320	0.085	0.511	0.725	0.724	0.653	2.106
2.49× 4.48× 6.25	1.799	2.510	4860	0.096	0.506	0.731	0.732	0.656	2.116
2.49× 4.98× 6.95	2.000	2.791	6000	0.118	0.597	0.793	0.882	0.757	2.442

5.3 Predictions from the simulations

From the simulations, the shear viscosity of (TIP3P) pure water $\eta_{TIP3P} = 0.31$ mPa.s which, although different from experimental measurements, closely agrees with previous MD simulations of liquid water (Gonzalez and Abascal, 2010), validating the simulation technique. Averaged values of η_{fluid} obtained between 350-450 ps of the simulation are presented in Table 5.1 for different ϕ. Figure 5.1 presents the time evolution of η_{fluid} determined from the time integral of the average autocorrelation for different values of ϕ. It initially increases

and then relaxes to a constant magnitude after ≈ 200 ps. The increase in η_{fluid} is attributed to equilibrium fluctuations, which dissipate over longer times, providing a converged autocorrelation value.

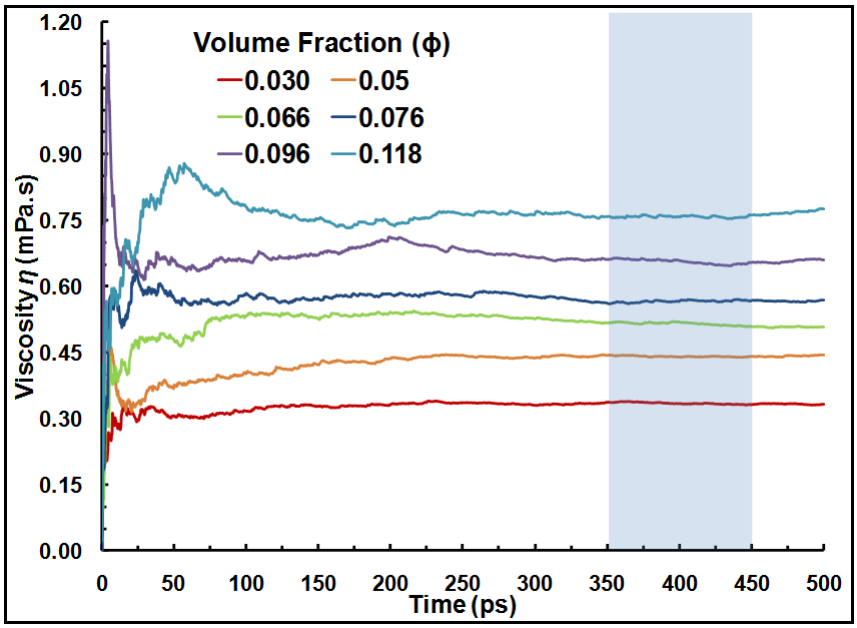

Figure 5.1: The shear viscosity η_{fluid} of water containing different sizes (or volume fractions) of the silicon dioxide nanoparticle for six representative simulations. η_{fluid} is calculated from the time integration of the autocorrelation of the off-diagonal components of the pressure tensor. The initial fluctuations dissipate as the system relaxes over time and the average autocorrelation converges. The values for η_{fluid} are calculated as averages over values recorded every 0.2 ps between 350 - 450 ps (shaded zone in the figure) of the simulations that have a standard deviation of smaller than ±0.5% for any of the cases.

Increasing the particle size increases ϕ and η_{fluid}. For $\phi = 0.019$, η_{fluid} increases by ≈ 2.6% over η_{TIP3P}. This increase is more significant (≈ 144%) when $\phi = 11.8\%$. These predictions are in good agreement with previous experimental measurements (Chevalier et al., 2007, 2009; Tavman et al., 2008) for silicon dioxide suspensions in water. However, minor differences exist because

1. Changes in the experimental volume fraction are implemented by incorporating different

numbers of similar nanoparticles and not by varying their size as in the simulations,

2. The nanoparticles in the experiments are approximated as spheres in contrast with the cuboid that is simulated,

3. The classical simulations use empirical functions to describe the behaviors of the solid and liquid phases,

4. Information about the material characteristics of the nanoparticles used in the experiments, such as whether they are amorphous or crystalline, is unavailable whereas the simulations assume a crystalline silicon dioxide structure,

5. Effects such as particle aggregation (Prasher et al., 2006a,b) that can further enhance the viscosity are absent from the simulations, and

6. Since the simulations are restricted by computational constraints, the characteristic dimensions of simulated nanoparticles are smaller than of those typically used in experiments.

The increase in η_{fluid} with ϕ is attributed to the adsorption of fluid molecules on the larger nanoparticle surfaces. Interfacial effects produce ordered quasi-crystalline layers of fluid molecules on these solid surfaces (Balasubramanian et al., 2008; Keblinski et al., 2002; Murad and Puri, 2008a) that have a reduced mobility due to their stronger attraction to silicon dioxide. Consequently, the layers impart additional resistance to fluid motion at the solid-fluid interfaces. Figure 5.2 presents the distribution of water around the y-z cross-section of a nanoparticle at $\phi = 9.6\%$. The x-wise width of this section is 0.3 nm, which is approximately 1 molecular diameter. The density of water molecules is highest in the neighborhood of the silicon dioxide surface and it gradually decreases at locations that are further away. The solid-like fluid atoms that are layered around the nanoparticle span a region equivalent to $\approx$ 2-3 molecular diameters.

The fraction of fluid molecules that is less mobile and hence more viscous than the surrounding "free" fluid in these layers is denoted by α. As the nanoparticle surface area increases, more fluid molecules interact with the solid to form these molecular layers. Thus, increasing the particle surface area increases α and decreases the proportion (1- α) of the

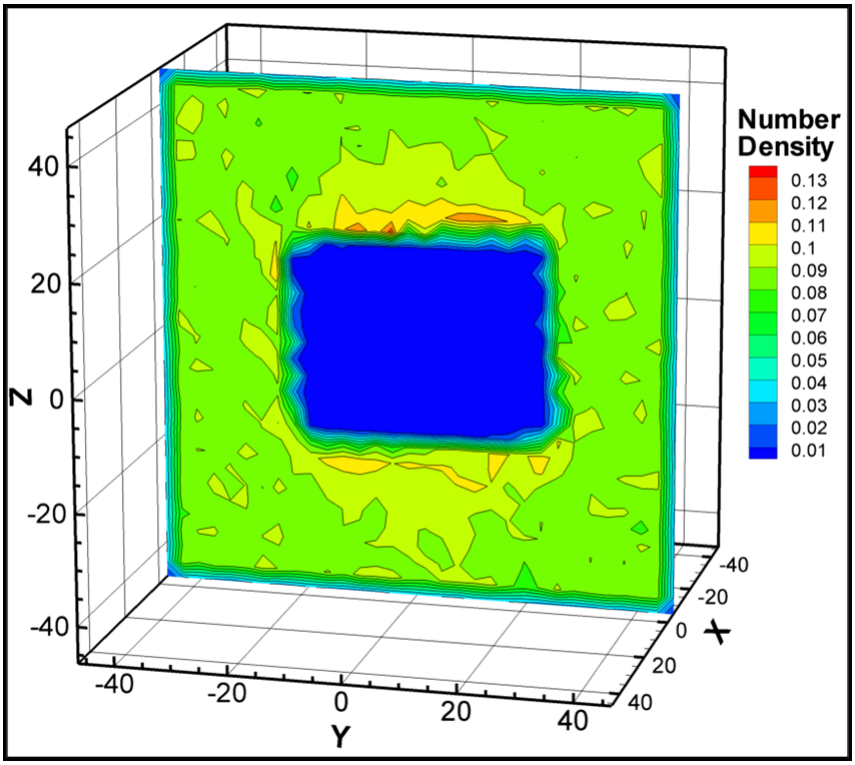

Figure 5.2: The number of water molecules per unit volume along a 0.3 nm thick y-z sectional slice of the system when $\phi = 0.96$. The higher number density at the surface of the solid particle confirms the adsorption of water on silicon dioxide. This effect, which diminishes away from the nanoparticle, increases the proportion of water molecules in the less mobile and more viscous fluid layers on the solid surface, and contributes to the enhancement in η_{fluid}.

more mobile free fluid that is located away from the nanoparticle surface, thereby enhancing η_{fluid}. This observation is also confirmed through the components of the shear viscosity along the surfaces of the nanoparticle. Table 5.1 reveals a direct correspondence between the surface area and viscosity. For instance, when $A_{xy} < A_{xz}$ for the nanoparticle, the effective viscosity of the fluid along those directions $\eta_{xy} < \eta_{xz}$.

The increase in the fluid viscosity can be represented by $\eta_{eff} = (\eta_{rel}$ - 1) = f(A, V, ϕ), where A denotes the total nanoparticle surface area and V its volume. A dimensionless area

$A^* = A/V^{2/3}$ is introduced to characterize the size effects of a nanoparticle on η_{fluid}. While $\eta_{eff} \propto \phi$ for smaller volume fractions, higher order terms provide more accurate predictions at large nanoparticle concentrations (Masoumi et al., 2009). Here, we propose the relation $\eta_{eff} = (A^*)^f(\phi + \phi^2)$ where f =(3 - d_f) is derived from the fractal dimension (d_f) (Prasher et al., 2006a,b) that accounts for the contribution of the quasi-crystalline fluid molecules. Approximating $d_f \approx 1.75$ (Prasher et al., 2006a,b), $\eta_{eff} = (A^*)^{1.25}(\phi + \phi^2)$.

Results from the model and the MD simulations are compared in Figure 5.3. At low volume fractions, when the effects of fluid layering on the solid nanoparticle are not pronounced, the model over predicts η_{fluid} due to the inclusion of the higher order term ϕ^2. There is excellent agreement between the two sets of results at larger ϕ. For a spherical nanoparticle, $A^* = 4.835$. Although A^* is constant for a specific nanoparticle geometry, an increase in the particle diameter (for a sphere) or length (for a cube) also increases ϕ, enhancing the fluid viscosity.

Aggregation occurs when the nanoparticle concentration in the suspension exceeds a critical value. This nanoparticle agglomeration creates an effective solid phase size that has as much as a 3× the characteristic dimension of an individual nanoparticle (Prasher et al., 2006b). Approximating $A^* = 3A/(3V)^{2/3}$ for such an aggregate of spherical nanoparticles and neglecting the higher order quadratic term, $\eta_{eff} \approx 11\phi$. This result is consistent with the experimental measurements of η_{fluid} for various fluids with spherical alumina suspensions of different diameters (Das et al., 2003; Prasher et al., 2006b; Wang et al., 1999), where the measurements provide $\eta_{eff} = 10\phi$ (Prasher et al., 2006b). The rheological behavior of fluids with suspended ceramic nanoparticles, like silica and alumina, show similar ϕ dependence in experiments (Tavman et al., 2008; Venerus et al., 2010). Thus, the model is able to reproduce the enhancement of η_{fluid} due to the variation in the shape and size of nanoparticles other than silica.

5.4 Summary

Increasing the silica nanoparticle size increases the shear viscosity of liquid water due to the layering of fluid atoms on the nanoparticle surface. MD simulations of this behavior agree

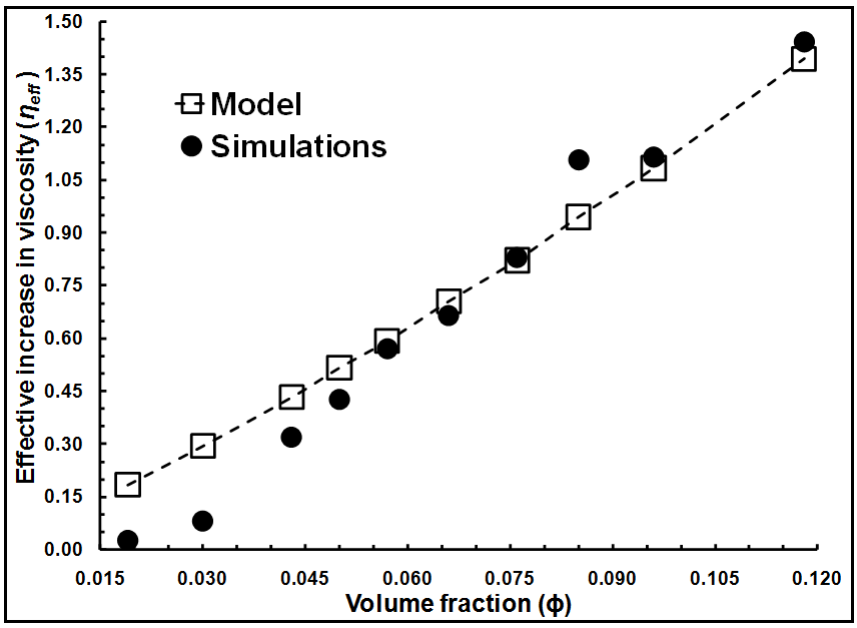

Figure 5.3: The shear viscosity η_{fluid} from the MD simulations of water containing different sizes (volume fractions) of the silicon dioxide nanoparticle compared against predictions of the proposed model. While the model predicts a larger value for η_{fluid} at low concentrations, the agreement is excellent at larger volume fractions.

with experimental measurements although minor differences exist due to the assumptions inherent to the simulations. A dimensionless area parameter is able to ascribe the enhancement in η_{fluid} to the coupled consequences of the particle shape, size and volume fraction. The model successfully reproduces the rheological behavior of fluid at large nanoparticle concentrations in accord with the MD simulations and previous experiments.

Chapter 6

Thermal conductivity reduction in materials: Effects of isotope substitution, mass disorder and binary systems

We introduce an analytical model to rapidly determine the thermal conductivity reduction due to mass disorder in nanomaterials. Although this simplified classical model depends only on the masses of the different atoms, it adequately describes the changes in thermal transport as the concentrations of these atoms vary. Its predictions compare satisfactorily with nonequilibrium molecular dynamics simulations of the thermal conductivity of ^{14}C-^{12}C carbon nanotubes as well as with previous simulations of other materials. We present it as a simple tool to quantitatively estimate the thermal conductivity decrease that is induced with isotope substitution in various materials.

G. Balasubramanian, I. K. Puri, M .C. Böhm and F. Leroy, under review

6.1 Tuning thermal properties of materials at the nanoscale

There is a growing interest in fabricating materials for sustainable energy applications that have a high thermoelectric efficiency at room temperature (Snyder and Toberer, 2008), e.g., to generate electricity from waste heat. The thermoelectric properties of a material can be improved by suitably tailoring its structure at the nanometer scale. This strategy allows for a significant reduction in the thermal conductivity of a nanostructured thermoelectric as compared to bulk materials (Galli and Donadio, 2010; Yu et al., 2010). When the characteristic dimension of these nanostructures approaches the phonon mean free path, the resulting perturbations in the lattice vibrations (phonons) that enable heat transport are larger than the corresponding variations in the electrical conductivity. This understanding has led to the development of nanomaterials such as nanowires, superlattices and solid thin films that have much smaller thermal conductivities in comparison with their bulk counterparts (Boukai et al., 2008; Hochbaum et al., 2008; Pernot et al., 2010; Tang et al., 2010; Venkatasubramanian et al., 2001). While perturbation of the phonon propagation is generally caused by different scattering mechanisms (Ashcroft and Mermin, 1976), phonon scattering in those materials mostly arises at the boundaries because of the large surface-to-volume ratio induced by the large extent of outer surface and interfaces.

Phonon scattering in silicon-germanium superlattice nanowires that have diameters of several tens of nanometers is dominated by atomic disorder (alloy scattering) rather than the surface scattering (Li et al., 2003). Thermal conductivity reduction through atomic disorder has been measured in various bulk materials including alloys and isotope mixtures (Cahill and Watanabe, 2004; Chang et al., 2006; Dismukes et al., 1964; Geballe and Hull, 1958; Inyushkin, 2002; Kremer et al., 2004; Morelli et al., 2002; Plekhanov, 2003). Even a small mass difference in these materials significantly changes their heat transport properties. For example, a change in the 13C isotope fraction from 0.07% to 1% in diamond can reduce the corresponding thermal conductivity by approximately 30% (Anthony et al., 1990). Therefore, we particularly consider the effects of mass disorder in nanostructured materials on the thermal conductivity as a strategy to reduce it.

This understanding has motivated several recent molecular dynamics (MD) simulations

which have dealt with heat transfer reduction in nanomaterials. In accord with experimental measurements, their predictions show that surface roughness and porosity play an important role in controlling the thermal conductivity of silicon nanowires (Chen et al., 2010; Donadio and Galli, 2009; Lee et al., 2008). MD simulations predict that the introduction of either silicon isotopes or germanium into the material lattice induces a thermal conductivity decrease relative to a pure silicon nanowire (Chen et al., 2009; Hu et al., 2011; Yang et al., 2008a; Zhang et al., 2010). Likewise, simulations of nanostructures with isotope defects also predict a thermal conductivity reduction in carbon based materials such as single walled carbon nanotubes (SWCNTs) (Maruyama et al., 2006; Zhang and Li, 2005), SWCNT superlattices (Shiomi and Maruyama, 2006), graphene sheets (Zhang et al., 2010) and nanoribbons (Jiang et al., 2010). Indeed, these show that the room temperature thermal conductivity can be reduced by almost an order of magnitude by simply doping the corresponding nanostructures with isotopes.

A theoretical framework for the heat transfer reduction that occurs due to mass disorder in lattices was defined more than fifty years ago by Klemens (Klemens, 1955) and Callaway (Callaway, 1959). They showed that a point defect that is induced by a mass difference in a crystal lattice causes phonon scattering. Moreover, if this mass-induced scattering dominates the whole phonon scattering, the lattice thermal conductivity is driven by the masses and concentrations of the individual isotopes that contribute to the disorder. More recently, ab initio methods and theoretical tools have been employed to analyze and predict the thermal conductivity of nanostructures, including those with mass disorder (Chantrenne et al., 2005; Kazan et al., 2010; Mingo et al., 2008; Savic et al., 2008; Stewart et al., 2009).

We propose a simple classical model based on mean-field approximations to evaluate the thermal conductivity variation in systems for which phonon scattering is induced through the presence of two different masses. The model requires only the masses of the different isotopes and their molar fractions, and does not contain adjustable parameters. It is able to correctly describe molecular dynamics predictions of the thermal conductivity reduction in carbon nanomaterials upon isotope substitution. Reasonably good agreement is also observed between our model predictions and recently published MD results for silicon crystals (Murakawa et al., 2004) and silicon-germanium nanowires (Chen et al., 2009). Since the model

readily predicts the thermal conductivity changes due to isotope substitution in nanomaterials at room temperature without resorting to complex calculations, its capability is also of practical interest.

We first present MD calculations of the classical density of vibrational states (DVS) of single walled armchair (10,10) carbon nanotubes containing different fractions of ^{12}C and ^{14}C isotopes at room temperature. Equipped with these results, we next introduce the classical model mentioned above. Finally, we validate the model using nonequilibrium MD simulations of ^{14}C isotope enriched CNTs and investigate its applicability by comparing its predictions with other MD results reported in the literature.

6.2 Equilibrium Molecular Dynamics simulations

MD simulations of 40 nm long (10,10) CNTs consisting of 6520 atoms were performed using the LAMMPS code (Plimpton, 1995). Periodic boundary conditions (PBCs) were applied in all directions so that the CNTs are essentially infinitely long in the z direction. The PBC applied along the z axis eliminates the effects of phonon-boundary scattering. The x and y dimensions of the simulation cell were large enough to prevent the tubes from interacting with their own periodic images in the lateral directions. Various fractions of ^{12}C atoms were randomly selected and replaced with ^{14}C isotopes. The Adaptive Intermolecular Reactive Empirical Bond Order (AIREBO) potential model was employed to reproduce the bonded interactions as well as the nonbonded Lennard-Jones dispersion-repulsion interactions (Brenner et al., 2002; Stuart et al., 2000). Each system was initialized at 300 K and simulated for 0.5 nanoseconds (ns) at 300 K and 1 atm. (NPT ensemble). We employ the Nose-Hoover thermostat and barostat, each with a coupling time of 100 femtoseconds (fs). This ensured that the CNT was free of internal stresses and relaxed to its appropriate thermodynamic density. Next, the canonical (NVT) ensemble was imposed and the system relaxed at constant temperature and volume for 0.5 ns after which the equilibrated CNT structure was obtained. All simulations used 1 fs timesteps.

Equilibrium simulations in the canonical ensemble at 300 K were used to calculate the classical DVS from the Fourier transform of the ensemble averaged mass weighted velocity

auto-correlation function (VACF) (Jobic et al., 2001). The equilibrated CNT structure was run for 1 ns with trajectories sampled every 100 picoseconds (ps). Each of these trajectories was independently simulated for 8.5 ps and the velocities were recorded every 1 fs. The time-translation invariance of the VACF was used to obtain a correlation over 8.192 ps by performing an average over 309 time origins. The average of all VACFs was Fourier transformed to obtain the DVS spectra with a 2.036 cm^{-1} resolution. In order to improve the signal-to-noise ratio of the Fourier transform, the VACFs were multiplied by an exponential function that had a characteristic decay time of 5 ps. Such a procedure is widely used in the treatment of the free induction decays in NMR spectroscopy (Keeler, 2005). This filtering function broadens the bands of the spectrum while appreciably decreasing the noise. Since the characteristic time was chosen to be close to the maximum time correlation of the VACFs, only a very slight broadening of the bands was observed.

6.3 Density of Vibrational States

The DVS spectra of the pure ^{12}C and ^{14}C nanotubes, as well as of a CNT with 40% of ^{14}C, are presented in Figure 6.1a. The spectra of the systems that contain the ^{14}C isotope are shifted along the y-axis for clarity. The general shape of the spectra corresponds to earlier reports (Alaghemandi et al., 2011). The structure with two broad profiles below 700 cm^{-1} arises mainly from the radial vibration modes of the CNT (Rao et al., 1997; Sanchez-Portal et al., 1999). The maximum around 1762 cm^{-1} in the pure ^{12}C nanotube corresponds to the fastest vibrational modes in the system that can be associated with more or less localized stretching modes of the carbon atoms around their equilibrium position. The localized nature of these high energy modes can be deduced from calculations in the momentum space (Sanchez-Portal et al., 1999). This boundary frequency can also be interpreted as the Einstein frequency of the CNT lattice, which corresponds to the frequency of an isolated atom vibrating in the potential energy surface generated by its local environment.

Figure 6.1b shows that the high energy modes shift towards lower wave numbers when the ^{14}C content increases. The high energy maximum of the DVS for a pure ^{14}C nanotube occurs at 1632 cm^{-1}. The height of this peak decreases until the content of ^{14}C is around

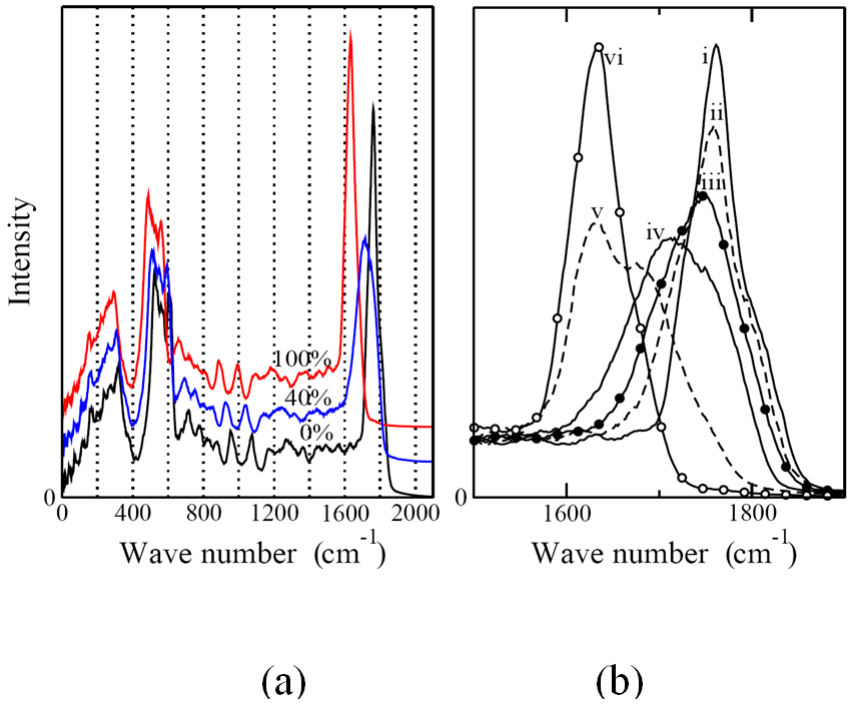

Figure 6.1: (a) Density of vibrational states (DVS) of CNTs containing 0% (black), 40% (blue) and 100% (red) of ^{14}C isotope, respectively. The spectra at 40% and 100% are displaced in the y direction in order to perform a convenient comparison. (b) DVS of the CNTs containing 0% (i), 10% (ii), 20% (iii), 40% (iv), 80% (v), and 100% (vi) of the ^{14}C isotope. The plot is restricted to the region between 1500 and 1900 cm^{-1}. The intensity in both plots is reported in arbitrary units.

50%, beyond which it increases again. This reduction correlates with a broadening of the high-energy DVS: it splits between 1762 and 1632 cm^{-1}. Thus, the results show that the local vibrational characteristics of a system with an intermediate content of isotopes are influenced by the mass disorder introduced in the network of atoms. While we have not presented the low frequency behavior of the DVS spectra in Figure 6.1b for the sake of visual clarity, we have observed the wave number shift to be smaller in the low frequency region than at higher frequencies.

6.4 A classical model based on mean-field approximation

The high energy maximum in Figures 6.1(a-b) for the two pure isotope CNTs corresponds to the more or less local modes described above. This can be illustrated through a simple model that predicts the change of the corresponding wave number when a system contains isotopes of different masses. In order to build this model, we compute the wave number of an isolated vibrating atom whose mass m_x is the average atomic mass in the system defined by

$$m_x = xm_\beta + (1-x)m_\alpha \tag{6.1}$$

where m_α and m_β denote the masses of the two isotopes α and β, and x the molar fraction of isotope β that has substituted isotope α in the structure. In the harmonic approximation, the wave number depends on the square root of the product of the force constant and the inverse of the mass of the considered atom. Since the system consists of isotopes with a similar electronic structure that can be described adequately in the Born-Oppenheimer approximation, we neglect the change in the local curvature of the potential energy surface (which yields the force constant) induced by the mass difference. The ratio between the wave number ν_0 at x=0 and ν_x for a specified fraction x of isotopes β is,

$$\frac{\nu_0}{\nu_x} = \sqrt{x\frac{m_\beta}{m_\alpha} + (1-x)} \tag{6.2}$$

Figure 6.2 presents the DVS spectra for systems with different contents of the ^{14}C isotope. The wave number axis of all the spectra is rescaled by the factor in equation 6.2. The spectra are also shifted along the y-axis for visual ease. It can be seen that the major changes in the DVS spectra occur in the high energy region beyond 1600 cm^{-1}. Nevertheless, the high energy spectra in the two pure systems coincide when the rescaled wave numbers are used. Moreover, all the rescaled spectra are generally similar in the region below 1600 cm^{-1} (with small differences in the DVS structure that are beyond the scope of this work).

The results show that approximately all the wave numbers in the system are influenced in a similar manner when ^{12}C is substituted with ^{14}C. This is consistent with the theoretical

Most of this section is attributed to my collaboration with Dr. F. Leroy, TU-Darmstadt

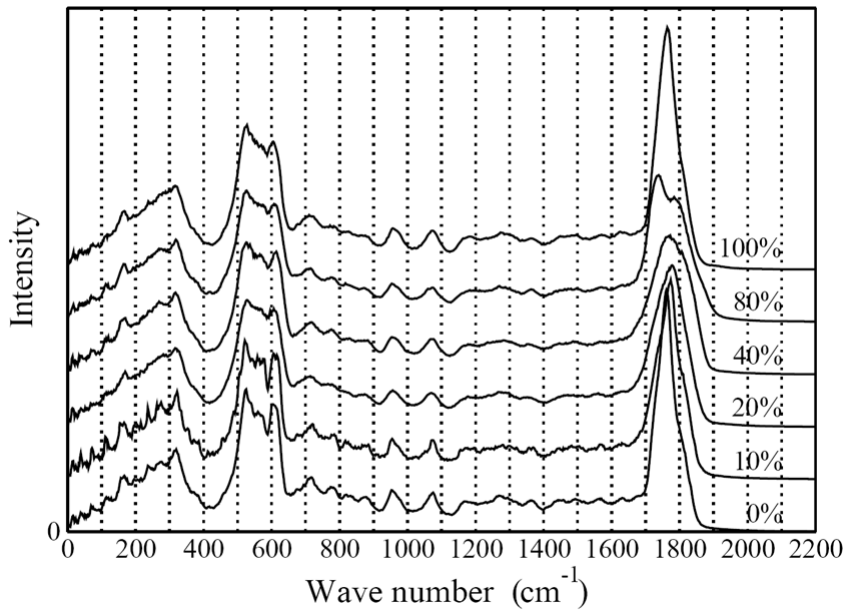

Figure 6.2: Density of vibration state spectra (DVS) of the CNTs containing 0%, 10%, 20%, 40%, 80% or 100% of ^{14}C isotope. The wave numbers are rescaled according to equation 6.2. The intensity in the plot is reported in arbitrary units.

finding that the mass disorder dominates the changes in vibrational properties for classical systems at high temperature (Klemens, 1960). We can conclude from the DVS spectra that the vibrational states of the isotope substituted CNTs can be roughly approximated as a set of weakly coupled harmonic oscillators with wave numbers that are determined by the average atomic mass in the system. Although such a rough estimate might imply that there is a monotonic variation of the thermal conductivity with respect to the isotope fraction, this variation is not monotonic, as will be shown later.

While energy transfer occurs through the vibrational modes of the system, the participation of the different modes can differ significantly (Donadio and Galli, 2009; Tan et al., 2011). Only the modes that are delocalized to a large extent can be expected to play an important role in heat conduction in crystal lattices. Even a small mass disorder is sufficient to prevent the formation of these perfectly delocalized modes that are most efficient for thermal transport. Thus, heat conduction is reduced by the presence of scattering sites

created through mass disorder, e.g., due to isotope substitution. We show in Figures 6.1 and 6.2 that fingerprints of these changes also appear in the high energy region of the vibrational modes. While these findings might support interpretations highlighting the importance of the localized modes for the heat transport in nanomaterials, we believe that this picture neglects the changes in the phonon modes in the low energy range. In a recent MD study of CNTs adopting the Boltzmann transport equation, it has been shown that delocalized low energy modes (< 700 cm^{-1}) account for most of the thermal conductivity (Donadio and Galli, 2009), which also agrees with our previous findings (Alaghemandi et al., 2011).

Both experimental measurements and the results of MD simulation obtained from the literature follow the typical features of Klemens' theory:

1. There is a substantial reduction in heat transfer upon isotope substitution even for materials with two isotopes that have similar masses,

2. The largest variation in the heat transfer reduction κ occurs for small isotope contents,

3. The maximum thermal resistance in binary systems occurs for an approximately equimolar mixture, and

4. A pure material made of the lightest isotope should have the highest thermal conductivity λ.

Only the difference in mass and the mass-defect molar fraction play a central role in Klemens' theory. It can also be deduced from these observations that short-range order in the mass defect distribution is irrelevant to the reduction of heat transfer. This is illustrated by the frequency scaling of the DVS spectra described in Figure 6.2. We conclude that a mean-field approximation is applicable to map the isotope effect on the heat transfer reduction in isotope enriched CNTs.

In the mean-field approach, the heat transfer rate $\dot{Q}_x$ through an isotope enriched CNT is assumed to be proportional to the frequency ω_x of an oscillator that is defined by two different bonded point masses $M_A(x)$ and $M_B(x)$. Thus, the heat transfer reduction,

$$\kappa(x) = \frac{\dot{Q}_x}{\dot{Q}_0} = \frac{\omega_x}{\omega_0} \tag{6.3}$$

M_A and M_B depend linearly on the isotope fraction, such that $M_A = xM_\alpha$ and $M_B = (1-x)M_\beta$ to account for the variation of molar fraction with M_α and M_β denoting effective masses. In the harmonic approximation, the frequency of such an oscillator is inversely proportional to the square root of its reduced mass μ, where,

$$\frac{1}{\mu} = \frac{1}{xM_\beta} + \frac{1}{(1-x)M_\alpha} \tag{6.4}$$

The cases when the effective oscillator describes the homogenous systems must be considered separately. An additional dimensionless parameter ϵ in equation 6.4 ensures that the inverse reduced mass does not diverge in the limiting cases of x=0 and x=1. Hence,

$$\frac{1}{\mu} = \frac{1}{(x+\epsilon)M_\beta} + \frac{1}{(1-x+\epsilon)M_\alpha} \tag{6.5}$$

In order to establish the association between the frequency of an oscillator containing two atoms and the CNT thermal conductivity λ, we assume that it is the alteration in the heat transfer through the oscillator that reduces the thermal conductivity. Hence, the value for $\kappa(x)$ for a binary mixture in comparison with a pure ^{12}C nanotube is obtained from the change in the average frequency of the effective oscillator, which follows from equation 6.5 as

$$\kappa(x) = \frac{\lambda(x)}{\lambda(0)} = \frac{\dot{Q}_x}{\dot{Q}_0} = \frac{\omega_x}{\omega_0} = \sqrt{\frac{\mu_0}{\mu_x}} = \sqrt{\frac{\epsilon(1+\epsilon)(1-x+\epsilon)M_\alpha + (x+\epsilon)M_\beta}{(x+\epsilon)(1-x+\epsilon)(1+\epsilon)M_\alpha + \epsilon M_\beta}} \tag{6.6}$$

Equation 6.6 is reminiscent of the factor in Klemens' theory (Klemens, 1955, 1960) that quantifies the effect of isotope mass disorder on thermal conductivity. We will show that this equation is able to reproduce the features of that theory as enumerated above.

The three parameters M_α, M_β and ϵ in equation 6.6 are determined from considerations made on the systems of isotopes. Three values of κ can be identified on the basis of the following limiting cases:

1. Since κ is expected to predict the heat transfer reduction in comparison to a pure system containing the lightest isotope, $\kappa(0)$=1 defines one limiting condition.

2. The second limiting case follows from our analysis of the DVS spectra: $\kappa(1)=(\frac{m_\beta}{m_\alpha})^{1/2}$.

3. The third value of κ is determined from the second situation where the local isotope distribution is approximately homogeneous. This is achieved when x is close to 0.5 for a mixture where isotopes are regularly distributed. In order to derive the reduction of the heat transfer rate in the vicinity of x=0.5, we use the following mean-field construction: We assume that a pair of identical isotopes contributes constructively to energy transfer. On the contrary, two different isotopes are assumed to have a destructive effect. The contribution of a pair of bonded atoms to the heat transfer rate is inversely proportional to the square root of the reduced mass of the pair, which corresponds to $m_x/2$ when x is approximately 0.5.

Finally, the average energy transfer rate σ_x at a specified isotope fraction x is obtained by adding the individual participations of each kind of possible pairs of bonded atoms. Each contribution is weighted by the probability that the given pair is found in the system so that,

$$\frac{\sigma_x}{\sigma_0} = \frac{\dot{Q}_x}{\dot{Q}_0} = \frac{1}{\sqrt{x\frac{m_\beta}{m_\alpha} + (1-x)}}\Big[x^2 + (1-x)^2 - x(1-x)\Big] \tag{6.7}$$

Equation 6.7 considers that the probabilities for an oscillator to consist of two α-type isotopes and two β-type isotopes are approximately x^2 and $(1-x)^2$, respectively, whereas the probability that an oscillator is made of two different isotopes is approximately $x(1-x)$. This relation can be employed to derive the expression for the heat transfer reduction $\kappa(x)$=σ_x/σ_0. The constraints $\kappa(0)$=1, $\kappa(1) = \sigma_1/\sigma_0$ and $\kappa(0.5) = \sigma_{0.5}/\sigma_0$ are used to numerically determine the complete set of parameters used in equation 6.6.

6.5 Nonequilibrium Molecular Dynamics simulations

Reverse nonequilibrium molecular dynamics (RNEMD) (Alaghemandi et al., 2009; Müller-Plathe, 1997) simulations were performed to probe the validity of the analytical model by computing the thermal conductivity of different CNTs. In RNEMD simulations, a steady heat flux is realized through the simulation cell by periodically imposing a kinetic energy exchange within specific regions of the system while the total energy and momentum are conserved. This imposed heat flux leads to a steady-state temperature gradient. Both the

imposed heat flux and the measured temperature gradient are used to obtain the thermal conductivity from Fourier's law provided that the thermal gradient is linear, i.e. linear response holds. The RNEMD simulations were performed over the 5 ns that followed the equilibration described previously. The RNEMD velocity exchange period parameter covered 300 timesteps. Temperatures and energy flux over the simulation cell were recorded every 1 ps, and a steady state was achieved by 3.5 ns. The last 1 ns of the simulation was used to determine the average thermal conductivity.

6.6 Results, discussions and comparison with literature

The simulated values of λ for different fractions of ^{14}C isotope are reported in Table 6.1. The variation in the thermal conductivity reduction factor $\kappa(x)=\lambda(x)/\lambda(0)$ upon isotope substitution is presented in Figure 6.3. The observed nonmonotonic behavior is in agreement with Klemens' theory and has also been reported in other MD simulations (Maruyama et al., 2006; Zhang et al., 2010). The scatter in the MD results arises because a single calculation was used to obtain λ for each system. Averaging over a set of calculations with a different spatial isotope distribution should suppress such fluctuations (Zhang and Li, 2005). Nevertheless, the simulation results are in very good agreement with the predictions from equation 6.6 which are also reported in Figure 6.3.

The addition of ^{14}C reduces λ until the CNT contains approximately a 50% molar fraction of this isotope, but the conductivity increases with increasing substitution beyond this fraction. We also compare the predictions of equation 6.6 with MD simulations of the thermal conductivity of other carbon materials in Figure 6.3. The model slightly overestimates λ for isotope substituted graphene nanoribbons (Jiang et al., 2010), but the overall agreement is still good. Our model is also able to predict $\kappa(x)$ for ^{13}C isotope substitution in graphene sheets (Zhang et al., 2010). Thus, the thermal conductivity behavior of isotope-substituted graphene is also well reproduced by equation 6.6. Figure 6.4a shows that equation 6.6 is also able to predict the MD simulation results for the thermal conductivity of binary mixtures of ^{28}Si, ^{29}Si and ^{30}Si isotopes in silicon crystals (Murakawa et al., 2004). This agreement seems to be an outcome of the very small differences between the masses of the isotopes.

Table 6.1: Variation in the thermal conductivity of a (10,10) carbon nanotube with respect to the fraction of ^{14}C isotope at room temperature obtained from nonequilibrium molecular dynamics simulations.

Percentage of ^{14}C isotopes	Thermal conductivity λ ($Wm^{-1}K^{-1}$)
0	173.16 ± 23.33
2.71	123.81 ± 11.57
5.24	85.60 ± 3.31
10.21	82.79 ± 2.92
12.63	79.55 ± 5.32
15.04	69.78 ± 3.26
20.53	63.65 ± 2.68
30.31	45.25 ± 1.67
40.82	38.51 ± 1.03
49.63	33.15 ± 0.73
60.06	41.53 ± 1.11
70.09	65.69 ± 3.04
79.65	74.32 ± 4.62
89.54	85.20 ± 5.21
100	114.83 ± 7.71

However, the thermal conductivity reduction in a (5,5) CNT (Maruyama et al., 2006; Zhang and Li, 2005) is reproduced poorly by our model (not shown here). While the model predicts a maximum reduction of 75%, the simulations report a maximum reduction of 40% at most. We implicitly assume in the parameterization of our model that the scattering induced by the mass defects can be described through the stretching mode between two bonded atoms. However, for structures with large curvature like (5,5) CNTs it may be necessary to explicitly consider the influence of bending or breathing modes to obtain a more precise description of the thermal transport (Sanchez-Portal et al., 1999). The absence of such effect in a two-center model could explain the disagreement between its predictions and the mentioned results for (5,5) CNTs.

A comparison of the model with experimental measurements is difficult because of the

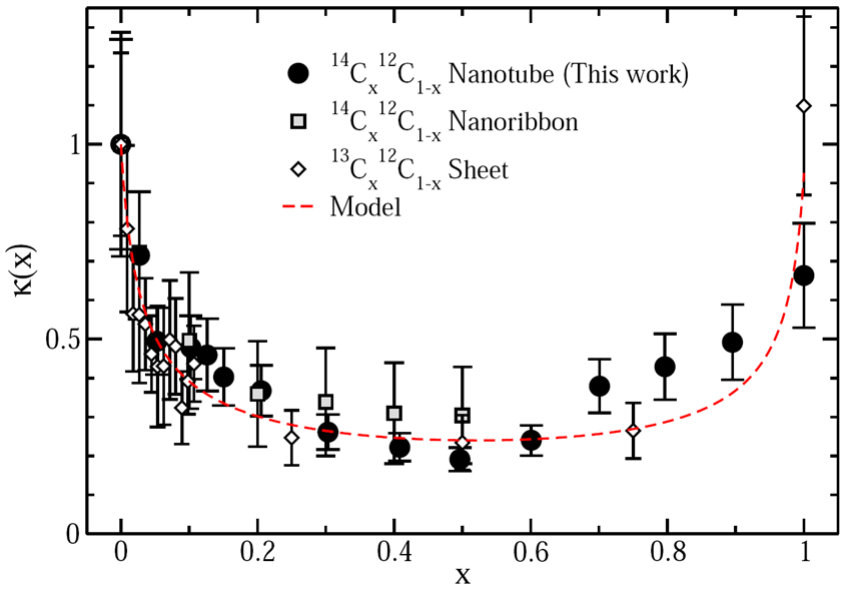

Figure 6.3: Comparison between our RNEMD calculations (filled circles), the heat transfer reduction model (dashed line), and previous simulations for graphene nanoribbons (Jiang et al., 2010) (open squares) and graphene sheets (Zhang et al., 2010) (open diamonds).

lack of data. Measurements for ^{12}C enriched diamond are restricted to a very small amount of ^{13}C isotopes (Anthony et al., 1990). Such substitutions produce a reduction of approximately 30-36% in λ while our analytical model predicts a decrease of about 19% as the ^{13}C isotope fraction is varied from 0.07% to 1%. When the fraction of ^{13}C is varied from 0.5% to 1% in the experiments, there is a 6-12% reduction in the conductivity while our model predicts a decrease of 10%. The experimental trend is in qualitative agreement with the results obtained from simulations for carbon and silicon materials.

We also evaluate the applicability of our model for systems in which the difference between the masses exceeds that between two typical isotopes of the same element. Here, we choose different elements from the same group in the periodic table. Figure 6.4b presents a comparison between our model predictions and earlier simulations of silicon-germanium nanowires (Chen et al., 2009). The dashed red line in Figure 6.4b is obtained from equation 6.6 by constraining the values of $\kappa(0)$, $\kappa(1)$ and $\kappa(0.5)$ as described above. Although the results for a low germanium content are good, this procedure yields a result that contra-

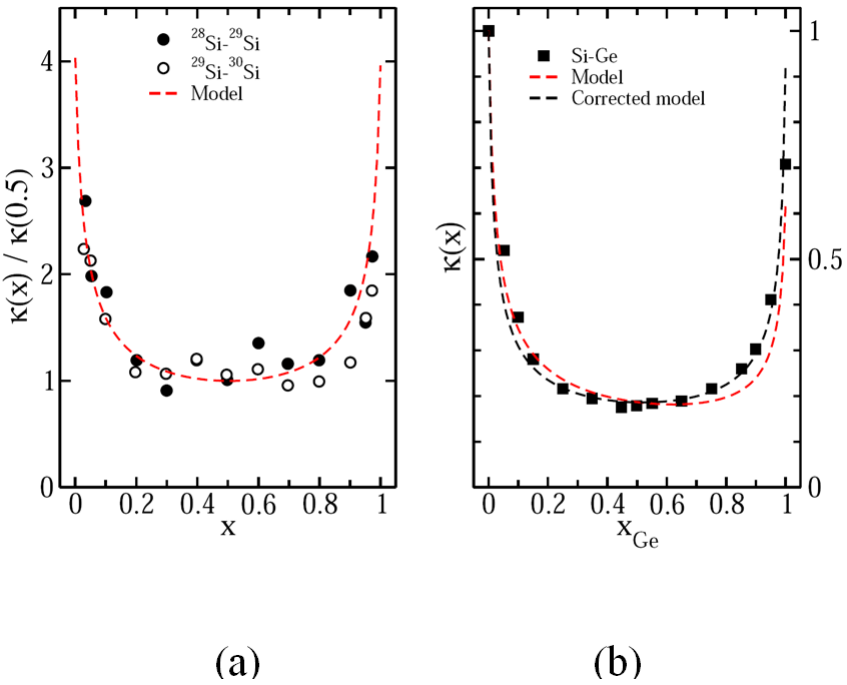

Figure 6.4: (a) Comparison between the model and the MD simulations of silicon crystals (Murakawa et al., 2004) with ^{28}Si and ^{29}Si with ^{29}Si and ^{30}Si substitution, respectively. x denotes the fraction of the lightest isotope, i.e. ^{28}Si or ^{29}Si. The ratio $\kappa(x)/\kappa(0.5)$ is presented instead of $\kappa(x)$ because data for the pure components are unavailable. The dashed red line corresponds to our model of equation 6.6. (b) Comparison between MD simulations in silicon-germanium nanowires (Chen et al., 2009) and the prediction of equation 6.6. The dashed red line is obtained from constraints on σ in equation 6.7, while the dashed black line is obtained from constraints on the first derivative of σ.

dicts the requirement of maximum thermal conductivity reduction (i.e. the minimum of κ) around x=0.5, as can be seen from the distorted shape of the red curve in Figure 6.4b. It is therefore more consistent to constrain the minimization of κ through its first derivative with respect to x. However, it is not possible to use the value of this derivative at x=0.5 since it yields a symmetric variation in κ with respect to x=0.5. Such mirror symmetry violates the constraint that the thermal conductivity of the lightest material should be larger than that of the heaviest. We therefore locate the minimum of κ at x_{min} for which the ratio

σ_{xmin}/σ_0 obtained from equation 6.7 is minimized. The new set of constraints is thus $\kappa(0)=1$, $\kappa(x_{min}) = \sigma_{xmin}/\sigma_0$ and $\mathrm{d}\kappa(x_{min})/\mathrm{d}x=0$. Moreover, $\kappa(1)$ becomes an output of the model. The resulting variation of κ(x), shown as the dashed black line in Figure 6.4b, improves the agreement with the simulations. The variation of $\kappa(x)$ in Figure 6.3 (carbon materials) and Figure 6.4a (silicon crystals) is not modified by the new set of constraints. This is because the previously observed distorted shape arises due to the large mass difference between silicon and germanium, while isotope systems are characterized by very similar masses.

Our model is also in qualitative agreement with recent simulations of silicon-germanium core-shell nanowires (Hu et al., 2011). That study found that germanium coatings reduce the thermal conductivity of silicon nanowires by 70-76%, which is similar to the maximum reduction predicted by our model in Figure 6.4b. The molar fractions of germanium in that study are in line with those corresponding to the smallest values of κ in Figure 6.4b. Furthermore, for a specified nanowire length, the thermal conductivity reduction for the Si/Ge composite in comparison with its uncoated silicon counterpart increases when the fraction of germanium increases. This trend is also predicted by our analytical model when the fraction of germanium is smaller than 50%. Finally, the reduction in thermal conductivity of the composite is somewhat insensitive to the nanowire length. This can also be explained with our model since increasing the nanowire length does not modify the ratio between silicon and germanium molar fractions. Therefore, the fraction of pairs of atoms which contribute either constructively or destructively to heat transfer remains the same.

6.7 Summary

We have derived a simple model that predicts the reduction in heat conduction due to isotope substitution and mass disorder in binary solid materials. The model which is purely classical and based on effective harmonic oscillator properties depends only on the masses of the isotopes. Our objective is to propose a tool that readily provides acceptable results rather than competing with more detailed theories. While it should be used with caution at low temperatures when quantum effects are likely to play a role, it is possible to decouple the temperature effect from the mass disorder effect (Klemens, 1960). In this case, the effect

of temperature can be subsequently included as a multiplying factor.

Chapter 7

Thermal conductivity of metallic alloys: A combined experimental and simulation study

We measure the thermal conductivity of Ni-18%Fe alloy using time-domain thermoreflectance (TDTR) measurements and molecular dynamics (MD) simulations. Experimental measurements provide the overall thermal conductivity. The simulations confirm that the contribution of phonon transport to this conductivity is much smaller than that due to free electron movement since phonons are internally scattered, which impedes lattice vibrations. In contrast, electrons are able to carry charges through the material unimpeded. Their movement is the dominant thermal transport mechanism. Its effect is more than an order of magnitude larger than that of the phonon thermal conductivity.

H.-H. Liao, G. Balasubramanian, N. C. Shukla, C.-H. Wu, L. Li, P. K. Liaw, I. K. Puri, and S. T. Huxtable, in preparation

Only the computational part of this research study is my contribution to the investigation

7.1 Electron and phonon contribution to thermal conductivity

While lattice vibrations, or phonons, are the major energy carriers in dielectrics, electrons dominate thermal transport in metals and conductors (Kittel, 2005; Nitzan, 2007). In metallic alloys, the presence of two or more interacting lattices increases phonon-phonon, phonon-electron and electron-electron collisions, which effectively reduces their thermal conductivity. We investigate the electronic and phonon contributions to the thermal conductivity of a nickel-iron (Ni-Fe) alloy using a combination of fundamental molecular simulations and experimental measurements to predict the influence of varying composition on the thermal transport through the material. Ni-Fe alloys are selected as the materials of interest because of their relatively low thermal expansion coefficient and favorable magnetic properties, which makes them strong candidates for applications such as thermostatic bimetals, glass sealants, electronic packages, and magnetic actuators (Cheng et al., 2010; Fan et al., 2006; Li et al., 2009; Suryanarayana, 1995; Suryanarayana and Koch, 2000). Their multifunctional properties make them useful for various applications where enhanced material performance, such as high strength, good tensile ductility, low thermal expansion and corrosion resistance are desirable.

7.2 Experimental measurements of Nickel-Iron alloy

A bulk nanocrystalline alloy containing Ni and 18% Fe (Ni-18Fe) by weight percent, fabricated by electrochemical deposition with a thickness of 3 mm in the deposition direction was acquired from Integran Technology Inc. The as-deposited alloy has a single phase with a face-centered-cubic (fcc) structure (Fan et al., 2006; Li et al., 2009). A transmission electron microscopy (TEM) image of the Ni-18Fe alloy is presented in Figure 7.1. While under planar projection the average grain size is roughly 25 nm, it is almost doubled in the cross sectional representation (Fan et al., 2006). The material exhibits a fiber texture (Li et al., 2009) in the deposition direction composed of ellipsoidal shaped grains. Twins are also observed within some grains in the TEM micrograph, which is due to the low stacking fault energy in the alloy. The presence of such grain boundaries in the alloy indicates that thermal transport must experience scattering at the grain interfaces in contrast with heat transfer in either Ni

or Fe in their pure homogeneous forms. Both of these metals are good electrical conductors so that thermal transport occurs due to both phonons and electrons.

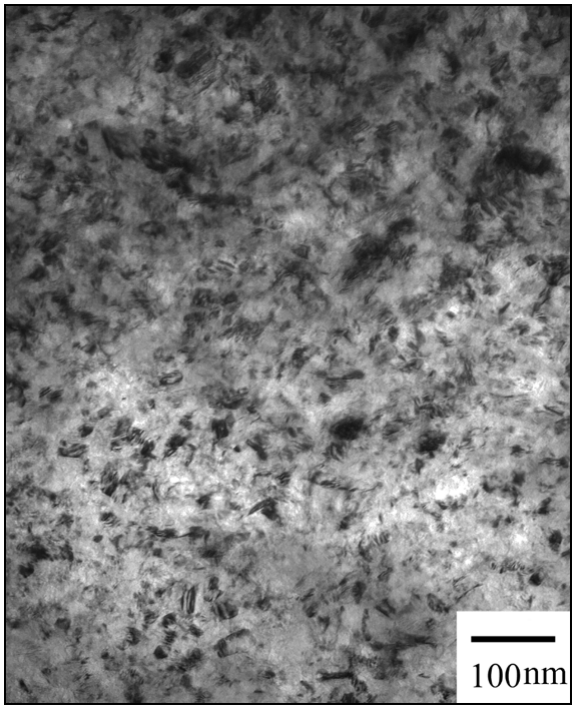

Figure 7.1: TEM micrograph of the Ni-18Fe specimen used in our experiments taken with the image plane perpendicular to the deposition direction.

The thermal conductivity, k, is measured using time-domain thermoreflectance (TDTR) (Cahill et al., 2003; Huxtable et al., 2004). TDTR is a pump-probe optical technique that measures thermal properties based on the reflectivity of a metal that depends slightly on temperature. A mode-locked ultrafast laser pulse with a repetition rate of 76 MHz and a 780 nm wavelength is split into pump and probe beams. The time-delayed probe beam reflects off an aluminum layer that coats the surface of the sample and into a photodetector, giving a measure of the temperature decay at the surface since the reflectivity of aluminum depends on temperature. Lock-in amplifiers measure the in-phase (V_{in}) and out-of-phase (V_{out}) signals from the photodetector. Interfaces are treated as thin layers (1 nm thick) where the interface conductance, G, is given by the ratio of the thermal conductivity to the thickness of the layer.

The thermal conductivity is extracted simultaneously by comparing the experimental data with a thermal model and adjusting k and G until the model matches the measurements (Cahill, 2004). The input parameters to the model include the thickness, heat capacity, and thermal conductivity for each layer in the sample. A Mira Optima 900-F ultrafast titanium:sapphire laser is split into two pump and probe beams with a 50:50 beam splitter. The pump beam heats the samples and the time-delayed probe beam measures the temperature decay of their reflectivities. The $1/e^2$ beam diameter (where the intensity falls to $1/e^2 = 0.135$ times the maximum value) of the pump beam on the sample is 27 μm. For the probe beam, it is 23 μm when the delay stage is at the home position and 25 μm at the end of delay stage that is about 600 mm away from the home position. A photodetector receives the in- and out-of-phase voltages passing through a lock-in amplifier in order to improve the signal-to-noise ratio.

The 3 mm $\times$ 3 mm $\times$ 0.7 mm sample is coated with a thin 93 nm aluminum (Al) layer which has a high thermoreflectance at 800 nm by using electron-beam evaporation, (PVD-250). The layer thickness is verified through an acoustic measurement based on the sound speed of 6420 m/s for Al. The volumetric heat capacity of the Ni-18Fe alloy, C, is required in order to extract its thermal conductivity. The value of $C = 3.88$ J cm^{-3}K^{-1} is determined using the Kopp Neumann Law. We use a laser modulation frequency f = 9.86 MHz and adjust k and G until the model matches the experimental measurements, which provides a value of $k = 26\pm15\%$ W m^{-1}K^{-1} for the Ni-18Fe alloy. The experimental data are shown in Figure 7.2 along with the "best-fit" curve for the TDTR model.

The electrical resistivity of a permalloy (80% Ni and 20% Fe by weight) has been found to be $\approx$ 165-196 Ω-nm at room temperature (298K) (Faltin, 2000), while our room temperature experiments on the Ni-18Fe sample reveal an electrical resistivity $\rho = 298$ Ω-nm. Thus, based on the Wiedemann-Franz law $k_e/\sigma = LT$, where σ denotes the electrical conductivity (inverse of electrical resistivity), T the temperature and the Lorentz number $L = 2.44 \times 10^{-8}$ W Ω K^{-2} (Stojanovic et al., 2010), the electronic contribution to the thermal conductivity $k_e \approx 24.35$ W m^{-1} K^{-1} for Ni-18Fe. Since k_e and k are of the same order, this confirms that free electrons that conduct charge through the alloy are the dominant thermal energy carriers. The contribution of phonons, which are scattered due to internal heterogeneity of

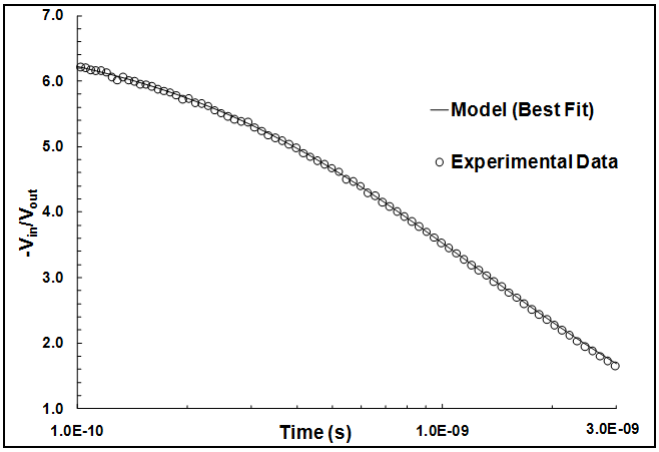

Figure 7.2: TDTR data for the Al/Ni-18Fe sample. V_{in}/V_{out} represents the ratio of the in-phase/out-of-phase voltages as measured by a lock-in amplifier. The data taken with the sample are used to determine the thermal conductivity of the Ni-18Fe layer. The solid lines represent the best fit curve from the thermal model. The models used identical material properties for Al, the Al/Ni-18Fe interface, and the Ni-18Fe layer.

the material, particularly at grain boundaries, is far smaller. Thus, varying the composition of the alloy should essentially only influence k_e.

7.3 Predictions from computations

We also employ detailed molecular dynamics (MD) simulations to support the above conjecture (Allen and Tildesley, 1987). Although the simulations only consider the thermal transport through phonons, their purpose is to show that the phonon thermal conductivity, k_{ph}, is much smaller than k and k_e. The value of k_{ph} is obtained from equilibrium MD simulations using the Green-Kubo method based on the fluctuation-dissipation theorem (Allen and Tildesley, 1987). The heat current vector S in such systems oscillates about zero at equilibrium and the thermal conductivity is correlated with the time required for these fluctuations to dissipate (Cahill et al., 2003; Chen, 2000b; Chen et al., 2010; Lukes et al., 2000; Schelling et al., 2002). Therefore, for a cubic isotropic material,

$$k_{ph} = \frac{1}{3k_B V T^2} \int_0^\infty \{< \vec{S_{ij}}(t)\vec{S_{ij}}(0) >\} dt \tag{7.1}$$

where k_B denotes the Boltzmann constant, V and T the system volume and absolute temperature, t the time, and $< \vec{S_{ij}}(t)\vec{S_{ij}}(0) >$ is the heat current autocorrelation function (HCAF). We determine k_{ph} from the converged values of the HCAF.

We eliminate system size effects on the bulk thermal conductivity (Cahill et al., 2003; Chen et al., 2010; Kulkarni and Zhou, 2006; Lukes et al., 2000; Sellan et al., 2010; Tang, 2004) by specifying a 14 nm $\times$ 14 nm $\times$ 14 nm cubic Ni-18%Fe alloy block that contains 256000 Ni and Fe atoms. Periodic boundary conditions eliminate phonon-boundary scattering and also ensure that the system is effectively infinite. Thus, the system is large enough to ensure that length scale effects do not influence the simulated k_{ph} values.

Multibody Embedded Atom Model (EAM) potentials (Bonny et al., 2009; Mishin et al., 2005) are employed to describe the interactions between the Ni and Fe atomic sites. The system is initialized at a temperature of 300 K and simulated for 0.5 nanoseconds (ns) at constant temperature and pressure (NPT ensemble) using a Nose-Hoover thermostat and barostat. This ensures that the Ni-18Fe block is free of internal stresses and relaxes the system to its appropriate thermodynamic density. Next, the canonical (NVT) ensemble is imposed and the system relaxes at constant temperature and volume for 0.5 ns after which an equilibrated system structure is obtained. Finally, equilibrium simulations are employed over the next 5 ns. The heat current values are sampled over every 0.02 picoseconds (ps) and the time correlation between them is calculated. All simulations are employed using the LAMMPS code (Plimpton, 1995). k_{ph} is calculated by averaging the thermal conductivities k_{xx}, k_{yy} and k_{zz} along the three orthogonal (x-y-z) directions of the cubic lattice. To accurately determine the HCAF integral, the simulation times should be much longer than phonon relaxation times of $\approx$ 100ps ($<$ 5 ns) (Lukes et al., 2000; Sellan et al., 2010).

Figure 7.3 presents the variations in k_{xx}, k_{yy} and k_{zz} values for which are obtained by integrating the HCAF over time. The thermal conductivity initially increases for $\approx$ 1 ns due to oscillations in the HCAF followed by a gradual decay to a constant value after $\approx$ 2.5 ns. The initial increase in k_{ph} is attributed to equilibrium fluctuations, which gradually

dissipate after being averaged over longer times. The time required for the fluctuations to recede, when a converged value of the HCAF can be determined, is directly proportional to the largest phonon relaxation time in the material (Sellan et al., 2010). Systems in which k_{ph} has a large contribution to k should therefore typically require simulations of $\bigcirc(\approx 10^1 - 10^2$ ns). This qualitative analysis leads us to predict that the contribution of phonons to k for Ni-18Fe is limited. The average value of the HCAF integral between 3.5-4.5 ns (which is the shaded region in the inset of Figure 7.3) is used determine $k_{ph} = 1.743$ $\mathrm{Wm^{-1}K^{-1}}$, a value that is much smaller than k_e. Making the material more internally heterogeneous, or incorporating other conductive impurities or materials in the alloy, should further lower k due to internal scattering between phonons and electrons (Murad and Puri, 2009b).

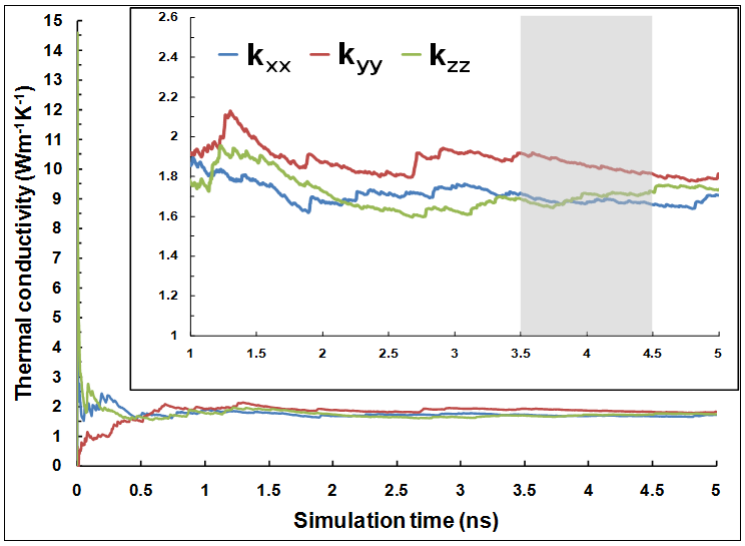

Figure 7.3: The phonon thermal conductivity over time evaluated by integrating the heat current autocorrelation function (HCAF). The thermal conductivity first increases along all three orthogonal directions (x-y-z), then decreases and becomes constant at longer times when the autocorrelation function decays to zero. The inset shows the time evolution of k_{xx}, k_{yy} and k_{zz} after 1 ns of simulation time when the variations in their values occur about an average value. The average Ni-18Fe k is sampled along the three orthogonal directions in the shaded region.

We simulate cases with 40% and 60% Fe by weight in the alloy to investigate the influence

of composition on the thermal conductivity, k_{ph} values for which are presented in Table 7.1. The overall k does not change significantly although k_{ph} is larger for the Ni-40Fe alloy. This indicates that while increasing the relative amount of Fe improves the capability of the material to transport thermal energy by phonons, when the amount is increased to 60% Fe, phonon-phonon scattering at a larger number of Ni-Fe interfaces significantly impedes energy transport.

Table 7.1: Thermal conductivity of Ni-Fe alloys obtained from MD simulations with 18, 40 and 60 weight percent of Fe, respectively.

Case	Weight% of Fe	Thermal conductivity ($Wm^{-1}K^{-1}$)
1	18	1.743
2	40	1.883
3	60	1.693

7.4 Summary

We have examined the thermal conductivity of Ni-18%Fe alloy through TDTR measurements and equilibrium MD simulations. The prime contribution to the bulk thermal conductivity is due to the movement of free electrons in the alloy rather than phonon transport, which is more than an order of magnitude smaller. This trend indicates that while internal phonon scattering at Ni-Fe interfaces impedes the thermal energy transport, electrons are still able to efficiently transport this energy in the electrically conducting material. Varying the fraction of Fe in the alloy can increase k_{ph} by a small but not significant amount.

Krishna Vummidi, Department of Electrical Engineering at Virginia Tech, encouraged and supported us in the experimental part of this work.

Chapter 8

Interfacial thermal resistance: Temperature discontinuity across contact surface of dissimilar materials

Nonequilibrium molecular dynamics simulations are employed to simulate unsteady nanoscale thermal transport at a solid-fluid interface by placing cooler liquid-vapor argon (Ar) mixtures adjacent to warmer iron (Fe) walls. The Ar-Fe intermolecular interactions induce the migration of fluid atoms into quasi-crystalline interfacial layers adjacent to the walls, creating vacancies at the migration sites. This induces temperature discontinuities between the solid-like interfaces and their neighboring fluid molecules. The interfacial temperature difference and thus the heat flux decrease as the system equilibrates over time. The averaged interfacial thermal resistance $R_{k,av}$ decreases as the imposed wall temperature T_w is increased as $R_{k,av} \propto T_w^{-4.8}$. The simulated temperature evolution deviates from an analytical continuum solution due to the overall system heterogeneity.

G. Balasubramanian, S. Banerjee and I. K. Puri, Journal of Applied Physics 104 (6), 064306 (2008)

8.1 Background and objectives

Since the length scales associated with nanostructures are comparable with those of the energy carriers that facilitate thermal transport, the corresponding nanoscale properties are different from those at the continuum. The role of the interfacial resistance (Swartz and Pohl, 1989) during nanoscale thermal transport thus also differs from its characteristics at larger scales (Cahill et al., 2003). Moreover, the structural details of a nanoscale interface have a significant influence on the local thermal properties (Chaudhuri et al., 2007; Murad and Puri, 2008b). The attraction of liquid molecules to hydrophilic surfaces promotes structural ordering at interfaces, which enhances the local thermal conductivity (Henderson and Vanswol, 1984; Murad and Puri, 2008b). There is also evidence that the local intermolecular interactions can introduce temperature discontinuities across these interfaces (Khare et al., 2006). Kapitza first discussed the existence of an interfacial contact resistance during heat transfer between liquid helium and heated metal surfaces such as copper and lead (Kapitza, 1941). The interfacial (Kapitza) resistance,

$$R_k = \Delta T / \dot{q} \tag{8.1}$$

represents the ratio of the temperature drop at the interface to the normal heat flux across it (Barrat and Chiaruttini, 2003; Pollack, 1969). Thermal transport across nanoscale solid-liquid interfaces, e.g., those formed when nanoparticles and nanostructures are immersed in fluids, is also influenced by the locally large surface area to volume ratio (Eastman et al., 2004).

Atomistic simulations, such as those based on molecular dynamics (MD) which is a fundamental technique rooted in the principles of classical mechanics (Poulikakos et al., 2003), can help explain interfacial effects (Murad and Puri, 2007a,b) during nanoscale thermal transport (Xue et al., 2003). Examples of such MD studies include investigations of heat transfer between simple solid-liquid interfaces (Murad and Puri, 2008b; Wang et al., 2007a) and of the bonding between liquid and solid atoms (Xue et al., 2004). These simulations have been limited to steady state investigations of nanoscale thermal transport across interfaces (Chaudhuri et al., 2007; Khare et al., 2006; Maruyama and Kimura, 1999; Wang et al., 2007a). Another limitation is that the heat flux is not typically determined in these simulations explicitly, but

rather a posteriori using the empirical Fourier heat conduction law (Maruyama and Kimura, 1999). In order to address these two issues, a nonequilibrium molecular dynamics (NEMD) approach is employed to investigate the transient thermal transport across a nanoscale interface in which the values of $\dot{q}$ are explicitly determined.

8.2 Simulation details

Table 8.1: Lennard Jones interaction parameters for Fe and Ar.

Interaction sites	ϵ (eV)	σ (Å)
Ar-Ar	0.0103	3.4
Ar-Fe	0.0516	3.7

The interaction between a metal and an inert element is usually represented in MD simulations through a potential function, e.g., the LJ potential, shown earlier (Equation 4.1) The Ar-Ar and Fe-Ar interactions are modeled with LJ parameters, values of which are listed in Table 8.1 (Lummen and Kraska, 2004). MD simulations have also been able to reproduce the temperature discontinuities across solid-liquid interfaces by modeling the solid atoms with a harmonic potential function (Maruyama and Kimura, 1999; Ohara and Suzuki, 2000). While this is a better representation than the LJ model which tethers solid atoms to their respective equilibrium positions, the even more realistic Embedded Atom Model (EAM) which incorporates many-atom interactions (Daw et al., 1993; Mendelev et al., 2003) that are otherwise neglected in a pair-potential scheme (Johnson and Oh, 1989) are employed. For the EAM model, the total energy of a system of atoms is

$$E = \sum_i \left[F_i(\bar{\rho}_i) + \frac{1}{2} \sum_{j(\neq i)} \Phi_{ij}(R_{ij}) \right] \tag{8.2}$$

where the summation occurs over the atoms i and j. The embedding function F_i denotes the energy required to embed an atom of type i into the background electron density at the site ρ_i, and Φ_{ij} represents the pair-interaction between atoms i and j whose separation is R_{ij}. Here, the electron density of the solid is considered to be a linear superposition of the

densities of the individual atoms. The relevant parameters for the EAM model are obtained from the literature (Mendelev et al., 2003).

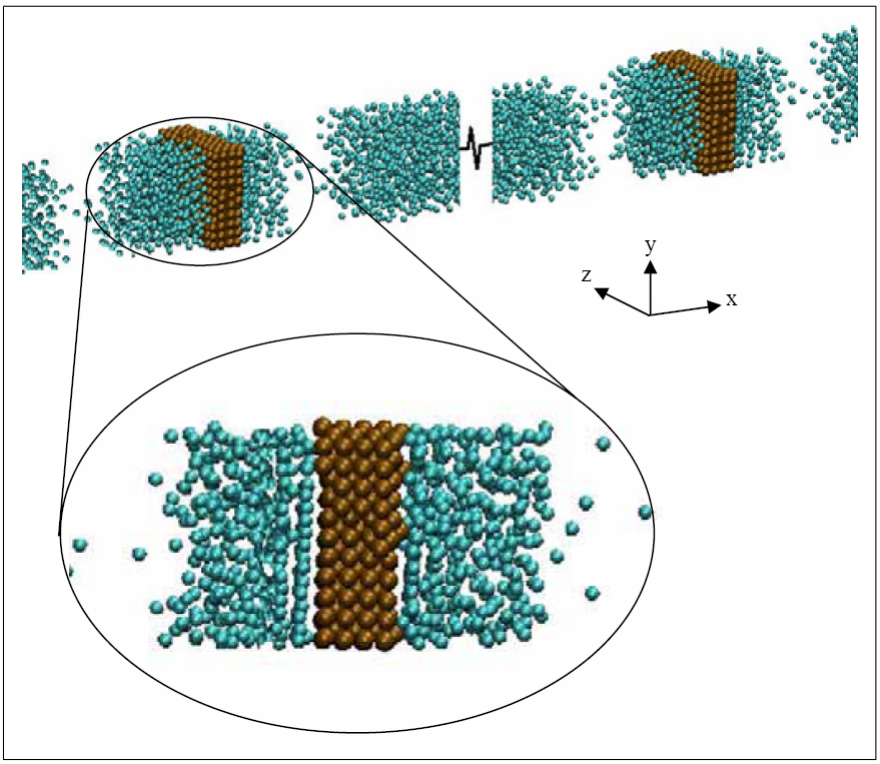

Figure 8.1: A 3-dimensional view of the MD simulation domain in which Ar (cyan) fills a space of 280 Å between two 10 Å thick blocks of solid Fe. Fluid atoms on both sides of the walls indicate periodicity. A close-up orthographic view shows the observed Ar-atom layering at the solid-fluid interface.

The simulation configuration is described in Figure 8.1. The 30 Å × 30 Å × 580 Å cuboid contains two 30 Å × 30 Å × 10 Å Fe blocks that restrain a liquid-vapor Ar mixture (with an initial 33% vapor volume fraction) between them. These solid Fe blocks extend from 140-150 Å and 430-440 Å along the $x-$direction. The Ar liquid-vapor mixture consists of 3402 atoms that initially form a face centered cubic (fcc) lattice which equilibrates through the simulations. Periodic boundary conditions apply in all directions to eliminate wall effects so that the system is essentially infinite. The cut-off distance for the LJ interactions between both the metal-fluid and the fluid-fluid atoms is 10 Å, or roughly 3 molecular diameters.

Linear momentum is conserved for each simulation by subtracting the center of mass velocity of the group of solid atoms in each wall from each Fe atom within the group. Likewise, the center of mass velocity in each fluid reservoir is subtracted from each Ar atom in that reservoir. The number of atoms, total volume and temperature of the solid walls in the closed system are held constant during the entire simulation.

The system is initialized at a temperature of 100 K. During the first 300 picoseconds (ps), a velocity-rescaling temperature control is applied for all atoms. This ensures an initial equilibrium state for which the entire system is at a uniform temperature. Subsequently, for the next 700 ps, the temperature of the solid atoms is controlled while fluid atoms are allowed to behave freely and equilibrate. At 1000 ps, the Fe blocks are provided with a step increase to a higher temperature, which is thereafter maintained with constant velocity rescaling for the remainder of the simulation. The temperature of the Fe atoms is maintained by rescaling their velocities (i.e., their translational movement), but keeping the overall kinetic energy constant. The instantaneous temperature $T = \frac{2}{nNk_B} \sum_{i=1}^{N} \frac{1}{2} m v_i^2$, where n denotes the molecular degrees of freedom (=3 for a monatomic molecule), k_B the Boltzmann constant, N the number of atoms, m the atomic mass, and v_i the instantaneous velocity of an atom. The specified wall temperature $T_{w,s}$ is maintained by rescaling the velocity of each atom according to the relation $v_i^{new} = (\frac{T_{w,s}}{T})^{1/2}$. Thereafter, the simulation is continued with the modified velocities. All the MD simulations are based on the massively parallel LAMMPS code (Plimpton, 1995) with successive 0.1 femtosecond time steps.

8.3 Results and their implications

The fluid domain is divided into several 4 Å thick slabs along the x-direction for the purpose of spatial characterization, and the density and temperature distributions within them are sampled at uniform time intervals. Figure 8.2 presents the averaged number density distribution of the Fe and Ar atoms when both Fe blocks are maintained at 120 K. The figure shows that the fluid atoms adjacent to the solid walls migrate closer towards them due to the Fe-Ar intermolecular interactions to form discrete interfacial layers in agreement with previous investigations (Maruyama and Kimura, 1999; Murad and Puri, 2008b; Ohara

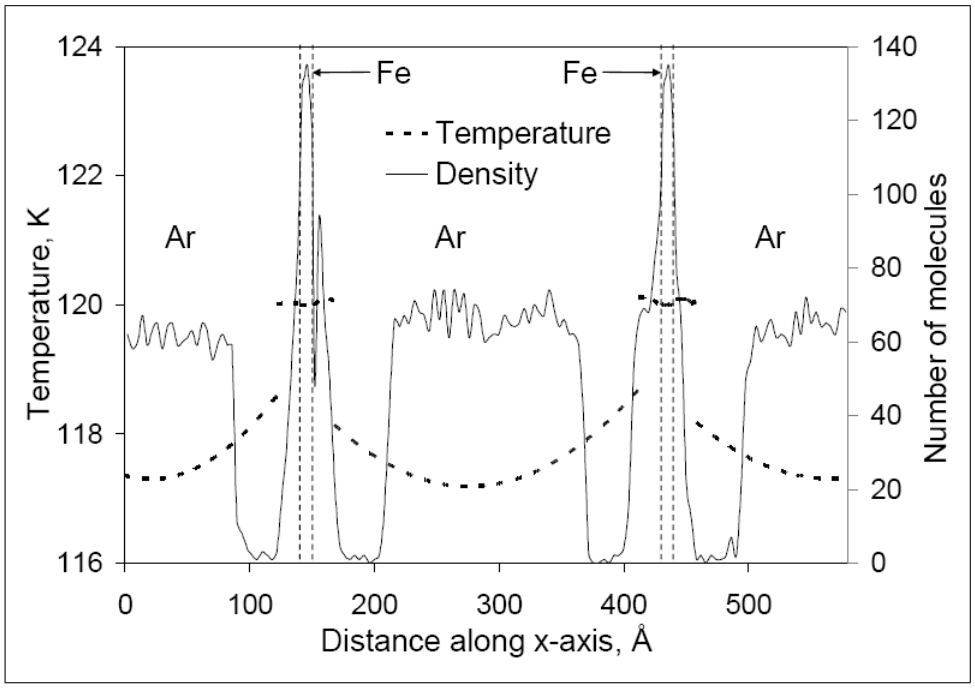

Figure 8.2: The temperature (dotted line) and density (solid line) distributions across the $x-$wise direction after the system nears its steady state. The solid Fe walls are located between 140-150 Å and 430-440 Å.

and Suzuki, 2000; Xue et al., 2003, 2004). The consequent higher Ar atom density at the interface causes a local increase in the interfacial pressure so that the packed fluid layers are quasi solid-like. Since the fluid is initially a liquid-vapor mixture, this inhomogeneous density distribution occurs due to phase segregation. Ar atoms that are further removed from the walls do not experience the wall-vapor intermolecular attraction and thus remain homogeneously distributed. In contrast, the migration of the fluid Ar atoms towards the walls to form the quasi-crystalline layers from proximal vapor-containing regions that are a few molecular diameters removed from the interfaces creates local vacancies. Essentially, Ar atoms closest to the walls exhibit a denser and more packed quasi-crystalline behavior, those further removed from the interfaces behave as fluid, with vacancies separating these two regions.

Figure 8.2 also presents the average temperature (based on a local equilibrium approximation) of each 4 Å thick slab in the domain. The Ar atom layers adjacent to each wall have

a temperature nearly equal to that of the solid. This is followed by a sharp temperature drop in the fluid extending from approximately four molecular layers away from each wall (Freund, 2005; Murad and Puri, 2008b). The Ar atoms in the four molecule thick interfacial regions show little tendency towards significant translational motion since, being attracted to the Fe atoms, they are held relatively immobile. These quasi-crystalline Ar layers have a higher effective thermal conductivity than atoms in the corresponding fluid phase (Freund, 2005). In contrast to fluid behavior at the continuum scale, a significant temperature discontinuity occurs in the vacancies that follow the interfacial Ar atom layers, since energy transfer through these sparsely populated regions is hindered. The thermal properties of nanoscale structures depend upon the length scales of the energy carriers (for example, thermal phonons) and the system dimensions. Hence, if a domain is much larger than the mean free path of the energy carriers, only then is continuum theory expected hold outside the interfacial region.

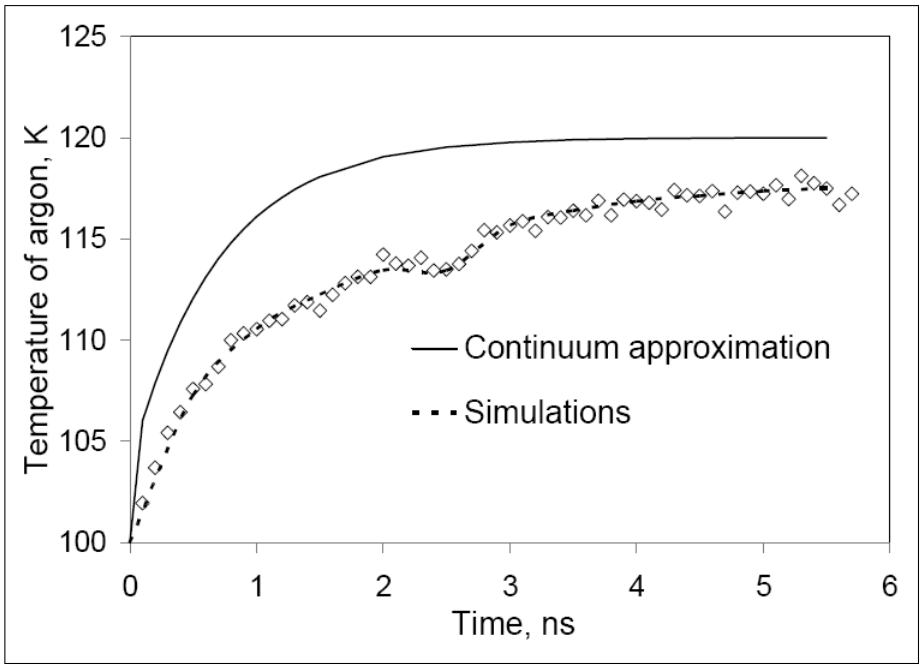

Figure 8.3: The temporal evolution of the fluid temperature obtained explicitly from the simulations and empirically from an analytical solution to Fourier's law of heat conduction (assuming homogeneous and constant properties).

Figure 8.3 presents the temporal evolution of the characteristic fluid temperature, which

is averaged over all slabs, as the simulation proceeds from its initial thermodynamic nonequilibrium state to a steady state. An analogous average temperature can also be obtained from the analytical solution of the continuum Fourier heat equation

$$\frac{\partial \theta}{\partial \tau} = \frac{\partial^2 \theta}{\partial X^2} \tag{8.3}$$

where θ denotes a dimensionless temperature $\frac{T(x,t)-T_w}{T_i-T_w}$, τ a dimensionless time $\frac{\alpha t}{L^2}$. Here, $\alpha = 1.12 \times 10^{-7}$ m^{2}s^{-1} denotes the bulk Ar thermal diffusivity at the initial system temperature T_i of 100 K, L the length of the domain in the $x-$direction and X a dimensionless length $\frac{x}{L}$. The boundary conditions correspond to fixed wall temperatures T_w. The solution follows the expression $\theta(X,\tau) = \sum n = 1^{\infty} \frac{2}{n\pi}(1-\cos(n\pi))\sin(n\pi X)e^{-n^2\pi^2\tau}$.

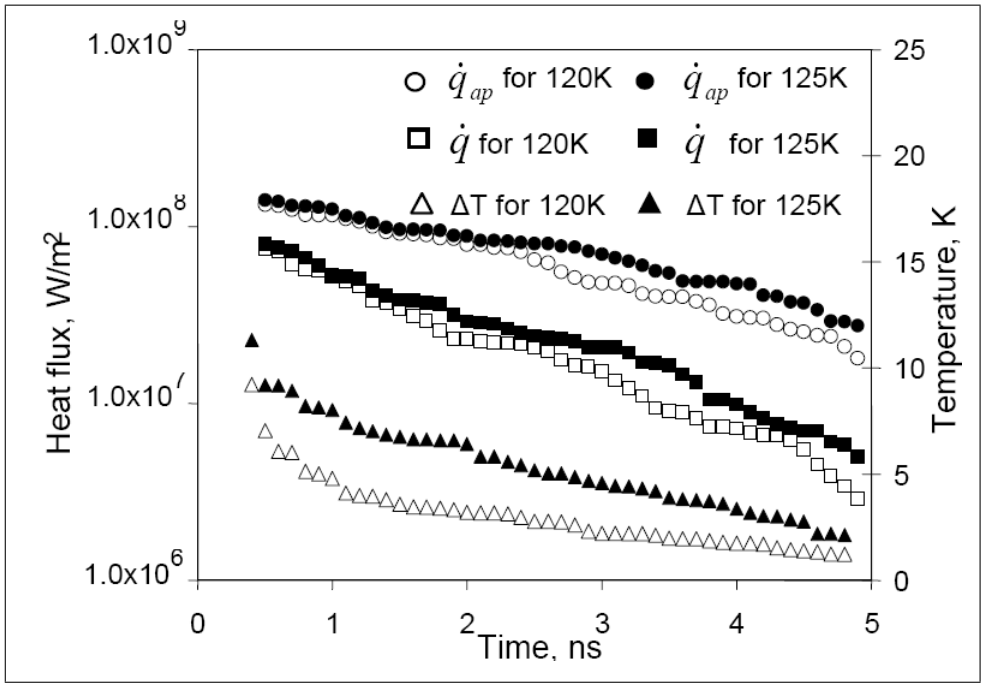

Figure 8.4: The temporal evolution of the heat fluxes calculated using first principles and a quasi-continuum approach, and the interfacial temperature drop for two different wall temperatures of 120 and 125 K.

The response of the MD simulations to thermodynamic disequilibrium differs from that of the analytical continuum solution. The simulation provides evidence of nonequilibrium effects even after 5000 ps whereas the analytical solution equilibrates by 3000 ps. More-

over, Figure 8.3 also shows that the bulk temperature temporarily stabilizes after $\approx$ 2500 ps. This occurs due to a temporary departure from the quasi-crystalline interfacial layering of Ar atoms as the system equilibrates. This reordering impedes heat transfer for $\approx$ 200-400 ps so that the fluid temperature remains virtually constant. Thermal transport resumes following the molecular rearrangement, but at a slower rate. In contrast, the continuum analysis assumes homogeneous system properties for all times, although the simulation results presented in Figure 8.1 and 8.2 contain evidence to the contrary. The source for the discrepancy between the continuum analytical solution and the MD simulations is attributed to the heterogeneous system characteristics due to the interfacial layering of Ar atoms. This provides emphasis for the assertion that for values of the heat flux to be accurate, these must be determined explicitly from nanoscale simulations rather than implicitly using empirical continuum relations. If an appropriate system-specific correction factor for the bulk thermal conductivity is incorporated, the results from continuum theory can be expected to agree with the simulations.

It is typical to determine the heat flux across nanoscale interfacial layers using a bulk thermal conductivity, i.e., by essentially making a quasi-continuum approximation. Instead the net energy flux $\dot{q_{sl}}$ from the solid molecules s to the fluid molecules l is explicitly calculated using $\dot{q_{sl}} = \frac{\dot{E_{ls}} - \dot{E_{sl}}}{2}$, where $\dot{E_{ls}}$ and $\dot{E_{sl}}$ denote the energy fluxes from the liquid to solid and solid to liquid phases, respectively (Ohara, 1999). With this approach, the total thermal energy transferred from a high temperature wall to the low temperature fluid adjacent to it is $\dot{q} = \sum_s \sum_l \dot{q_{sl}}$, which also allows us to determine R_k (Equation 8.1) explicitly from the simulation. Further, assuming for a specified mass $m = N_{Ar} M_{Ar}$ that the approximate energy flux $\dot{q_{ap}} = \frac{mc}{A} \frac{dT_{av}}{dt}$, where N_{Ar} and M_{Ar} denote the number of Ar atoms in the system and their molecular mass, A the interfacial area through which heat flows, c the constant volume specific heat of Ar, and T_{av} the average fluid temperature, an expression for the approximate Kapitza resistance $R_{k,ap} = \frac{A}{mc} \frac{\Delta T}{dT_{av}/dt}$ is obtained.

The temporal variations of the heat fluxes, based on both the explicit and approximate approaches, and the temperature drops across the quasi-crystalline Ar atom interface are presented in Figure 8.4 for two initial wall temperatures of 120 and 125 K. The behaviors of $\dot{q}$, $\dot{q_{ap}}$ and ΔT are similar for the two different initial wall temperatures. Since the temperature

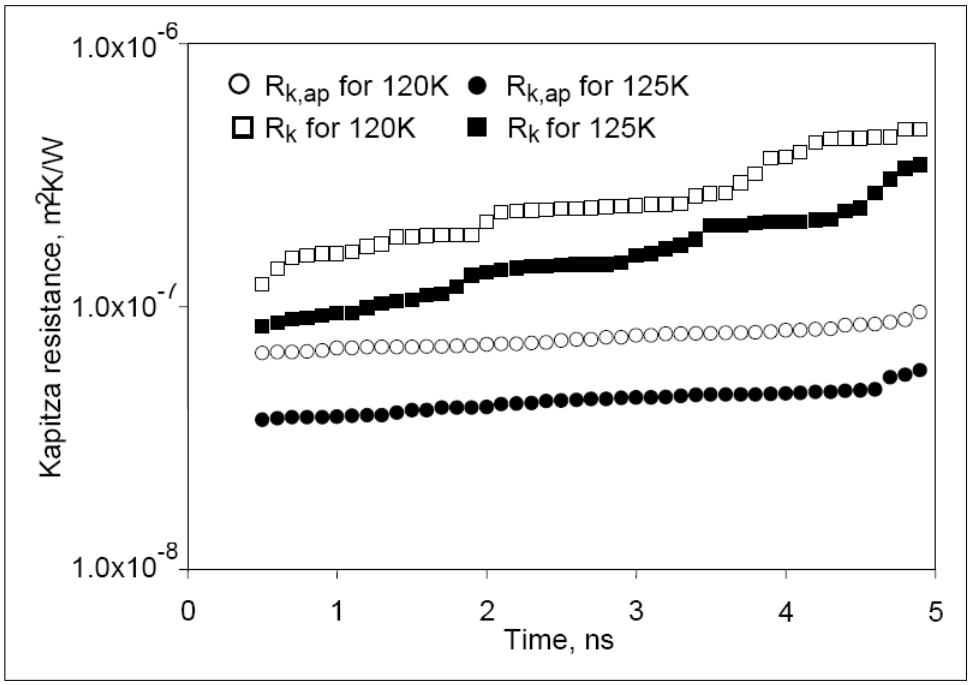

Figure 8.5: The temporal evolution of the interfacial thermal resistances for two wall temperatures of 120 and 125 K (based on heat fluxes calculated using a first principles and a quasi-continuum approach). The interfacial temperature drop is the same for both methods at any instant and is calculated as a time average over 100 ps.

difference across the interface, which is the driving potential for heat transfer, diminishes over time, so does the heat flux from the high temperature solid to the equilibrating fluid for each case. Notably, there can be an almost one order of magnitude difference between the heat flux values predicted explicitly by the simulations and the approximate method.

Figure 8.5 presents the temporal variation of R_k and $R_{k,ap}$ when the temporal values of ΔT are identical. Again, there is an almost an order of magnitude difference in the values of these two interfacial resistances. Their behaviors are similar although their rates of increase are different. The interfacial thermal resistance increases over time, since the decrease in the heat flux is greater than the decrease in the value of ΔT.

The influence of wall temperature on the thermal resistance is also examined. For each simulated case, the value of ΔT is averaged over the period from 2000-4000 ps, and the heat flux $\dot{q_{av}} = \frac{1}{2000} \sum_{i=200ps}^{400ps} \dot{q}_i$ to determine the average interfacial resistance $R_{k,av}$, which

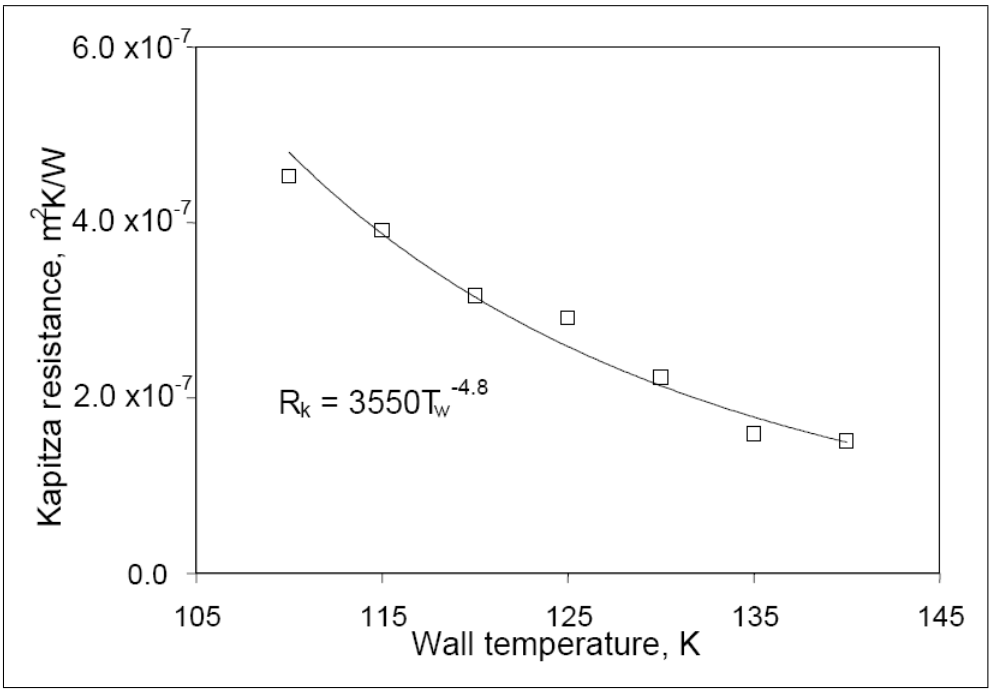

Figure 8.6: Change in the Kapitza resistance (based on heat fluxes calculated using a first principles approach) with respect to varying wall temperature. The fluxes and temperature drops are averaged over 2000-4000 ps.

is presented in Figure 8.6 with respect to increasing wall temperature T_w. As T_w increases, the pressure within the fluid and hence on the quasi-crystalline layers rises. Consequently, the interfacial molecular layers become more closely packed and the local intermolecular interactions are enhanced. Hence, thermal transport through these layers also increases, leading to a decrease in the interfacial thermal resistance according to the relation $R_{k,av} \propto T_w^{-4.8}$.

8.4 Summary

Unsteady nanoscale thermal transport differs from that at the continuum scale. It takes longer for a nanoscale system to respond to an imposed temperature difference than predicted by an analytical continuum solution. The steady state temperature distribution between the quasi-crystalline fluid interfacial layers adjacent to a solid wall and the rarefied fluid-

side vacancy-containing region following these layers exhibits a discontinuity due to phase segregation in the fluid. As the average temperature difference between the warmer interface and cooler fluid equilibrates over time, the heat flux also decreases. The resistance to heat transfer increases over time, since the heat flux decreases more rapidly than does the average temperature difference. Overall, the interfacial thermal resistance decreases with increasing wall temperatures as $R_{k,av} \propto T_w^{-4.8}$.

Chapter 9

Bridging length scales for interfacial thermal transport: A heterogeneous model

Thermal transport in solids occurs through the propagation of lattice vibrations, or phonons. Phonons scatter and travel ballistically in systems that are smaller than the phonon mean free path. At length scales larger than the phonon mean free path, the transport process is instead predominantly diffusive. We employ molecular dynamics (MD) simulations to describe the length dependence of Ge thermal conductivity, which manifests due to the two different modes of heat transfer across length scales. Molecular simulations for a Si-Ge superlattice are able to represent the acoustic mismatch that creates an interfacial thermal resistance R_k, which is unaccounted for in a continuum model. R_k is inversely proportional to the superlattice length, but attains a constant value as system dimension becomes larger than the typical phonon mean free path. This nanoscale effect can be incorporated into a continuum model by treating the interface as a distinct material with an effective thermal resistance equal to R_k. Our technique provides steady-state spatial temperature distribution within the superlattice that is in excellent agreement with a corresponding MD simulation of an entire system.

G. Balasubramanian and I. K. Puri, under review

9.1 Thermal transport in solids and across interfaces

The heat conduction mechanism in solids varies across length scales (Chen, 2000a; Sellan et al., 2010). Phonons, which enable energy transfer through lattice vibrations, are the predominant energy carriers in dielectrics and semiconductors. The ballistic propagation of phonons along dimensions smaller than the phonon mean free path causes them to scatter at the system boundaries (Schelling et al., 2002; Sellan et al., 2010). For larger (>50 nm) length scales, internal phonon scattering within the material produces diffusive heat transfer (Incropera, 2007). This scattering, which can depend upon the direction of heat flux (Hu et al., 2009), is enhanced as the phonon wavelength becomes comparable to the length scales of impurities and interfaces (Murad and Puri, 2008a; Stevens et al., 2007).

An interface between dissimilar materials, even without defects on the contact surfaces, creates an impedance to thermal transport that depends upon the differences in the densities and phonon propagation speeds for the two materials. The impedance induces an interfacial thermal (or Kapitza) resistance (Challis, 1974; Murad and Puri, 2009b; Pollack, 1969; Swartz and Pohl, 1989) $R_k = \Delta T/q$, where ΔT denotes the temperature drop across the interface and q the net heat flux flowing across the contact area.

9.1.1 MD simulation of a Si-Ge interface

We examine R_k through nonequilibrium molecular dynamics (MD) simulations (Haile, 1997) for a Silicon (Si) - Germanium (Ge) superlattice that is illustrative of semiconductor applications (Becker et al., 2006; Volz et al., 2000a,b). Figure 9.1 presents a representative temperature distribution along the x-direction of a 20.0 nm (x) × 2.5 nm (y) × 2.5 nm (z) cuboid domain. It includes a 10.0 nm × 2.5 nm × 2.5 nm solid Si lattice extending from 0 - 10 nm along the x-direction, and a 10.0 nm × 2.5 nm × 2.5 nm Ge lattice from 10 - 20 nm.

The MD simulations are conducted using the LAMMPS code (Plimpton, 1995). Each simulation step is 1 femtosecond (fs) long. The Si-Si, Ge-Ge and Si-Ge interactions are described through the Tersoff potential (Tersoff, 1988, 1989) which is based on the concept of bond order, i.e., the bond between atoms i and j is weakened by the presence of other bonds involving atom i. The interaction parameters are listed in the literature (Tersoff, 1988, 1989).

Periodic boundary conditions are employed in the y- and z-directions for the MD simulations while free surface conditions are imposed along the x-direction. The system is initialized at 300 K and equilibrates with a Langevin thermostat with a coupling time of 0.1 picoseconds (ps) for 2 nanoseconds (ns).

A temperature gradient is imposed on the system by heating the Si atoms between 0 - 0.5 nm to 330 K and cooling the Ge atoms between 19.5 - 20.0 nm to 270 K. The temperatures are maintained constant in Si and Ge by rescaling the atomic velocities every timestep (Balasubramanian et al., 2008). The entire system is thereafter allowed to behave freely with constant volume and energy (NVE ensemble) over the next 11 ns. All simulations used a timestep of 0.002 ps.

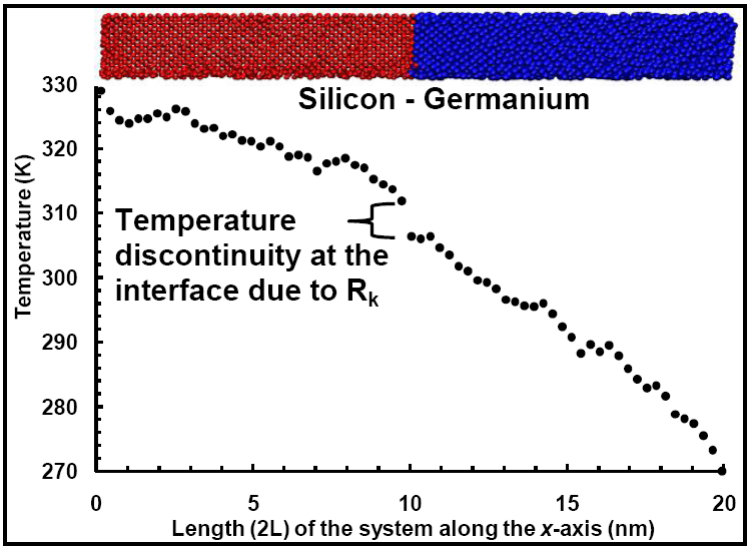

Figure 9.1: Spatial temperature distribution in a Si-Ge superlattice. Thermal transport is induced by hot Si atoms that lie between x = 0 - 0.5 nm (T_{Si} = 330 K) that transfer heat to cooler Ge atoms between x = 19.5 - 20.0 nm (T_{Ge} = 270 K). A temperature discontinuity of $\approx$ 5 K is observed at the interface at x = 10 nm due to the interfacial thermal resistance R_k.

The simulated temperatures are recorded every 20 ps and averaged over the last 1 ns in successive 0.3 nm $\times$ 2.5 nm $\times$ 2.5 nm slabs. The resulting spatial temperature distribution is presented in Figure 9.1. The interfacial thermal resistance at $\approx$ 10 nm produces a temperature discontinuity of $\approx$ 5K across the Si-Ge interface (Samvedi and Tomar, 2009). Higher tem-

peratures enhance lattice vibrations since the local atoms also possess larger kinetic energies ($T = \frac{2}{nNk_B}\sum_{i=1}^{N}\frac{1}{2}mv_i^2$). The vibrations in the Si lattice propagate, transferring energy to cooler regions in the superlattice and also scattering internally. The difference in the phonon propagation speeds across the Si-Ge interface, leads to a mismatch in phonon frequencies. Thus, phonons traveling through Si scatter at the interface, only partially transferring their energy to Ge. This impedance to heat conduction results in the temperature discontinuity at the interface. Overall, the bulk system follows the empirical Fourier's law of continuum heat conduction (Incropera, 2007) in regions further ($\approx$ 3-4 molecular layers) removed from its boundaries.

9.2 Bridging length scales and the transport mechanisms

Using either a solely continuum approach or instead only molecular simulations to describe the overall influence of the thermal resistance across an interface can be problematic. Continuum relations do not adequately describe the interfacial heat transfer at the nanoscale. However, the alternative of conducting molecular simulations for a mesoscale system containing thousands of atoms can be computationally expensive and an inefficient use of resources. We circumvent this difficulty by incorporating the effect of R_k into a modified continuum relation for steady-state heat conduction.

9.2.1 Length dependence of thermal conductivity

Since the heat transfer changes from ballistic transport at length scales smaller than the characteristic phonon mean free path to diffusive transport for larger systems,(Chen 2000) the material thermal conductivity, a required parameter in continuum relations, also changes (Sellan et al., 2010; Yang et al., 2008b). The literature discusses the variation of Si thermal conductivity with length (Sellan et al., 2010; Yang et al., 2008b), but a similar study for Ge is absent.

We use equilibrium MD to simulate Ge cubes of various edge dimensions L to describe the dependence of its thermal conductivity k_{Ge} on length. Periodic boundary conditions in all directions are employed to eliminate phonon-boundary scattering. Tersoff potentials model

the atomic interactions. The value of k_{Ge} is obtained from equilibrium MD simulations using the Green-Kubo method based on the fluctuation-dissipation theorem (Guajardo-Cuellar et al., 2010; Schelling et al., 2002; Sellan et al., 2010). The heat current vector S in such systems oscillates about zero at equilibrium and the thermal conductivity is correlated with the time required for these fluctuations to dissipate. Therefore, for a cubic isotropic material

$$k_{Ge} = \frac{1}{3k_B V T^2} \int_0^\infty \{< \vec{S_{ij}}(t)\vec{S_{ij}}(0) >\} dt \tag{9.1}$$

where k_B denotes the Boltzmann constant, V and T the system volume and absolute temperature, t the time, and $< \vec{S_{ij}}(t)\vec{S_{ij}}(0) >$ is the heat current autocorrelation function (HCAF). We determine k_{Ge} from converged values of the HCAF.

Each cube is initialized at 300 K and 1 atm. Using 0.002 ps timesteps, it is (1) simulated for 0.2 ns under constant temperature and pressure (NPT ensemble) to relax the internal stresses in the lattice, (2) followed by a constant volume and temperature (NVT) simulation for further 0.2 ns. We employ the Nose-Hoover thermostat and barostat, each with a coupling time of 0.1 ps to maintain the temperature and pressure, respectively. Finally, the system is allowed to evolve freely with constant volume and energy (NVE) over the next 2 ns, while the heat current values are sampled over every 0.02 ps and the time correlation between them is calculated. k_{Ge} is calculated by averaging the thermal conductivities k_{xx}, k_{yy} and k_{zz} along the three orthogonal (x-y-z) directions of the cubic lattice recorded every timestep over that last 200 ps. To accurately determine the HCAF integral, simulation times (2 ns) that are much longer than phonon relaxation time of $\approx$ 100 ps are employed (Sellan et al., 2010).

The variation of $1/k_{Ge}$ with $1/L$ is presented in Figure 9.2 for L in the range from 2.5 nm - 10 nm. As the system length increases so does the thermal conductivity with a linear correlation between $1/L$ and $1/k_{Ge}$. At very small length scales, phonons do not have sufficient space for their natural evolution and decay. This enhances the energy loss due to boundary scattering so that transport is predominantly ballistic. As the system size increases, boundary scattering diminishes, leading to lower energy losses and higher thermal conductivity. Here, thermal transport becomes diffusive. Extrapolating the predictions for L approaching ∞, we obtain the bulk thermal conductivity for Ge $k_{Ge-Tersoff} = 111$ $\mathrm{Wm^{-1}K^{-1}}$. While this value agrees with the MD simulation literature (Dong et al., 2001), it differs from experimen-

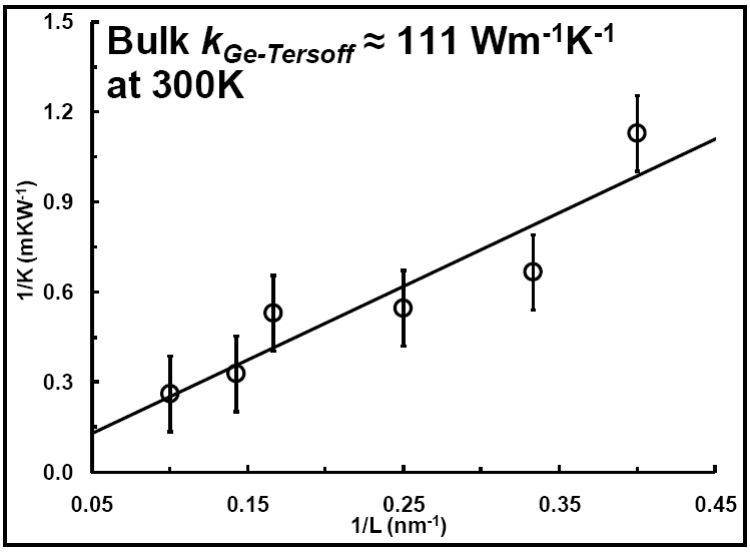

Figure 9.2: Length L dependence of the Ge thermal conductivity k_{Ge} at 300 K obtained from equilibrium MD simulations. The continuous line is a linear fit to the data. It is extrapolated to $1/L = 0$ to determine the bulk Ge thermal conductivity $k_{Ge} = 111$ Wm^{-1}K^{-1}. The error bars depict the data scatter in the form of standard errors for the thermal conductivities that are recorded every 0.002 ps over the last 200 ps of each simulation.

tal measurements because (1) empirical potential models are used to mimic the interatomic interactions, (2) a pure defect-free Ge is simulated in comparison to isotopically impure Ge typically used in experiments and (3) the simulations being classical, do not account for variations in phonon frequencies.

9.3 Coupling the nanoscale effects with the continuum

Thermal transport across the length scales is next coupled into a modified continuum simulation using transport coefficients that depend on the dimensions of the superlattice. The interface is treated as a new material with a very small thermal conductivity and, hence, high resistance. This allows the temperature discontinuity to be reproduced using Fourier's law, as follows.

9.3.1 Treating the interface as a thin layer of low thermal conductivity material

Instead of interpreting the interfacial temperature difference as a jump or a discontinuity, we model the interface as a material ($\approx$ 1.2 nm thick) with a very small thermal conductivity (and correspondingly large resistance). This requires an accurate characterization of the effects of system size on R_k. We now employ nonequilibrium MD to simulate various forms of the Si-Ge superlattice described through Figure 9.1 by altering the length along the x-direction of Si L_{x-Si} between 1 - 100 nm. In all these simulations $L_{x-Si} = L_{x-Ge}$. The net heat flux through the interface is calculated by time averaging the energy supplied to the warmer Si and removed from the cooler Ge atoms to maintain their temperatures at constant values (Samvedi and Tomar, 2009).

Figure 9.3a presents the change in R_k with respect to the system length. The simulated R_k values agree with the literature (Samvedi and Tomar, 2009). With increasing L_{x-Si}, R_k decreases, which follows from our argument about the length dependence of thermal conductivity. The reduction in R_k is relatively large for L_x = 1 - 40 nm, which are lengths smaller than the mean free paths of phonons (Chen, 2000a). For larger dimensions, the resistance approaches a constant value. Likewise, the temperature drop at the interface is larger (>10 K) when $L_{x-Si} < 20$ nm but gradually diminishes to a constant value (3 - 5 K) as the system size increases. Overall, the relation $R_k \propto {L_{x-Si}}^{-\beta}$ holds.

When the boundary temperatures (at x = 0 and x = $2L_x$) are maintained constant in the simulations and the system length is varied, the net heat flux through the system changes, which also influences R_k (Kapitza, 1941; Murad and Puri, 2009a,b). Therefore, we again simulate the same set of samples with varying lengths, but instead of maintaining constant boundary temperatures, we supply and extract the same energy (= 8×10^{-8} W) to the hot and cold boundaries during each timestep. This ensures that heat fluxes through the different systems are identical. Figure 9.3b presents the variation in R_k with L_{x-Si}, which is overall similar to the predictions in Figure 9.3a. Both R_k and ΔT decrease by larger amounts for $L_{x-Si} < 30$ nm but then assume constant values. This again demonstrates the presence of a characteristic interfacial resistance even at bulk scales, which follows the $R_k \propto {L_{x-Si}}^{-\beta}$

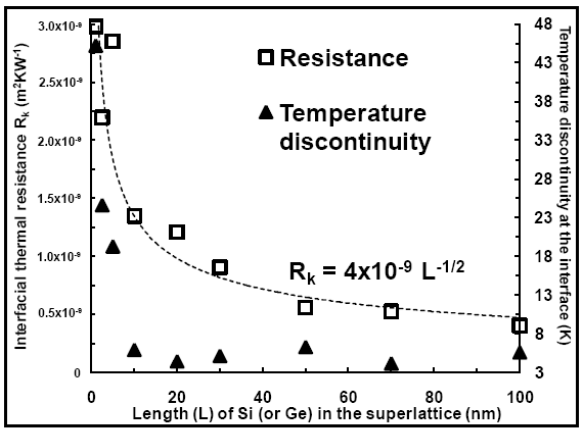

(a)

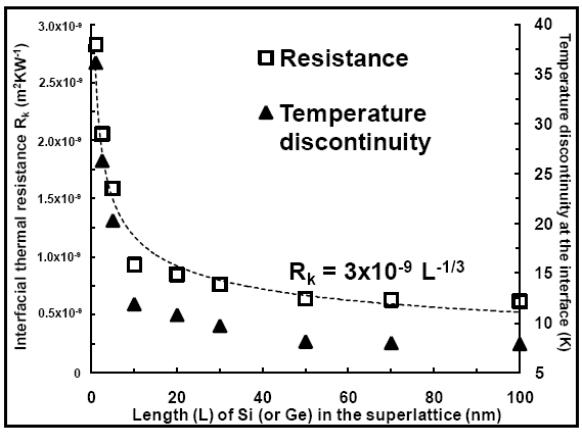

(b)

Figure 9.3: Variation of R_k and interfacial temperature discontinuity ΔT for different lengths of the superlattice obtained from the MD simulations when (a) the temperatures at the boundaries are constant, i.e., $T_{Si} = 330$ K and $T_{Ge} = 270$ K, and (b) a constant energy of 8×10^{-8}W is supplied and simultaneously extracted during every timestep from the superlattice boundaries. The reduction in R_k with increasing L follows a similar relation for both cases. The decrease is relatively large for system dimensions smaller than the mean free path of phonons (Chen, 2000a), but R_k assumes a constant value at larger lengths. The temperature discontinuities follow a similar trend. At length scales larger than the phonon mean free path ΔT has a constant material specific characteristic value.

relationship.

Effects of varying interfacial contact areas are also considered. Superlattices are simulated with L_x = 10 nm (= 2 L_{x-Si} = 2 L_{x-Ge}) while $L_y = L_z$ are varied between 1 - 10 nm. Values for R_k presented in Table 9.1 show that beyond 2.5 nm, the lateral dimensions of the superlattice have negligible influence on the magnitude of R_k. Hence, this resistance is dependent only on the dimensions along the direction of heat conduction, not on those perpendicular to it.

Table 9.1: Interfacial thermal resistance R_k values obtained from MD simulations of 10 nm × y nm × z nm Si-Ge superlattices with different cross-sections are listed. Beyond 2.5 nm lateral dimension, R_k remains constant, implying that dimensions orthogonal to direction of heat transfer do not exert a notable influence on the thermal transport through the interface.

Cross section (y nm × z nm)	1.0 × 1.0	2.5 × 2.5	5.0 × 5.0	7.5 × 7.5	10.0 × 10.0
R_k (m^2KW^{-1})	4.02×10^{-8}	2.85×10^{-9}	2.65×10^{-9}	2.72×10^{-9}	2.75×10^{-9}

A schematic for the proposed technique is in Figure 9.4 where the interface is considered as a new material contained between the Si - Ge superlattice. To demonstrate its applicability, we select the 20 nm (x) × 2.5 nm (y) × 2.5 nm (z) cuboid simulation domain in the configuration of Figure 9.1. Since interfacial effects influence ≈ 2 atomic layers on either side of the contact location (Murad and Puri, 2008a,b), the dimensions of the interfacial material are assumed to be 1.2 nm (x) × 2.5 nm (y) × 2.5 nm (z) that lies between 9.4 - 10.6 nm along the x-direction.

The Fourier law for steady-state heat conduction suggests that the overall heat flux across a system of composite slabs with different thermal conductivities is $q = (T_{HOT} - T_{COLD})/R_{TOTAL}$.(Incropera 2007) Here, the total thermal resistance $R_{TOTAL} = L_{x-Si}/k_{Si} + R_k + L_{x-Ge}/k_{Ge}$ accounts for resistances due to the length-dependent thermal conductivities of Si and Ge as well at the Kapitza resistance of the assumed interfacial material. Again, the

flux $q = (T_{HOT}$ - $T_{i-Si})/(L_{x-Si}/k_{Si}) = (T_{i-Si}$ - $T_{i-Ge})/R_k = (T_{i-Ge}$ - $T_{COLD})/(L_{x-Ge}/k_{Ge})$ leads to a temperature distribution within each material. T_{i-Si} and T_{i-Ge} are the temperatures at the boundaries of the interfacial material in contact with Si and Ge, respectively. Using $T_{HOT} = 330$ K, $T_{COLD} = 270$ K, the length-dependent $k_{Si} = 5.38$ $\mathrm{Wm^{-1}K^{-1}}$ (Yang et al., 2008b), $k_{Ge} = 3.33$ $\mathrm{Wm^{-1}K^{-1}}$ and $R_k = 1.26 \times 10^{-9}$ $\mathrm{Wm^{-1}K^{-1}}$ obtained from the simulations lead to the temperature distribution presented in Figure 9.4. Not only does it successfully reproduce the expected continuum behavior away from the interface, but this also replicates the temperature discontinuity across the interface that is predicted using MD, which is superimposed to validate our technique.

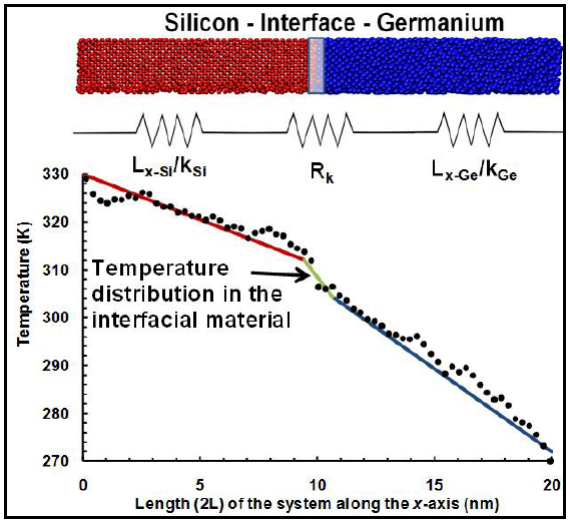

Figure 9.4: Spatial temperature distribution shown through continuous straight lines for a 20 nm (x-wise) long Si-Ge superlattice obtained using a modified continuum approach that considers the interface as a distinct material with a thermal resistance R_k. The thermal transport is induced by hot Si atoms that lie between x = 0 - 0.5 nm ($T_{HOT} = 330$ K) that transfer heat to cooler Ge atoms between x = 19.5 - 20.0 nm ($T_{COLD} = 270$ K). The resistances provided by the Si lattice (L_{x-Si}/k_{Si}), interface (R_k) and Ge (L_{x-Ge}/k_{Ge}) that contribute to the overall heat transfer are shown. The filled circles represent the MD simulation results from Figure 9.1 for comparison.

9.3.2 Conclusions

Thermal transport changes from a ballistic form into diffusive behavior as the length increases from the nano- to the mesoscale. An accurate representation of heat transfer across solid-solid interfaces should account for the corresponding changes in both the bulk and the interfacial thermal resistance with varying length. We provide a modified continuum approach that incorporates the interfacial temperature discontinuity from atomistic simulations of dissimilar solids. The technique treats the interface as a new material with a resistance R_k that depends on the overall system length. As the system sizes increases, lattice vibrations that carry thermal energy scatter inside the bulk material and energy losses at the interface are reduced. This increases the material thermal conductivities simultaneously decreasing the interfacial thermal resistance according to $R_k \propto L^{-\beta}$. The contact area does not exert an appreciable influence on thermal transport. The Fourier heat conduction relation is modified to account for R_k. For our Si-Ge model system, the approach is able to accurately replicate the effects of R_k and predict the temperature discontinuity predicted by MD simulations alone.

9.4 Computational aspects of a second method

The computational expense of a large-scale molecular simulation is circumvented through heterogeneous multiscale modeling. Here a separate molecular simulation of a smaller nanoscale subsystem that accounts for interfacial and boundary effects can be coupled with one of the much larger overall system that is based on continuum relations alone. Many such methods have been suggested although there are few examples that explicitly deal with thermal transport (Chantrenne, 2008; Jolley and Gill, 2009; Kalweit and Drikakis, 2008; Liu et al., 2007; Nie et al., 2004a; Tao and He, 2009; Thome, 2006; Wagner et al., 2001).

The general paradigm is to divide the entire system into two sub-domains. Atomistic simulations are employed for one of these and the other is simulated through a conventional continuum procedure. An overlapping zone between the two sub-domains bridges these two simulations and couples their properties. For example, intermolecular interactions within such a large and complex system can be characterized by coupling MD simulations of small

nanoscale volumes that only encompass interfacial boundary regions with a larger continuum simulation. Thus, the information from the MD simulation can be passed to a more conventional method, e.g., a finite element model (FEM), a finite volume model (FVM), or a meshless method such as symmetric smoothed particle hydrodynamics (SSPH) (Batra and Spinello, 2008; Batra and Zhang, 2008; Gingold and Monaghan, 1977; Lucy, 1977; Zhang and Batra, 2009).

The coupling in the overlap region can be induced either by exchanging state variables (velocity, temperature, pressure) or fluxes (mass, momentum, energy). A properly implemented hybrid scheme will reproduce the behavior of the much larger system with sufficient accuracy by explicitly including the influence of nanoscale interfacial effects. Such a hybrid approach avoids the inordinate computational cost of an MD simulation of the entire system and also diminishes any inaccuracies that are introduced if molecular interactions are not considered (e.g., if the continuum method is employed throughout).

A coupling scheme provides consistency between the state variables calculated from the small and large scale simulations. For instance, physical quantities can be measured separately from both the small scale MD and large scale SSPH simulations, with their boundary values transferred back and forth during the coupling phase. We use a method that averages the local thermodynamic properties in the molecular subdomain and transfers these to an SSPH node, or similarly transfers the continuum level information from an SSPH node to its surrounding MD molecules. We also use the constrained temperature rescaling of atomic velocities.

There are different approaches to specifically ensure mass conservation within a system when molecules flow from an atomistic subsystem to a larger mesoscale subdomain. Typical approaches insert a repulsive wall at the boundaries to prevent the translation of molecules out of the small system domain, or reinsert the same number of molecules into it as those that flow out. However, these techniques introduce imaginary forces that can produce simulation artifacts. We have found that systematically averaging the results reduces their influence and removes unwanted statistical fluctuations (Allen and Tildesley, 1987; Dupuis and Koumoutsakos, 2006; Dupuis et al., 2007; Hadjiconstantinou, 1999; Kalweit and Drikakis, 2006, 2008; Nie et al., 2004a; Oconnell and Thompson, 1995; Tao and He, 2009; Wagner et al., 2001;

Werder et al., 2005).

Matching the physical and computational times appropriately is also important. An MD simulation that takes 500 discrete δt time steps to reach equilibrium should be matched with an SSPH simulation that runs with steps of $500\delta t$. While it might computationally appear that the two simulations run sequentially, since the run time for a coupled simulation set is $1000\delta t$, the total physical time for such a simulation is only $500\delta t$, since two separate problems are being coupled over that period.

9.4.1 Coupling scheme

There are two significant issues while coupling the molecular and continuum simulations in the overlap zone, (1) regarding the exchange of averaged values of the state variables, and (2) ensuring conservation laws are satisfied. The proper exchange of property values in the overlap region (where both MD and SSPH simulations occur) (Kalweit and Drikakis, 2006, 2008) is enabled either through an exchange of the local thermodynamic states or of the corresponding fluxes (Dupuis and Koumoutsakos, 2006; Oconnell and Thompson, 1995; Wagner et al., 2001). The former requires that external boundary conditions be imposed to maintain a constant mass in the overlap zone. Matching the fluxes can become problematic when the physical or computational timescales of the meso- and nanoscale techniques are different (Werder et al., 2005; Wijesinghe and Hadjiconstantinou, 2004), since using flux exchanges at the boundaries of MD and SSPH simulations restricts the time scale to the order of nanoseconds at most. For that reason, we exchange the thermodynamic state variables back and forth between the atoms (during MD) and the nodes (for SSPH).

MD simulations commonly use periodic boundary conditions whereby an atom that leaves any boundary of the nanoscale domain is capable of reentering it through the opposite side. Thus mass conservation in a realistic multiscale model that has fixed nonperiodic boundaries can be challenging. Workarounds to avoid this issue include embedding the molecular system (with periodic boundary conditions) inside a larger periodic system (Hadjiconstantinou and Patera, 1996, 1997), employing a rule to insert or remove atoms or molecules in order to keep their numbers constant in the molecular simulation (Liu et al., 2007, 2008; Nie et al., 2004a,b), or creating an artificial boundary force based on the mean pressure (Dupuis et al.,

2007).

Our experience has shown that MD simulations of nanoscale interfacial regions typically reach an equilibrium state within 1-2 ns after which the boundary temperature gradients and averaged properties in the overlap region can be accurately determined. Since each SSPH node in the overlap region has a zone of influence, the locations of molecules specified by the MD simulations that fall within or on the boundary of such a zone can be assumed to imitate the influences of neighboring SSPH nodes. Using the kernel function and the standard SSPH technique, property values for all nodes (that are specific to the SSPH domain and not the MD molecules) in the overlap region are calculated. These act as the SSPH boundary nodes for the domain of the bulk or larger subsystem and their values provide the corresponding boundary conditions. Next, the mesoscopic simulation is performed for the SSPH subsystem. This simulation typically runs for the same total time as the preceding MD simulations, but with a mesoscale time step that is generally two orders of magnitude or more larger than the MD time step.

The property values are thereafter calculated for all SSPH nodes, including those that are in the overlap zone. Since the overall system is continuous and is spatially decomposed into subsystems only for computational convenience, the temperatures and the gradients at all locations, except near the interfaces that do not lie in the overlap region, are also continuous. We compare the MD and SSPH temperatures and the corresponding gradients in the overlap zone to determine if an acceptable solution has been obtained. If the solution is not acceptable, the hybrid simulation is repeated. The property values of the SSPH nodes in the overlap zone provide the new boundary conditions for the subsequent set of MD simulations. The entire process is repeated with values for the state variables exchanged back and forth until the hybrid simulation converges to within an acceptable tolerance.

9.4.2 Method validation

A complete molecular dynamics simulation is computationally beyond reach for a large mesoscale system. However, since important interfacial effects occur over only three or so molecular layers (Balasubramanian et al., 2008; Banerjee et al., 2007; Murad and Puri, 2007a,b, 2008a,b) we examine smaller systems that have dimensions of tens of nanometers

using both MD and the proposed hybrid multiscale methodology. While not of mesoscale dimensions, it will nonetheless be instructive to learn how the results of the multiscale approach take interfacial effects into account in comparison with the more extensive molecular simulations.

9.5 Details of a computational example

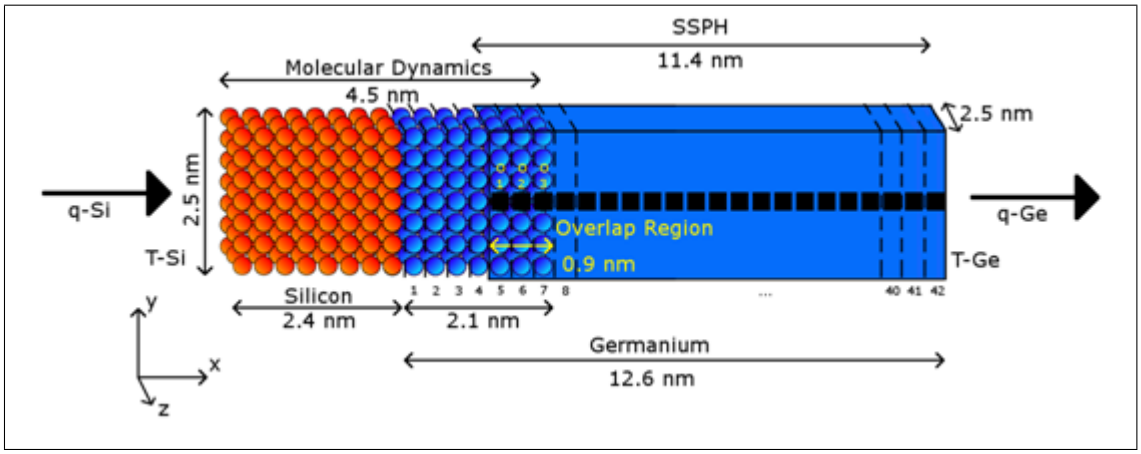

Figure 9.5: The multiscale simulation domain (not to scale) with separate subdomains for continuum simulations using symmetric smoothed particle hydrodynamics (SSPH) and molecular dynamics (MD). The overlap regions where exchanges of state variables occur between the two simulations types are highlighted. Heat flux q flows from the high temperature (T_{Si}) solid Si wall towards the cooler Ge surface at temperature T_{Ge}.

Figure 9.5 presents a two-dimensional cross section of the 15 nm (x) $\times$ 2.5 nm (y) $\times$ 2.5 nm (z) cuboid simulation domain. It contains a 2.4 nm $\times$ 2.5 nm $\times$ 2.5 nm solid Si lattice extending from 0 - 2.4 nm along the x-wise direction, and a 12.6 nm $\times$ 2.5 nm $\times$ 2.5 nm Ge lattice from 2.4 - 15 nm. The interfacial thermal resistance around 2.4 nm is expected to produce a temperature discontinuity across the Si-Ge interface. We intend to reproduce this effect by coupling MD simulations of the entire Si lattice and a small interfacial Ge subdomain (of 2.1 nm $\times$ 2.5 nm $\times$ 2.5 nm size) with SSPH simulations for the bulk of the Ge lattice (11.4 nm $\times$ 2.5 nm $\times$ 2.5 nm), as shown schematically in Figure 9.5. The 0.9 nm

$\times$ 2.5 nm $\times$ 2.5 nm overlap zone provides a region where thermodynamic state variables are exchanged between the MD and SSPH simulations, and convergence tests imposed. Different hot and cold boundary temperatures T_{Si} and T_{Ge} and influx q_{Si} and outflux q_{Ge} conditions are applied at the outermost x = 0 nm (Si) and x = 15 nm (Ge) boundaries to induce thermal transport. A "pure" MD simulation for entire Si-Ge domain is also performed for each case to compare with the coupled multiscale MD-SSPH predictions. Both sets of simulations use a 16-processor cluster. Whereas there are 4460 atoms in the entire domain for the pure MD simulations, only 1422 atoms are required for the MD portion of the hybrid computation.

Periodic boundary conditions are employed in the y- and z-directions for the MD simulations, while nonperiodic boundaries exist along the x-wise direction. The MD simulations are conducted using the LAMMPS code (Plimpton, 1995), with each simulation step being 1 femtosecond (fs) long. The Si-Si, Ge-Ge and Si-Ge interactions are described through the Tersoff potential. The system is initialized at 300 K and equilibrates with a velocity-rescaling thermostat that is removed after 500 picoseconds (ps). The entire system is thereafter allowed to behave freely with constant volume and energy over the next 50 ps. Then, various conditions are imposed for different simulation cases by either (1) increasing the temperature to T_{Si} and maintaining it by rescaling the atomic velocities, or (2) by introducing a constant heat flux q_{Si} for the entirety of the simulations through the atoms that lie between 0-0.3 nm in the x-wise direction. After the MD simulations have proceeded for 500 ps, the temperatures along the x-wise direction are averaged over the next 200 ps in successive 0.3 nm $\times$ 2.5 nm $\times$ 2.5 nm slabs. The spatial temperature distribution is smoothened by sampling fifteen MD simulation sets, each of which is initialized with the same macroscopic thermodynamic conditions, but with an ensemble of different microscopic states.

The continuum simulations are based on Lagrangian mesh-free SSPH that predicts the local states at any specified location through an interpolation of the particle distribution in its neighborhood. Thus, the material properties at a particular position, or node, are obtained through an interpolation of the particle distribution in the neighborhood of that node. This is accomplished by introducing a smoothing or weighting kernel function which ensures that particles closest to the node exert a stronger influence on it than those that are further away. The heat conduction equation in the bulk Ge lattice has the form

$$\int_{\Omega}\{\rho c w\frac{\partial T}{\partial t}\}d\Omega = \int_{\Omega}\{k\frac{\partial}{\partial x}(w\frac{\partial T}{\partial t})\}d\Omega - \int_{\Omega}\{k\frac{\partial w}{\partial x}\frac{\partial T}{\partial x}\}d\Omega - \beta\int_{\Gamma}\{w(T-T_b)\}d\Gamma \qquad (9.2)$$

where ρ denotes the density, c the specific heat capacity, k the thermal conductivity, T_b the boundary temperature, w the kernel function, and β a penalty parameter (Batra and Zhang, 2008; Zhang and Batra, 2009). Thirty eight equispaced nodes are distributed in the Ge lattice at 0.3 nm intervals along the x-axis to ensure that the averaging slabs for the MD and sampling around the SSPH nodes occur over similar regions. A T_{Ge} or q_{Ge} boundary condition is imposed at x = 15 nm. The second boundary condition is the temperature of node O_1 that is obtained through the coupled MD simulation for slab 5 lying between 3.6-3.9 nm in the overlap region. The system is initialized at 300 K and simulated over the next 700 ps with 0.001 ps time steps.

The entire Si lattice and the first seven slabs containing the Ge material in the vicinity of the Si-Ge interface are simulated using MD. The bulk of the Ge lattice encompassing slabs 5-42 is described using SSPH. Thus, slabs 5-7 form the overlap region where both MD and SSPH simulations are employed. The information exchange must be refined since the two methods have different length scales. These local states are harmonized by assigning the average temperature for slab 5 obtained from the MD simulations to SSPH node O_1, as shown in Figure 9.5. If the differences between the temperatures of slab 7 and node O_3, obtained respectively from the MD and SSPH portions of the hybrid simulations, are larger than 2%, the MD simulations are repeated for another 700 ps. In this case the (MD) temperature of slab 7 is made identical to that of SSPH node O_3 by rescaling the atomic velocities. However, since this thermostat changes the local molecular energies in the slab that could have been otherwise transferred to neighboring atomic layers, it can induce fictitious temperatures. The intermediate slab 6 corresponding to node O_2 acts as a buffer region to ensure that these artifacts decay when they are transferred to the MD portion of the hybrid simulation (LIU, CHEN et al. 2007). Computational convergence for the Ge temperatures in the overlap zone is obtained after a single SSPH simulation for all four cases considered. However, systems with steeper temperature gradients could require repeated sets of coupled simulations to obtain converged results.

9.5.1 Results from the hybrid simulations

The computational times required to obtain equilibrium solutions using pure MD and the hybrid MD-SSPH simulations are presented in Table 9.2 along with the temperature and flux boundary conditions for four cases. The hybrid MD-SSPH method typically provides $\approx$ 60% savings in computational time over a pure MD simulation. The time required for an MD-SSPH simulation essentially scales with the number of atoms N, which is roughly 70% smaller for the hybrid method than for pure MD. This is to be expected, since the time for the parallel implementation of classical MD simulations on P processors scales at best as $\bigcirc$(N/P), while the interprocessor communication time scales as $\bigcirc$(N) (Plimpton, 1995). Thus, the hybrid scheme should be significantly less expensive for even larger systems.

Table 9.2: List of boundary values and simulation times for various cases corresponding to both the pure MD and the hybrid MD-SSPH simulations. Percentage gain in the computational time is obtained as difference in the times for the two sets of computations over the time required for pure MD simulation. All simulations use the same set of 16 processors of the ESM-LCC cluster.

Case	Boundary condition		Time (HH:MM)		Computational gain (%)
	Si	Ge	MD	MD-SSPH	
I	$T = 350K$	$T = 300K$	23 : 50	9 : 32	60
II	$q = 1.28 \times 10^{10}$ W	$q = -1.28 \times 10^{10}$ W	24 : 20	9 : 54	59
III	$T = 350K$	$q = -1.28 \times 10^{10}$ W	24 : 02	12 : 31	48
IV	$q = 1.28 \times 10^{10}$ W	$T = 300K$	35 : 34	13 : 08	63

Figure 9.6 presents the equilibrium spatial temperature distributions obtained from the hybrid and pure MD simulations for the four cases. For case 1 shown in Figure 9.6a, the boundary temperatures $T_{Si} = 350$ K and $T_{Ge} = 300$ K are maintained. The ≈ 8 K temperature discontinuity at the interface due to the acoustic mismatch between the Si and Ge lattices is reproduced by the hybrid simulation. The temperature distribution in the bulk Ge is linear

and in accord with the continuum Fourier relation. Minor temperature differences between the pure MD and hybrid simulations are attributed to statistical fluctuations associated with MD.

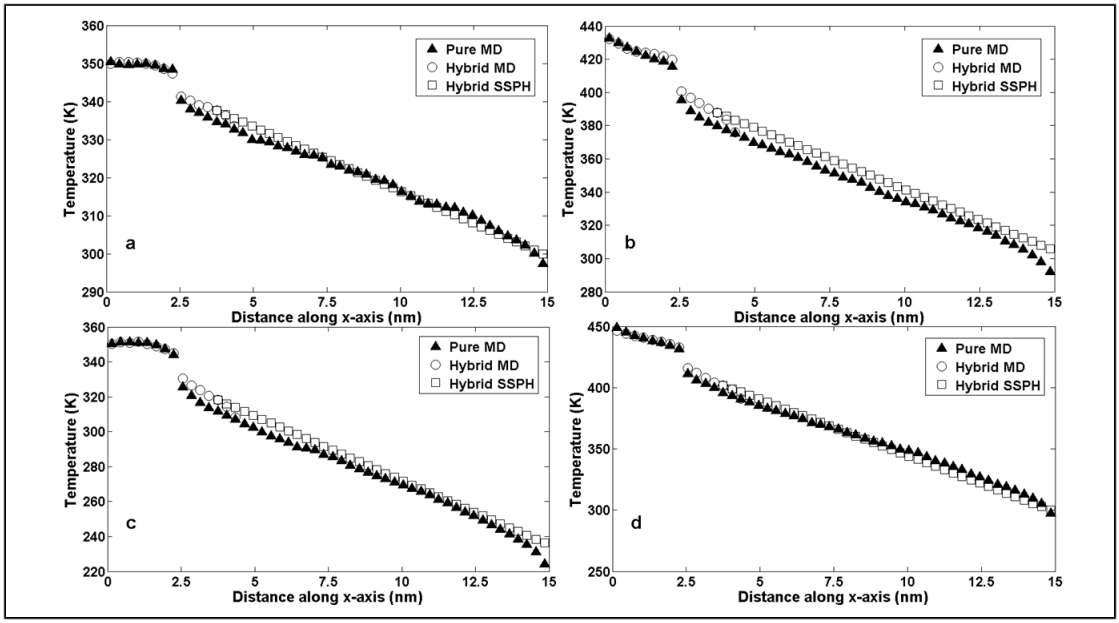

Figure 9.6: Spatial temperature profiles at equilibrium for the various simulated cases using both hybrid MD-SSPH scheme and pure MD simulations. The imposed boundary values for simulated cases corresponding to the figures are (a) T_{Si} = 350 K, T_{Ge} = 300 K, (b) q_{Si} = 1.28 × 10^{10} Wm^{-2}, q_{Ge} = -1.28 × 10^{10} Wm^{-2}, (c) T_{Si} = 350 K, q_{Ge} = -1.28 × 10^{10} Wm^{-2} and (d) q_{Si} = 1.28 × 10^{10} Wm^{-2}, T_{Ge} = 300 K.

For case 2, q_{Si} = 1.28 × 10^{10} Wm^{-2} with a similar outflux q_{Ge}. Figure 9.6b shows that the temperature decreases from 430 K at x = 0 towards the interface where there is a significant temperature discontinuity of ≈ 20 K due to interfacial phonon scattering. This is again followed by a linear temperature distribution in the bulk Ge lattice. Since nonperiodic boundaries assume vacuum adjacent to them, they induce phonon scattering. This case lacks an explicit temperature boundary condition and, unlike MD, the SSPH predictions are unable to reproduce phonon scattering at x = 15 nm. Thus, SSPH predicts higher temperatures in the Ge lattice than does pure MD. For instance, at x = 15 nm, the hybrid simulation

predicts a 305 K temperature while the pure MD prediction is 292 K. Even though it leads to computational savings, and the MD and SSPH temperatures converge in the overlap zone, the hybrid technique is unable to reproduce boundary effects when fluxes are added or removed.

The temperature distribution for case 3, shown in Figure 9.6c, corresponds to $T_{Si} = 350$ K and an outflux $q_{Ge} = 1.28 \times 10^{10}$ Wm^{-2}. There is good agreement between the hybrid MD-SSPH and pure MD predictions except at the Ge boundary due to the limitations of SSPH in modeling phonon scattering. Since the hybrid and pure MD simulations both involve MD at the Si-Ge interface, they predict an identical ≈ 15 K temperature discontinuity. Case 4 corresponds to $q_{Si} = 1.28 \times 10^{10}$ Wm^{-2} and $T_{Ge} = 300$ K. Since the Ge boundary temperature is now maintained constant for both simulations, this condition implicitly compensates for boundary scattering. Hence, both the pure and hybrid simulations yield similar results, as shown in Figure 9.6d. They also predict identical ≈ 17 K temperature discontinuities at the Si-Ge interface.

9.5.2 Conclusions

We implement a hybrid nonequilibrium molecular dynamics (MD) and symmetric smoothed particle hydrodynamics (SSPH) simulation for a model Si-Ge mesoscale system and it provides significant computational time savings over the corresponding pure MD simulation. The molecular and continuum models are coupled in the hybrid scheme by transferring state information between the two simulations in an overlap region. The hybrid simulation incorporates the influence of a Si-Ge interfacial thermal resistance and predicts $\approx$ 8-20 K temperature discontinuities for the cases considered. Heat transfer in the bulk Ge lattice, which extends approximately four atomic layers beyond the Si-Ge interface, follows the Fourier heat conduction relation. There is good agreement between the two simulations when the boundary temperatures are specified. The imposition of heat flux boundary conditions leads to discrepancies between the two sets of predictions since SSPH is unable to account for the energy loss due to phonon boundary scattering. In this case, SSPH predicts higher temperatures than pure MD, which reproduces this scattering at the nonperiodic boundaries.

Chapter 10

Nanotechnology education for freshmen: First step of a spiral pedagogical model

A nanotechnology learning module was implemented into a freshman engineering course at Virginia Tech. The novelty of our approach is that an established spiral curriculum model has been employed, for the first time to the best of authors' knowledge, to design the nanotechnology option. The module was piloted in a freshman class (180 students) during spring '08. The key components included (1) a prior knowledge survey, (2) a 40-minute in-class presentation on basic nanotechnology concepts, (3) an activity that involves nanoscale image analysis and the plotting of molecular forces using LabVIEW software, and (4) a post-module survey. Lessons learned from the pilot implementation were incorporated appropriately to expose roughly 1450 freshmen to nanotechnology basics in fall '08. The module was further refined in spring '09 when pre- and post-tests were administered to assess the learning outcomes. Based on the prior knowledge data from about 1800 freshmen, we found that they had misconceptions about nanoscience fundamentals, e.g., regarding the (1) role of gravity at the nanoscale,

G. Balasubramanian, V. K. Lohani, I. K. Puri, S. W. Case and R. L. Mahajan, International Journal of Engineering Education 27 (2), 333-353 (2011)

Reprinted with permission from International Journal of Engineering Education

and (2) behavior of intermolecular forces. Exit surveys revealed that approximately 18% of students had an interest in pursuing a nanotechnology option and approximately 65% believed that nanotechnology was relevant in their intended engineering majors. LabVIEW provided an appropriate environment to implement the hands-on analysis of nanotechnology concepts, but we caution that such hands-on exercises should place greater emphasis on nanotechnology concepts than on LabVIEW skills.

10.1 Educational initiatives

Virginia Tech offers one of the largest engineering programs in the United States. A Department of Engineering Education (EngE; www.enge.vt.edu) was created within its College of Engineering (CoE) in early 2004 to improve engineering pedagogy and initiate engineering education research activities. EngE offers a common one-year General Engineering (GE) program for the initial preparation of approximately 1500 incoming engineering freshmen. Students transfer into thirteen ABET-accredited engineering majors after successfully completing the GE program. The EngE Faculty collaborates with other engineering departments and the School of Education to pursue engineering education research and curriculum development activities. A National Science Foundation (NSF) grant funded through its department level reform (DLR) program has been instrumental in introducing a spiral curriculum approach (briefly described in the following section), to reformulate the engineering curricula of bioprocess engineering and freshman engineering programs in the CoE (Lohani et al., 2005b). Experiences in our DLR project were extended in 2008 to develop a nanotechnology option within the CoE Department of Engineering Science and Mechanics (ESM; www.esm.vt.edu) using this spiral curriculum approach. The effort is coordinated by nanotechnology and engineering education experts and is funded through the NSF Nanotechnology in Undergraduate Education (NUE) in engineering program. The project makes use of the Nanoscale Characterization and Fabrication Laboratory (NCFL; www.ncfl.ictas.vt.edu) of the Institute for Critical Technology and Applied Science (ICTAS; www.ictas.vt.edu) at Virginia Tech.

We illustrate the implementation of a nanotechnology module for engineering freshmen in the context of a spiral curriculum and assess the scope of teaching fundamentals of nanotechnology to a heterogeneous population of students in the freshman engineering class of Virginia Tech. We discuss the learning modules that are being implemented to establish the spiral theory based nanotechnology option. Specifically, we provide implementation details of a freshman module that initiates the spiral framework. This module was successfully implemented in a freshman engineering course in successive stages to roughly 180 students in the 2008 spring semester, 1450 students in the fall semester that year, and 180 students in the 2009 spring semester. An analysis of the assessment data to discuss the effectiveness

of the module is also presented. We also discuss our plans for implementing the remaining components of the nanotechnology spiral.

10.1.1 Department-Level Reform (DLR) project (2004-2009)

This project is the first major curriculum reform and engineering education research project at Virginia Tech's College of Engineering and is funded by the U.S. National Science Foundation. The twentieth century psychologist, Jerome Bruner, proposed the concept of the spiral curriculum in his classic work The Process of Education (Bruner, 1960) and The Culture of Education (Bruner, 1996). Bruner advocates that a curriculum as it develops should revisit basic ideas repeatedly, building upon them until the student has grasped the full formal apparatus that goes with them. This approach was adopted in a 5-year (2004-2009) grant under a Department-Level Reform (DLR) program of the NSF (hereafter referred to as DLR project). In this project, a number of EngE faculty members collaborated with faculty from the Biological Systems Engineering (BSE) and the School of Education to reformulate the freshman engineering (also called general engineering) program within the EngE and the bioprocess program within the department using a theme-based spiral curriculum approach (Bruner, 1960, 1996). Two major outcomes of this project were: (i) spiral curriculum reformulation of bioprocess engineering within BSE department, and (ii) enhanced freshman engineering program. The spiral reform process in bioprocess engineering included a 7-step process (Wolfe et al., 2009). The DLR project investigators have conducted workshops within and outside United States to share the details of spiral curriculum development process (Lohani et al., 2005a). Also, a number of hands-on activities have been implemented in this course to make it learner-friendly, contemporary and research-driven (Lo et al., 2006; Lohani et al., 2005a). Some examples include the use of a clicker-based classroom response system to obtain student feedback, introduction to sustainability (Mullin et al., 2006a, 2007), ethics skits that enable engineering ethics learning (Mullin et al., 2006b), introduction of international research and education activities (Jayaraman et al., 2008; Lohani et al., 2006a), use of the electronic portfolio (e-portfolio) for instruction (Knott et al., 2004, 2005), and multi-disciplinary design based on mechatronics (Lohani et al., 2006b). Tablet PC based instruction was introduced in this course in 2006 (Lohani et al., 2007, 2008b). A number of

formative and summative assessment activities have been implemented in EngE 1024 as part of the DLR project to evaluate the learning experiences of freshmen (Robson et al., 2006, 2008, 2007). Additional details are available in references (Lohani, 2010).

10.1.2 Literature review

Bruner's spiral curriculum theory has been adopted to reformulate diverse academic curricula. For example, Wark and Kohen (Wark and Kohen, 2002) describe a spiral curriculum approach to redesign a hypnosis training program at University of Minnesota. Elizondo et al. (Elizondo et al., 2002) discuss the use of the approach in the horizontal and longitudinal integration of basic and clinical sciences to enable medical school curricular reform in Mexico. A core curriculum for medical education in the U.K. presented by Harden and Davis (Harden and Davis 1995) uses the spiral approach as one of its underlying philosophies. Cowan et al. (Cowan et al., 1998) advocate the use of the programming language Zeno in a spiral curriculum to facilitate problem-solving instruction in schools in Britain. The results of successful project-based spiral chemical engineering curriculum design, implementation, and evaluation at Worcester Polytechnic Institute are presented in a series of papers by Clark et al. (Clark et al., 2000), Dixon et al. (Dixon et al., 2000), and DiBiasio et al. (DiBiasio et al., 2001). The authors claim that spiral-taught students displayed equal or better understanding of basic chemical engineering principles, performed better in upper level courses, and had higher satisfaction levels with their academic experience as compared to students who were taught traditionally through a compartmentalized sequence of courses. Gupta et al. (Gupta et al., 2008) discussed an approach for transforming the educational experiences of transfer students in chemical engineering by developing and implementing a multidimensional spiral curriculum. Lohani (Lohani, 2010) has discussed the application of the spiral approach to reformulate the bioprocess engineering program in Virginia Tech.

A general approach to a bottoms-up curriculum that retains the interdisciplinary nature of nanotechnology is to bring together faculty members from various departments who are able to incorporate the essential aspects of their different disciplines (Lee et al., 2006). Bickle et al. (Bickle et al., 2006) describe the implementation of a nanotechnology curriculum at University of Cincinnati through which second and third year students were exposed to the

fundamental scientific concepts at the nanoscale, the related ethical issues, and hands-on laboratory experiences in nanoscale characterization and nanoparticle synthesis. Universities in Taiwan have provided opportunities to students from different majors in different years of their undergraduate education to learn through a common nanotechnology curriculum (Chu and Song, 2006). Another approach is to design the curriculum around applications (Raju and Muthuswamy, 2005). Specifically designed courses have been developed to teach sophomores the fundamentals of nanotechnology and its potential to develop micro-arrays, micro-fluidics and nanostructures (Mendelson et al., 2004). Florida Tech implemented a freshmen fundamentals of nanotechnology course by teaching them about ferrofluid synthesis, quantum dots, and carbon nanotubes followed by hands-on experience on laboratory equipment, such as a Scanning Tunneling Microscope (STM) and an Atomic Force Microscope (AFM) (Winkelmann et al., 2005). Similar laboratory based approaches with an emphasis on synthesis and characterization have been implemented elsewhere for engineering and science students (Jaksic, 2008; Mitin et al., 2008). Learning modules have been developed to integrate nanotechnology research into the undergraduate curriculum that help students understand the impact of sustainable engineering solutions in a global context (Hu, 2008). Other examples include online nanotechnology programs (Anwar and Dhillon, 2008), that rely on web-based distance learning, e.g., through the use of the LabVIEW software environment to understand a nanoscale experiment on a piezoelectric actuator (Chang et al., 2002). Engaging freshman students to learn about nanotechnology has exposed them early on to a nanotechnology option (Shapter et al., 2002, 2004). Another approach has been to develop a nanotechnology concentration or major that does not require freshmen student exposure to nanotechnology (Hegab et al., 2005). The University of Wisconsin-Stout has developed a concentration available to Applied Science and Engineering Technology majors (Schultz, 2007). Nanotechnology is also taught from a humanities perspective through a discussion-based module that teaches students to understand the societal implications of the technology (Tahan et al., 2006). The possibility and utility of "sociotechnical integration" during nanoscale engineering research in an academic setting is reported in (Fisher and Mahajan, 2006).

We have chosen to expose all engineering freshmen at Virginia Tech to some fundamental nanotechnology concepts through our spiral methodology to address student misconceptions,

e.g., about the predominant intermolecular forces (Augustine et al., 2006). Students interested in pursuing a nanotechnology option are then provided with hands-on learning and advanced coursework in the experimental and computational aspects of nanotechnology, as well as relevant undergraduate research experiences.

10.1.3 Spiral curriculum approach

The concept of the spiral curriculum proposed in The Process of Education (Bruner, 1960) and The Culture of Education (Bruner, 1996), Bruner's idea was that learners - even beginners - could engage successfully with the central problems and questions inherent in any discipline if those key questions could be represented in a manner that invites real experimentation and inquiry at the appropriate level. One key to this idea is that the learning curriculum could be arranged so that the central questions, or themes in a discipline, would be returned to again and again as learners advance in their knowledge and intellectual capacity. The learning trajectory is thus represented as a spiral rather than the linear pathway that is characteristic of traditional schooling. As learners participate in increasingly complex investigations, organized carefully around the major themes of choice, they acquire in a more natural way the knowledge they need because it is connected to problems of real import and interest, and they acquire also the full intellectual apparatus associated with being the scientist, historian, or engineer rather than learning about their chosen discipline. This approach was adopted to reformulate the bioprocess engineering curriculum within the Biological Systems Engineering (BSE) Department at Virginia Tech. Three spiraling themes, namely, design, systems, and ethics are considered in the spiral reformulation (Lohani et al., 2009c; Wolfe et al., 2009).

We extended our experiences of implementing spiral theory based curriculum reformulation for structuring the nanotechnology option discussed here. Nanotechnology is the scientific understanding of physical processes at the smallest scale of length and time that engineers can integrate into their systems. While both top-down and bottoms-up approach exist, the latter begins from the fundamentals of atoms and molecules, gradually inserting the complexities of nanostructures and nanoscale interfaces, and then moving on to understand how they contribute to microscale and macroscale systems. Considering the interdisciplinary nature of

nanoscale science and engineering, and noting that new phenomena arise at the nanoscale, we believe that the spiral approach is the most effective way to impart and reinforce the basic concepts of nanotechnology. Implementation of nanotechnology education using an established learning theory model like the spiral approach has not been attempted to the best of our knowledge. While the bottoms-up approach described by Lee et. al (Lee et al., 2006) considers the expertise of researchers from different disciplines, it does not provide a model for the actual curriculum. Other approaches are traditional lecture-workshop-demonstration schemes which follow the regular course structures, and not any theoretical model. The various learning experiences the students will undergo in pursuing our spiral theory based nanotechnology option are discussed in the next section.

10.1.4 Spiral experiences at different learning levels of the nanotechnology option

The implementation of the nanotechnology option includes learning modules designed to impart knowledge at four learning levels (i.e., Level 1 through Level 4). These modules are not necessarily courses that students must take during the freshman, sophomore, junior and senior years of their undergraduate engineering curriculum. Rather, the learning levels essentially imply the different stages of knowledge that students will gain through the spiral curriculum, with the content and complicacy of the learning experience gradually increasing from Level 1 through Level 4. Figure 10.1 shows the key learning objectives at the various learning levels of the nanotechnology option. For example, the knowledge students acquire about the role of intermolecular forces during the freshman nanotechnology module (Level 1) recurs when they learn about the computational techniques in molecular mechanics (Level 3). Likewise, the brief description of common experimental instruments used for nanoscale characterization provided during Level 1 is repeated in depth in Level 2, with hands-on experiences with the fabrication and experimental procedures. These learning experiences are revisited during the undergraduate research experience at Level 4 where, not only are the computational and experimental skills of the students acquired from the previous levels put to test, but the potential applications and ethical issues highlighted during the freshman nanotechnology module are also explored with greater emphasis. Details of the various learning objectives at

the different levels of the nanotechnology option are listed in Table 10.1.

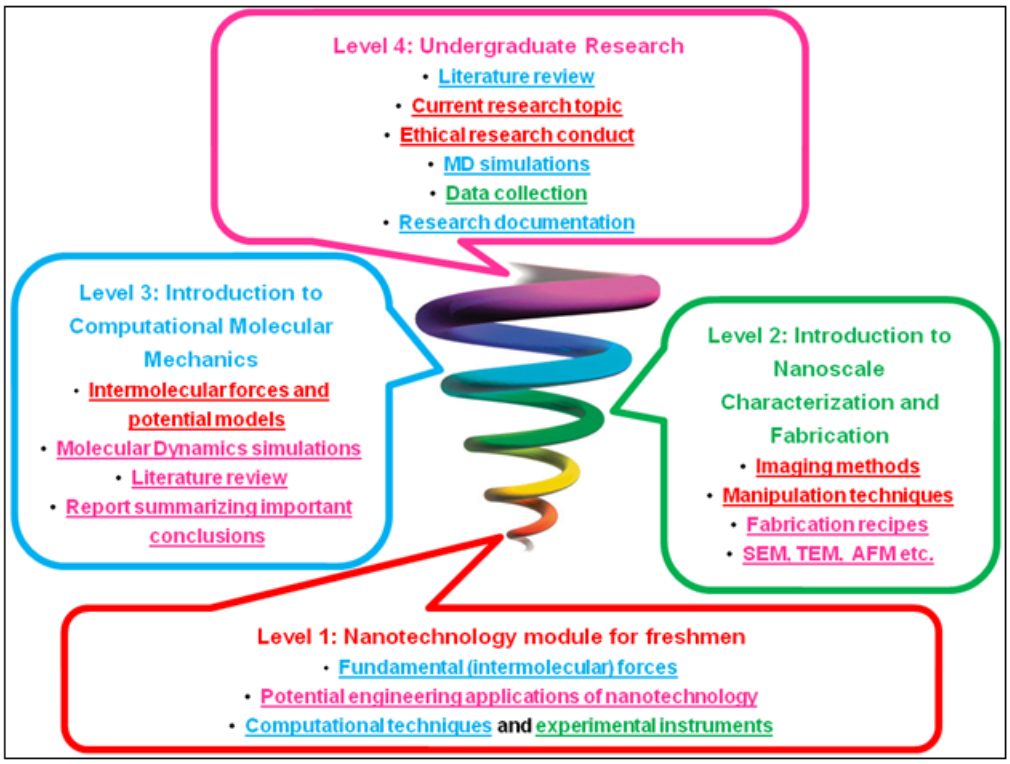

Figure 10.1: Nanotechnology option developed using the spiral curriculum approach.

The key learning activities at various learning levels in the nanotechnology option are presented in Figure 10.2. As an example, the Level 1 hands-on exercises involving the determination of diameter of carbon nanotubes and plotting the nature of intermolecular forces provide students with fundamental notions about nanostructures, which recur at the higher learning levels. Students watch videos of nanotechnology experimental instruments such as an Atomic Force Microscope and a Scanning Electron Microscope, during Level 1 and then use this equipment to participate in hands-on exercises for nanoscale characterization at Level 2. Similarly, the generic ideas obtained from the Level 1 plotting exercise of intermolecular forces is discussed in greater detail at Level 3 when students acquire further knowledge about molecular forces and their influence on properties at the nanoscale, and familiarize themselves with computational codes that include the potential models necessary to simulate the

Table 10.1: Learning objectives of the spiral curriculum for the nanotechnology option.

Level	Course/Experience	Learning Objectives	
1	Nanotechnology module for freshmen (Implemented)	I.	Differentiate between macro and nano, and demarcate the domain of nanotechnology amongst different length scales
		II.	Describe the fundamental (intermolecular) forces significant at the nanoscale
		III.	Identify existing and potential engineering applications of nanotechnology
		IV.	Cite typical computational techniques and experimental instruments used in nanoscale research
2	Introduction to Nanoscale Characterization and Fabrication (Implemented)	I.	Describe common methods for imaging nanometer-size features
		II.	Describe common methods for manipulating features on this size scale
		III.	Describe common spectroscopy methods
		IV.	Explain the operating principle behind a nanotechnology instrument
		V.	Identify an appropriate tool to solve a nanotechnology problem
3	Introduction to Computational Molecular Mechanics (Being Developed)	I.	Describe the role of different intermolecular forces at the nanoscale
		II.	Explain the physics and mathematics behind molecular dynamics simulation technique
		III.	Construct simple molecular geometries of nanoscale systems and devices
		IV.	Conduct basic numerical experiments using pre-existing computational codes
		V.	Conduct literature review to be aware of the present scenario on a chose research topic in nanotechnology
		VI.	Prepare a report summarizing important conclusions of the project undertaken during the course
4	Undergraduate Research (Implemented)	I.	Conduct a literature review on a current research topic
		II.	Work in conjunction with a faculty advisor to develop an independent research plan for the topic
		III.	Explain the importance of ethical research conduct
		IV.	Demonstrate proper practices in research documentation and data collection
		V.	Conduct atomistic simulations of the nanoscale system specific to the research
		VI.	Fabricate the experimental sample and characterize the same using appropriate techniques
		VII.	Prepare a report and/or presentation appropriate to the project summarizing important conclusions

systems. These learning experiences again spiral into Level 4, when students take up independent research projects that involve both the experimental skills and simulation expertise

imparted during the previous levels of the curriculum.

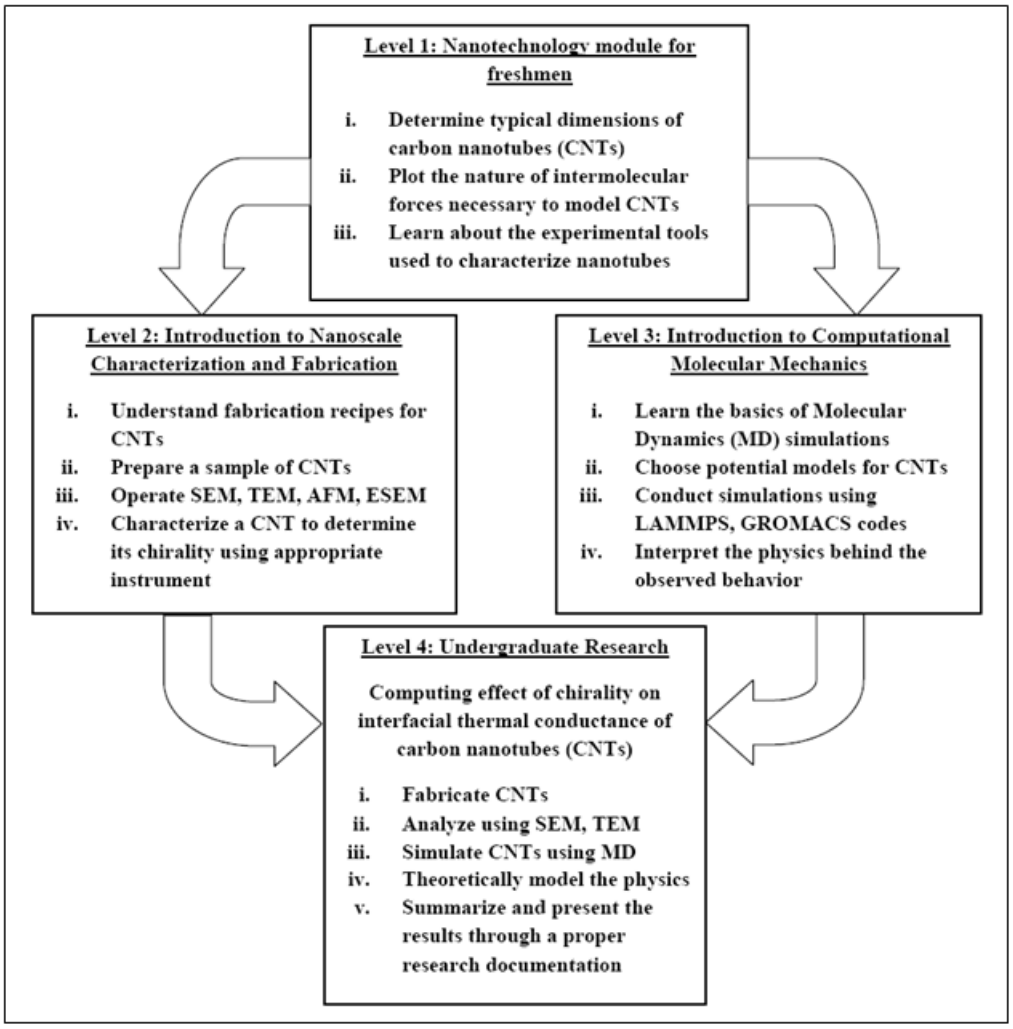

Figure 10.2: Knowledge areas including examples of hands-on activities and their relevance in the spiral theory-based nanotechnology option.

In order to further highlight the spiral theory concepts, a visual representation of the key learning experiences of the students at the four distinct learning levels of the nanotechnology option is shown in Figure 10.3. Level 1 indicates the fundamental ideas about the realm of nanotechnology to increase students' awareness and acquaintance to nanoscale systems and their potential applications. In Level 2, details about experimental characterization of nanoscale devices with hands-on sessions are provided to increase their skills with instruments

like a Scanning Electron Microscope (shown in the figure), an Atomic Force Microscope, a Transmission Electron Microscope, etc., which the students can employ for specific research problems. Level 3 includes modeling of nanoscale physical phenomena through atomistic simulations where the origin of intermolecular forces and their influence on system behavior are analyzed with the aid of molecular dynamics simulations. Students' spiraling experiences conclude with an undergraduate research project on a current research area in nanotechnology at Level 4 of the learning spiral. An example research project is to determine effects of chirality on the thermal conductance of carbon nanotubes. While students learn what carbon nanotubes are in Level 1, the characterization skill acquired in Level 2 enables them to visualize the chirality of carbon nanotubes in a sample. The computational ability obtained from Level 3 equips them to investigate the influence of chirality on the thermal conductance of carbon nanotubes.

At the time of this writing, the activities at Level 1 are included as a learning module in a freshman course, details of which are discussed in the following sections. The Level 2 activity is implemented in the form of a complete course that was offered for the first time in spring 2010. The Level 3 activity will be part of a course that is under development. Students have participated in nanotechnology related undergraduate research activities under the mentorship of faculty and senior graduate students in the ESM department. However, the recruitment of students to participate in the proposed nanotechnology option is ongoing at this time.

10.1.5 Nanotechnology option within the ESM department

ESM has 25 faculty members and about 130 undergraduate students from the sophomore to senior levels. The relatively small undergraduate program size makes it an excellent site to examine the effectiveness of instructional approaches, such as the nanotechnology option described here. As shown in Figure 10.1, all engineering freshmen are introduced to basic nanotechnology fundamentals regardless of their final major through our approach to initiate the spiral curriculum. In addition to repeating basic nanotechnology concepts in the ESM nanotechnology option, their learning experiences will focus on nanoscale material characterization and computational molecular mechanics. Students will also be expected to

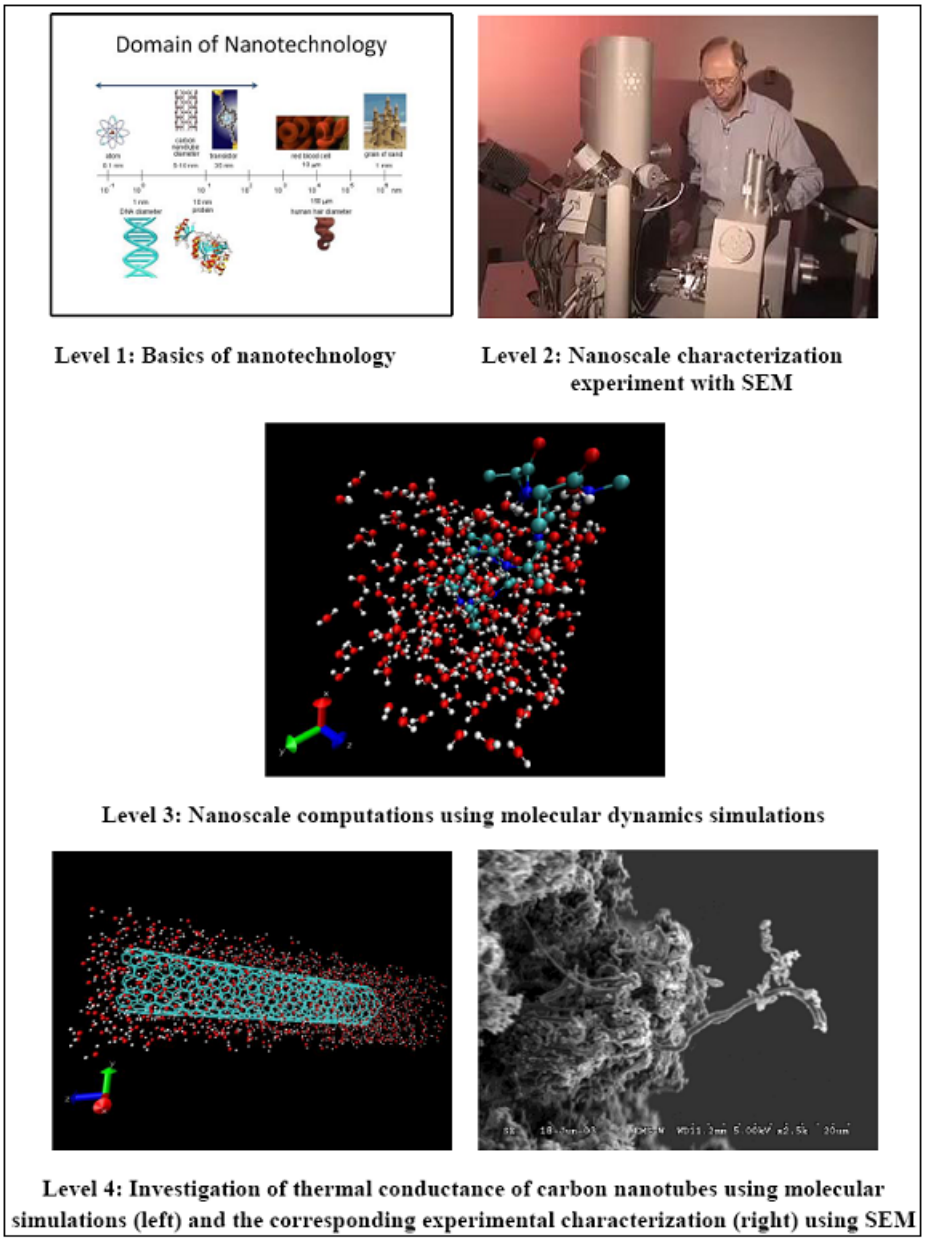

Figure 10.3: Visual representation of the different levels of the spiral curriculum.

conduct a nanotechnology-related research project mentored by CoE faculty members and the graduate students under their supervision. Table 10.2 provides details of the various courses and their contents.

Table 10.2: Summary of the various learning modules of the spiral curriculum approach.

Course/Experience	Proposed contents	Implementation plan
Nanotechnology module for freshmen	Prior knowledge survey; pre-test, nanotechnology lecture and video presentation; nanotechnology experiment video; hands-on activity using LabVIEW-based analysis; post-test	Implemented in Spring '08, Fall '08, and Spring '09 in EngE
Introduction to Nanoscale Characterization and Fabrication	Describe common methods for imaging and manipulating nanometer-size features; common spectroscopy methods; explain operating principle of nanotechnology instruments; identify appropriate tool to solve a nanotechnology problem	Implemented using NCFL equipment and ICTAS instructors in Spring '10
Introduction to computational molecular mechanics	Introduction to statistical mechanics and statistical thermodynamics; Newtonian dynamics for particle systems; soft and hard sphere models; stochastic and deterministic methods; parallel computing and algorithms	Being developed
Undergraduate research	Nanotechnology-based experimental, theoretical and computational research experiences	Implemented in ESM and ICTAS

10.1.6 Freshman engineering nanotechnology module

All Virginia Tech engineering freshmen are required to take a two-credit Engineering Exploration (EngE 1024) course during their first semester of enrollment in the GE program, which is the only common engineering course that all undergraduates take. The course focuses primarily on developing problem solving, critical thinking, and engineering design skills. The delivery format includes a fifty minute lecture followed by a ninety minute hands-on workshop every week.

The DLR project investigators have collected demographic data to describe the participants who have participated in various activities implemented as part of DLR project (Robson et al., 2008). Majority of students who participated in this study are engineering freshman at Virginia Tech's College of Engineering. Based on analysis of data of two engineering classes (i.e., class of 2008 and 2009) it is observed that the majority of the freshman engineering class is male (85%) and white (80%). In regards to prior background experiences, approximately 50% of the class has an engineer in the family and also has prior programming experience. In addition, the majority of students (75%) did not take any pre-engineering courses in high school. A survey was designed to ask students to indicate all of the engineering majors they were interested in, and students selected mechanical engineering (53%), followed by aerospace and ocean engineering (40%), electrical or computer engineering (37%) and civil or environmental engineering (33%). It may be noted that students were allowed to select multiple possible majors in this survey (Robson et al., 2008).

One of the learning objectives of the course is that students will be able to demonstrate a basic awareness of contemporary global issues and emerging technologies, and their impact on engineering practice after successful completion of the course. The nanotechnology module discussed here meets this objective. The nanotechnology learning module was piloted in EngE 1024 in the 2008 spring semester for approximately 180 students (Lohani et al., 2009b). Student feedback was used to enhance the module that was again implemented in the entire freshman class of about 1450 in the 2008 fall semester, and with further revisions in the 2009 spring semester to about 180 students. Therefore, approximately 1800 students have participated in learning basic nanotechnology concepts using this module. The following sections discuss the development, implementation and assessment of the module, and include assessment questions and web links to instructional videos that will enable interested educators to learn from it and also implement it.

10.2 Development of freshman level nanotechnology learning module

10.2.1 Spring 2008 pilot

Approximately 180 students enrolled in EngE 1024 in the 2008 spring semester. The nanotechnology module was piloted for the first time in this course. It included four components: (1) prior knowledge survey, (2) in-class presentation, (3) hands-on nanotechnology activities, and (4) post-module survey.

Prior knowledge survey: In order to assess students' prior knowledge related to nanotechnology, we developed a short survey of ten questions that are listed in Appendix B (question numbers 1-10). The survey was implemented two weeks before the classroom instruction and hands-on activities took place. Figure 10.4 presents student responses to select survey questions. About 73% knew the definition of a nanometer but roughly 43% thought that the gravitational force played a dominant role at the nanoscale. Most students did not understand the behavior of intermolecular attraction as molecules move apart and the repulsive forces when they move closer to each other. Most freshmen were incorrect by an order of magnitude when asked to identify the size of an atom. A majority thought that the most important application of nanotechnology was in the medical sciences. Although only 5% students reported prior exposure to basic nanotechnology concepts, 60% expressed an interest in learning about nanotechnology. These results were used to design an in-class presentation followed by a set of hands-on activities.

In-class presentation: A nanotechnology expert (the third author) developed this presentation in consultation with the other authors in two formats, i.e., as presentation slides and an online video. Figure 10.4 presents some of the slides for sake of illustration. The topics covered in the presentation are summarized in Table 10.4. These topics included, a background of nanotechnology development, the interdisciplinary nature of the subject involving physics, chemistry, biology and engineering disciplines, a comparison of the dominant forces at the macro- and nanoscales to help students to clear their misconceptions about the behavior of intermolecular and gravitational forces, nanostructures observed in nature, areas of applications with examples varying from novel electronic and semiconductor devices to

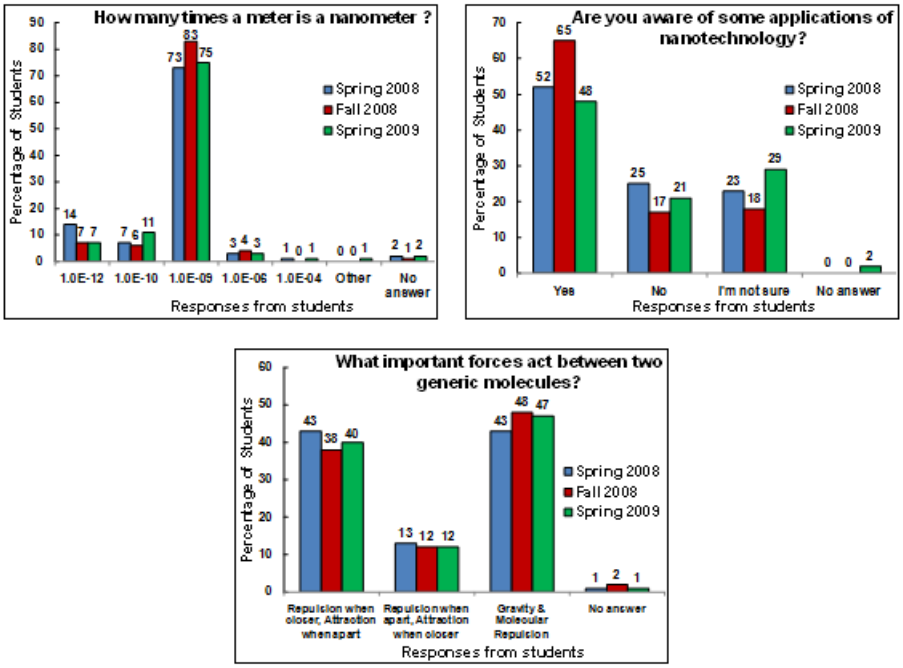

Figure 10.4: Student responses to some questions in the prior knowledge survey (Spring '08, N=99; Fall '08, N=868; Spring '09, N=149).

nanoparticles present in everyday applications like paints, and finally the societal and ethical issues associated with the technology. We have provided online links to this freshman module to enable access for the interested reader.

We took advantage of the classroom technology (i.e., Tablet PCs and DyKnow software) available to educators within the College of Engineering for developing interactive in-class presentations. Engineering freshmen at Virginia Tech are required to have a Tablet PC. The second author has developed and implemented technology enhanced classroom pedagogy using TabletPC and DyKnow technologies (Lohani et al., 2008a,b). These technologies were used during the nanotechnology presentation to develop an interactive learning environment. For example, in order to explain significance of various forces acting at the nanoscale, students were first asked to think about the dominant forces acting at the macroscale. They were assigned a short in-class exercise that involved sketching the various forces acting on an airplane (as shown in Figure 10.6). Student sketches were collected anonymously using the

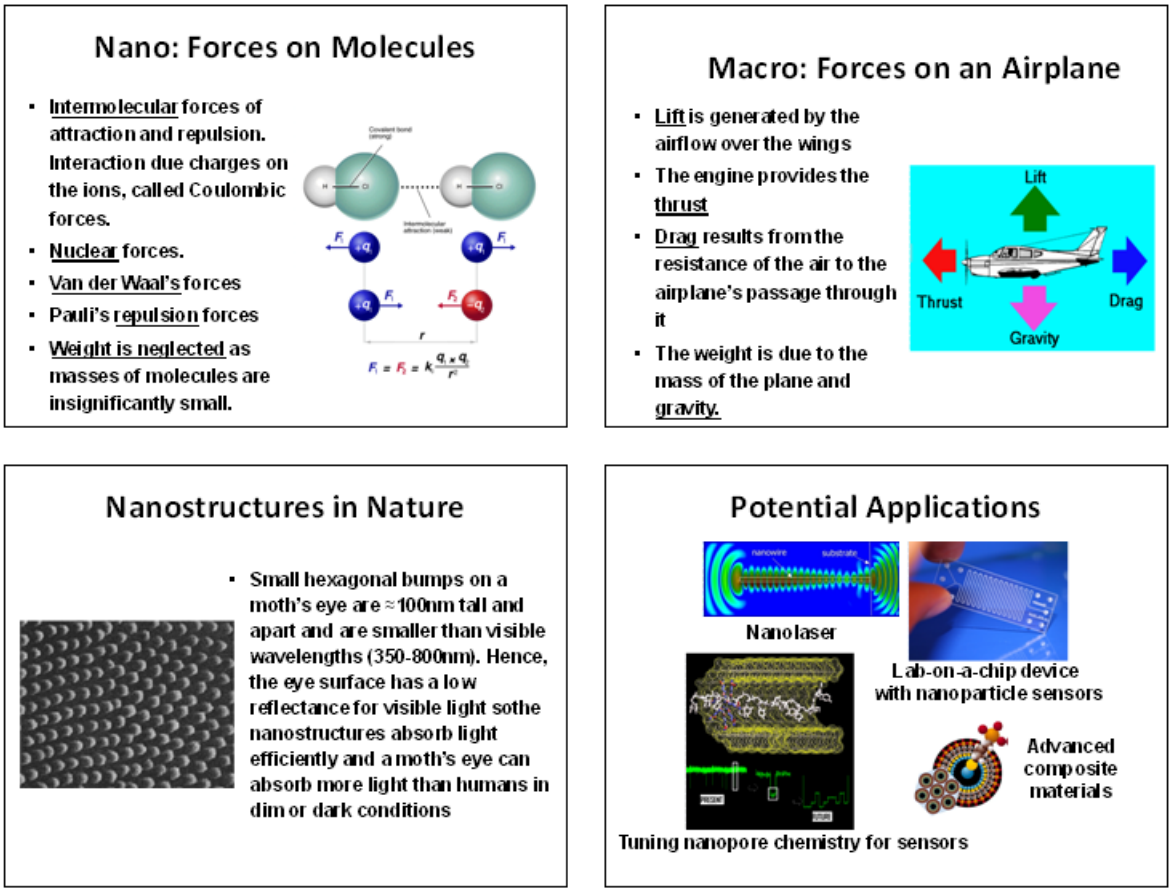

Figure 10.5: Slides from the in-class presentation.

TabletPC and DyKnow technologies. As shown in the figure, student 'A' was able to describe the different forces while student 'B' only considered gravity. Anonymously retrieved student sketches were displayed to the class shortly after they were retrieved to illustrate deficiencies. Thereafter, the instructor's slide that depicted the correct macroscale forces, also shown in Figure 10.6, was discussed.

Hands-on activity workshop: Students learn LabVIEW programming in EngE 1024 (Lohani et al., 2009a); thus we decided to use LabVIEW environment to introduce nanotechnology concepts. Keeping in mind the student misconceptions observed from the prior knowledge survey and academic preparation of students, three nanotechnology hands-on exercises were developed in a LabVIEW environment: (1) measurements of the typical dimensions of car-

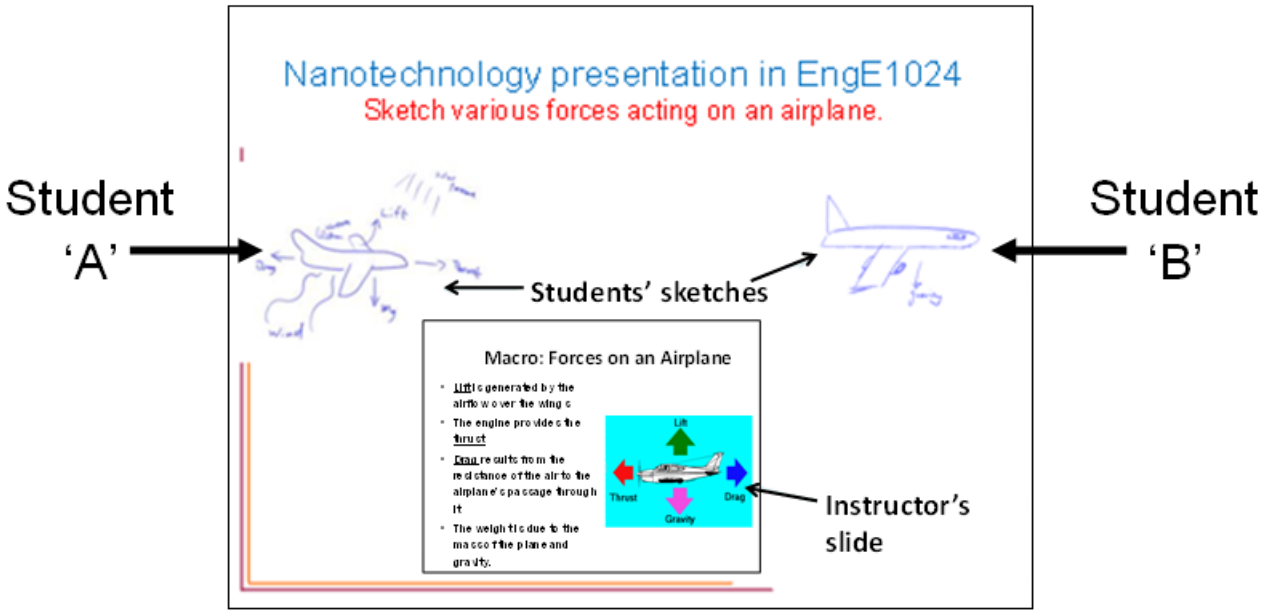

Figure 10.6: Example of feedback based classroom instruction.

bon nanotubes, (2) introduction to the Lennard-Jones potential function and its graphical analysis, and (3) analysis of the gravitational force between two molecular masses.

Students were provided with carbon nanotube images and used the LabVIEW VISION toolkit to measure their dimensions as illustrated in Figure 10.7a. In a second exercise, students were introduced to the Lennard-Jones potential function which is used to model intermolecular interactions. The students plotted the force derived from this function and analyzed the interaction forces between two molecules. These showed that increasing separation enhances intermolecular attraction while repulsive forces are strengthened as the two molecules come closer, as shown in Figure 10.7b. Finally, students plotted the gravitational force as a function of separation distance between two molecular masses. This exercise emphasized that gravitational forces are insignificant at the nanoscale due to the negligibly small molecular masses (see Figure 10.8).

Post-module survey: As part of the assessment activities for EngE 1024, a student exit survey has been implemented since the 2004 fall semester (Robson et al., 2007). Additional questions related to nanotechnology learning experiences were added to this survey, as follows:

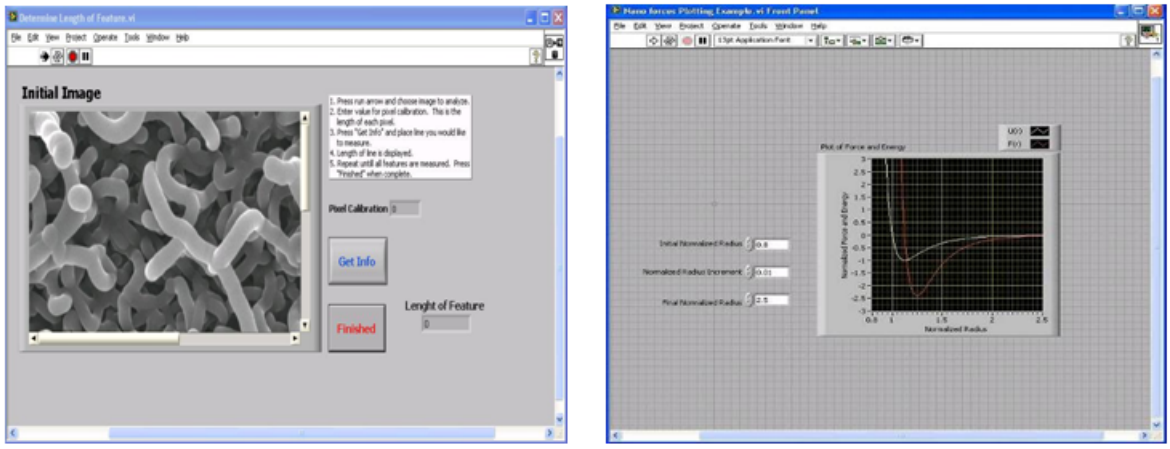

Figure 10.7: Hands-on analysis using the LabVIEW environment. (a) Determination of diameter of a carbon nanotube, and (b) plots of the Lennard-Jones potential and the force between two atoms.

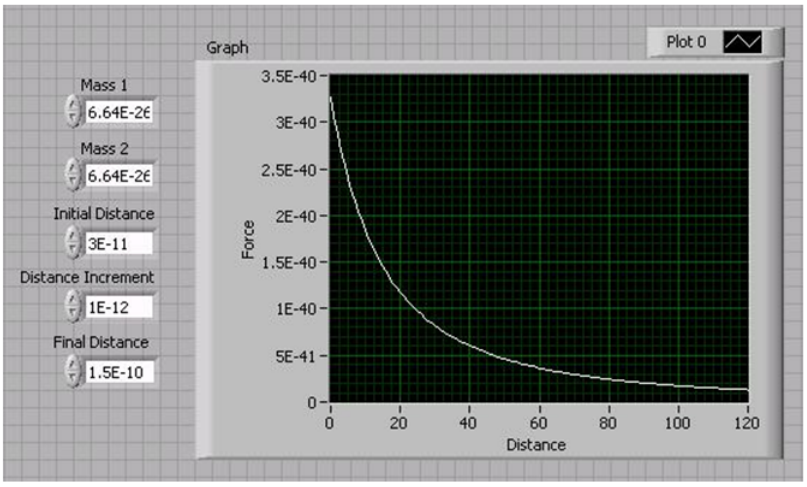

Figure 10.8: Gravitational force of attraction (shown in Newton) between two atoms separated by a certain distance (shown in meters) shows that not only is the force monotonic in nature but also that the magnitude of the attraction is negligible in comparison to the molecular forces present between the atoms.

1. Please recall (instructor's name)'s video presentation and workshop activities on nanotechnology this semester. These activities motivated me to pursue a nanotechnology minor/option. Strongly Agree/Agree/No Opinion/Disagree/Strongly Disagree

2. Do you see the relevance of nanotechnology in your intended major of engineering? Yes/No/I have not decided a major yet

3. Please comment on your overall experiences of learning about nanotechnology and provide suggestions for future improvement. (Free response)

Student responses were collected at the end of 2008 spring and fall, and 2009 spring semesters for which the results are discussed later.

10.2.2 Fall 2008 implementation

In the 2008 fall semester, approximately 1450 freshmen enrolled in EngE 1024. They were divided into eight large lecture sections that were further divided into 49 hands-on workshop sections. The lecture sections were taught by faculty members while graduate teaching assistants (GTAs) taught the workshop sections. All GTAs underwent two-week training on the basics of nanotechnology. This training covered fundamental principles of molecular interactions, the forces involved, and description of a simple potential model, Lennard-Jones potential, the relevance of the attractive and the repulsive terms, the insignificance of gravitational force at the nanoscale, discussion on the increase in surface area to volume ratio and its effects on material properties. The experiences gained during the 2008 spring semester were incorporated to implement changes into the nanotechnology learning module when it was taught in the 2008 fall semester. The module included: (1) prior knowledge survey, (2) forty minute nanotechnology video assigned as a homework assignment, (3) in-class question and answer session facilitated by the Tablet PC and DyKnow technologies, (4) hands-on activities, (5) video presentation on a nanotechnology experiment, (6) homework assignments on nanotechnology concepts, and (7) post-module survey.

Prior knowledge survey: The 2008 spring semester prior knowledge survey (question numbers 1-10 in Appendix B) was again implemented in the entire freshman class on a

voluntary basis and more than 50% students responded (Figure 10.4). Student responses again revealed the same misconceptions as during the 2008 spring semester pilot.

Nanotechnology video presentation: Students were again provided with an introduction to nanotechnology concepts through an online video and a slide presentation. It consisted of the same key topics discussed during the 2008 spring semester implementation of the module. Students were allowed one week to review a forty minute nanotechnology video developed by the nanotechnology expert and were instructed to come prepared to class to answer and ask questions on the various concepts presented in this video.

In-class question and answer sessions: Three Ph.D. students from ESM with nanotechnology research expertise assisted the EngE 1024 faculty instructors during in-class question and answer sessions on the nanotechnology concepts discussed in the video. Tablet PC and DyKnow technologies were used to obtain student responses to the following three questions:

1. List the forces that dominate intermolecular interactions.

2. List two engineering applications of nanotechnology discussed in this presentation. Can you also share example of an application that was not discussed in this presentation?

3. Suppose you are invited to your high school to give a short talk on your first year experiences at this university and you decided to say one thing about nanotechnology in this talk. What will you say?

Students were given about two minutes to provide written responses that were retrieved by instructors anonymously using TabletPC and DyKnow technologies. The ESM graduate students reacted to student feedback. Figure 10.9 lists some responses from students. That gravity is not a significant force at the nanoscale was explained to them. In response to the second question, students listed applications related to bio-nanotechnology, space elevators and microchips. Most students considered nanotechnology to be a significant emerging area for scientific research and predicted major development in the medical sciences. Some provided critical opinions about the negative aspects of such powerful technologies, with their imaginations suggesting the birth of "nano-babies" using DNA-mediated interactions, to producing "nano-weapons" and using destructive novel high energy physics applications.

Hands-on activities: The LabVIEW environment was again used to repeat the hands-on analysis activities of the 2008 spring semester pilot. However, in order to provide further insight into the dimensions of carbon nanotubes, a new exercise was developed that compared surface area to volume ratio of a nanotube with that of a large PVC plumbing pipe. Students were asked to measure the diameter and length of a typical nanotube using the VISION Toolkit in LabVIEW and to calculate the ratio. They were also provided with the dimensions of a typical PVC plumbing pipe and asked to compare its ratio with that of the nanotube. Table 10.3 summarizes the typical values that students obtained. This exercise demonstrated the significant increase in the surface area to volume ratio at the nanoscale that can be favorable for biochemical, and heat and mass transfer applications. The exercise complemented the discussion of this topic in the video presentation and emphasized nanotechnology concepts more than the LabVIEW concepts.

Table 10.3: Comparison of the surface area to volume ratio between a nanotube and a PVC pipe.

Dimension	Carbon Nanotube	PVC Pipe
Diameter	24.39nm = 24.39×10^{-9}m	5×10^{-3} m
Surface area	7.66×10^{-13} m^2	1.57 m^2
Volume	4.67×10^{-21} m^3	1.96×10^{-3} m^3
Surface area/Volume	1.64×10^{8} m^{-1}	8×10^{2} m^{-1}

Nanotechnology experiment video: In response to student feedback during the 2008 spring semester pilot, a video demonstrating a basic nanotechnology experiment was developed at the NCFL. Students were assigned to watch this seven minute video that demonstrated a nanotechnology experiment using a Scanning Electron Microscopy (SEM) to capture high resolution magnified images of a human hair and of carbon nanotubes. An SEM expert briefly explained the techniques involved in the preparation of the samples and the salient features and capabilities of the instrument. The large size of our freshman engineering class and high cost of nanotechnology experiment equipment were the main reasons we decided to

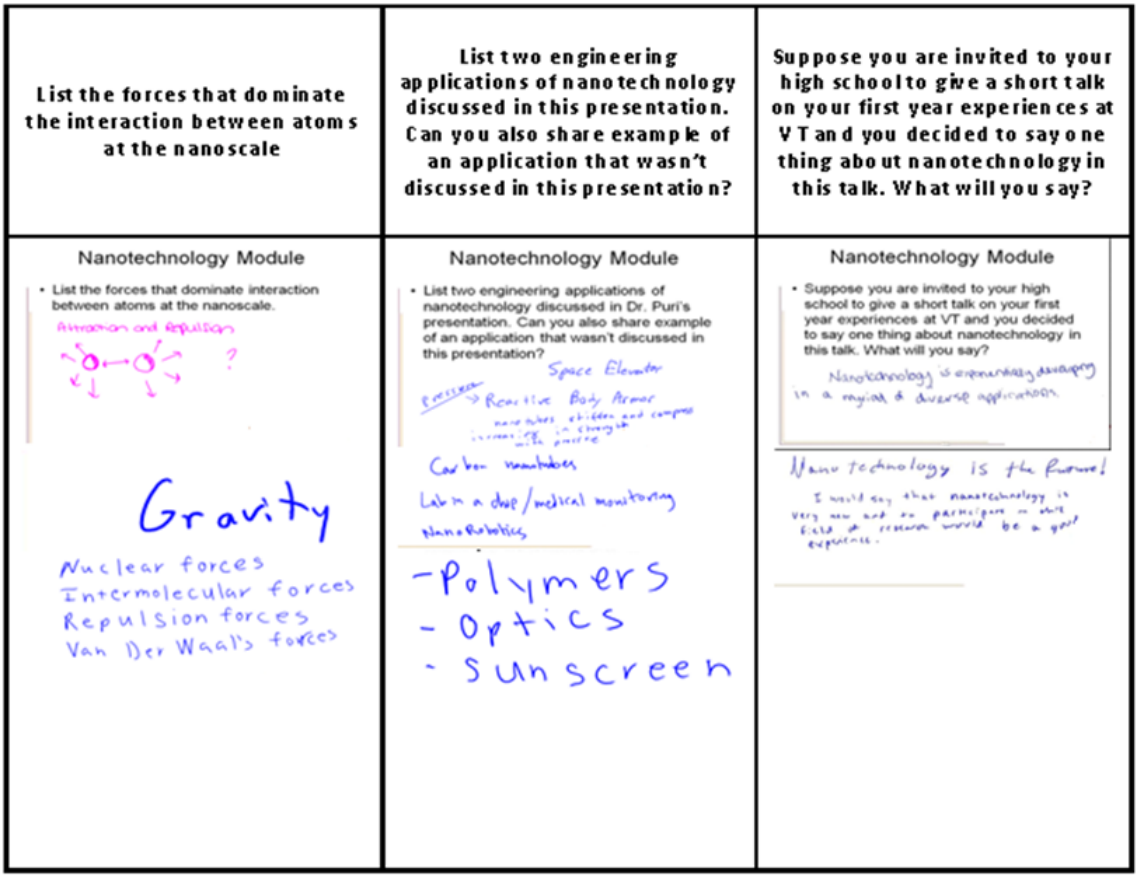

Figure 10.9: Examples of student responses during in-class question and answer session.

use an experimental video instead of asking students to participate in the experiment.

Post-module survey: Questions added to the EngE 1024 exit survey in the 2008 spring semester pilot were asked of all freshmen at the end of the 2008 fall semester. About 314 students responded. These responses are summarized in Figures 10.11(a-b). Students felt that the video presentation was too long and incorporated a variety of complex nanotechnology concepts. They indicated their preference for a shorter video that covered a few major fundamental concepts but contained greater discussion of applications. Many students, especially those who did not plan to further study nanotechnology as part of their curriculum, found the detailed discussion of the concepts covered in the video to be difficult to understand. Most students still thought that the hands-on analysis placed greater emphasis on LabVIEW

skills rather than a real-time demonstration of nanoscale activity.

10.2.3 Spring 2009 module

The 2008 fall semester module was modified further to address student concerns. A revised module was implemented in EngE 1024 for about 180 freshmen during the 2009 spring semester. Instead of the prior knowledge and post-module surveys, the students were asked to voluntarily participate in a pre- and a post-test. The prior knowledge survey implemented during the previous two semesters was modified appropriately to develop the test questions. A shortened twenty minute version of the video presentation was created. The 2009 spring semester implementation included: (1) pre-test, (2) nanotechnology videos and slides assigned as a homework assignment, (3) nanotechnology experiment video as a homework assignment, (4) in-class question and answer session assisted by Tablet PC and DyKnow technologies, (5) hands-on analysis activities, and (6) post-test.

Pre-test: Over 80% of students voluntarily participated in the pre-test which contained twelve questions (Appendix B), i.e., all questions that were asked of the students through the prior knowledge survey in the 2008 spring and fall semesters (numbers 1-10 in Appendix B) with two additional questions (numbers 11-12 in Appendix B). Again, the pre-test results indicated that students were unclear about the role of gravity at the nanoscale (as shown in Figure 10.12).

Nanotechnology video presentation: Students were allowed a week to review a twenty minute nanotechnology video and the corresponding slides. The link to the longer version of the nanotechnology video, developed for the 2008 fall semester was provided for an optional activity.

Post-test: After completion of all nanotechnology instruction, students were asked to complete a post-test survey. There was significant improvement in the previously noted student misconceptions (as shown in Figure 10.12). However, notably, after the completion of the module only about 18% of the students still believed that gravity was dominant at the nanoscale.

10.3 Nanotechnology module for freshman engineering students

In this section, we provide details of the components of the freshman nanotechnology learning module that should enable an educator to implement the module.

10.3.1 Pre- and post-tests

This multiple choice test is presented in Appendix B. An online link to this test was created and students were requested to complete it on a voluntary basis before the instruction occurred. We made it very clear that student scores on this test would not influence their course grades. The same test was administered as a post-test once all instructional activities were completed.

10.3.2 Nanotechnology video presentation and slides

Table 10.4 summarizes the key topics included in the nanotechnology video and slides.

Table 10.4: Key concepts discussed in the nanotechnology presentation.

Key topics included in the presentation on nanotechnology
Brief history of the subject
Domain of nanotechnology amongst different length scales
Interdisciplinary aspects
Comparison of macroscale and molecular forces
Molecular mechanics
Material behavior at the nanoscale
Nanostructures in nature
Applications- Everyday uses, electronics, nano-biotechnology etc.
Ethical issues

The video and slides can be viewed at:

http://www.vbs.vt.edu/content/adhoc/fall2008/Puri_Nanotech/

Students accessed above instruction materials from Blackboard sites. While the authors have not recorded data on frequency of students' accessing these materials, our another study indicates that use of classroom technology (like Blackboard, TabletPCs, and DyKnow) have been effective in developing a feedback-based learning environment in the classroom.

10.3.3 Nanotechnology experiment video

A nanotechnology characterization experiment on carbon nanotube and human hair samples was analyzed with an SEM at the NCFL. The salient points of this video are presented in Table 10.5.

Table 10.5: Salient features of a nanoscale characterization experiment using SEM.

Key topics demonstrated in the nanotechnology experiment
Facilities at the NCFL, ICTAS, Virginia Tech
Capabilities and uses of Scanning Electron Microscopy (SEM)
Applications of different nanoscale materials
Sample preparation and mounting
Image analysis and appropriate magnification for carbon nanotubes and human hair test samples
Measurement of typical dimensions
Phase determination using EDS spectra for other samples

The video is available at: http://light.vbs.vt.edu/adhoc/fall2008/ICTAS08.mov

It may be mentioned that the videos discussed above were professionally done with the support of the Virginia Tech Video/Broadcast Services (VBS).

10.3.4 Hands-on workshop activities

The LabVIEW environment was used to develop and implement hands-on activities for the nanotechnology module. Figures 10.10(a-d) show images of the LabVIEW Virtual Instru-

ments (Vis) created to (1) plot the attractive and repulsive forces due to the Lennard-Jones potential between two interacting molecules, and (2) measurements of typical carbon nanotube dimensions using the VISION toolkit of LabVIEW. The basic concepts involved in the LabVIEW Vis are applications of different data types, use of built-in functions like add, multiply, subtract and power, incorporating a while loop structure and the knowledge of shift registers. Before implementing the nanotechnology module, students learned these LabVIEW concepts as part of programming instruction in EngE 1024. Instructions for implementing this hands-on exercise are provided below:

- Cover the fundamentals of LabVIEW programming (i.e., data types, control structures, and plotting concepts).
- Have students install the VISION toolkit which is an add-on to the LabVIEW.
- Provide students with carbon nanotube image files and the supporting LabVIEW VIs for image analysis and plotting. The files can be accessed at:
  https://filebox.vt.edu/users/bganesh/NUE:%20Spiral%20Approach/
  Username: filebox.nue, password: lohani
- Explain the Lennard Jones (L-J) potential and force expressions, the role played by the material parameters, and discuss the attractive and the repulsive terms.
- In-class work (Total time of sixty minutes distributed equally to three different activities):
  1. Determination of size (20 minutes): Calculate the length and diameter of a typical carbon nanotube. The exercise involves a briefing of the concepts of pixel calibration in order to convert the measured dimension from pixels to corresponding length units, e.g., in micrometers or nanometers.
  2. Plot the L-J force function (20 minutes): Using the basics of LabVIEW programming to graph the L-J force expression with the values for material parameters provided to the students by the instructor. The exercise involves locating the value for the inter-atomic separation distance for which this force becomes zero, positive, and negative.

3. Calculate the surface area to volume ratio of a typical carbon nanotube and compare it with that for a standard PVC pipe (20 minutes): The dimensions for the PVC pipe and the formulae for obtaining the surface area to volume ratio are provided to students beforehand, while carbon nanotube diameter and length are computed by students using the LabVIEW exercise (a) analyzing a given image. The purpose of this activity is to show the marked difference in geometric characteristics that arises from the large surface areas of the nanostructures in comparison to their macroscale counterparts. Also, this activity laid more emphasis on nanotechnology concepts (e.g., high surface area to volume ratio) as opposed to LabVIEW concepts.

10.4 Assessment

We now summarize student responses to the exit survey, and pre- and post-test questions on a semester-wise basis. Two key instruction-related inputs from students in 2008 spring semester were: (1) hands-on activities should emphasize nanotechnology concepts over LabVIEW concepts, and (2) students expressed their desire to observe an actual nanotechnology experiment in order to develop a better understanding and appreciation for this emerging technology. Regarding the in-class presentation, many students felt that too much fundamental material was covered in a single lecture and suggested that nanotechnology applications be equally emphasized. A majority thought that nanotechnology was relevant to their majors with about 18% showing interest in pursuing a minor or option in nanotechnology.

Students taking the class during its 2008 fall semester implementation felt that the video presentation on nanotechnology was too long and also suggested that a shorter presentation be prepared that focused more on nanotechnology applications. As in the previous semester, students wanted greater emphasis placed on nanotechnology concepts during the hands-on activities with lower stress placed on LabVIEW programming skills.

Figure 10.11 provides a summary of student responses in the course exit survey for all three semesters. On average, about 18% of students expressed an interest in pursuing a nanotechnology minor or option. About 55% saw nanotechnology education relevant to their

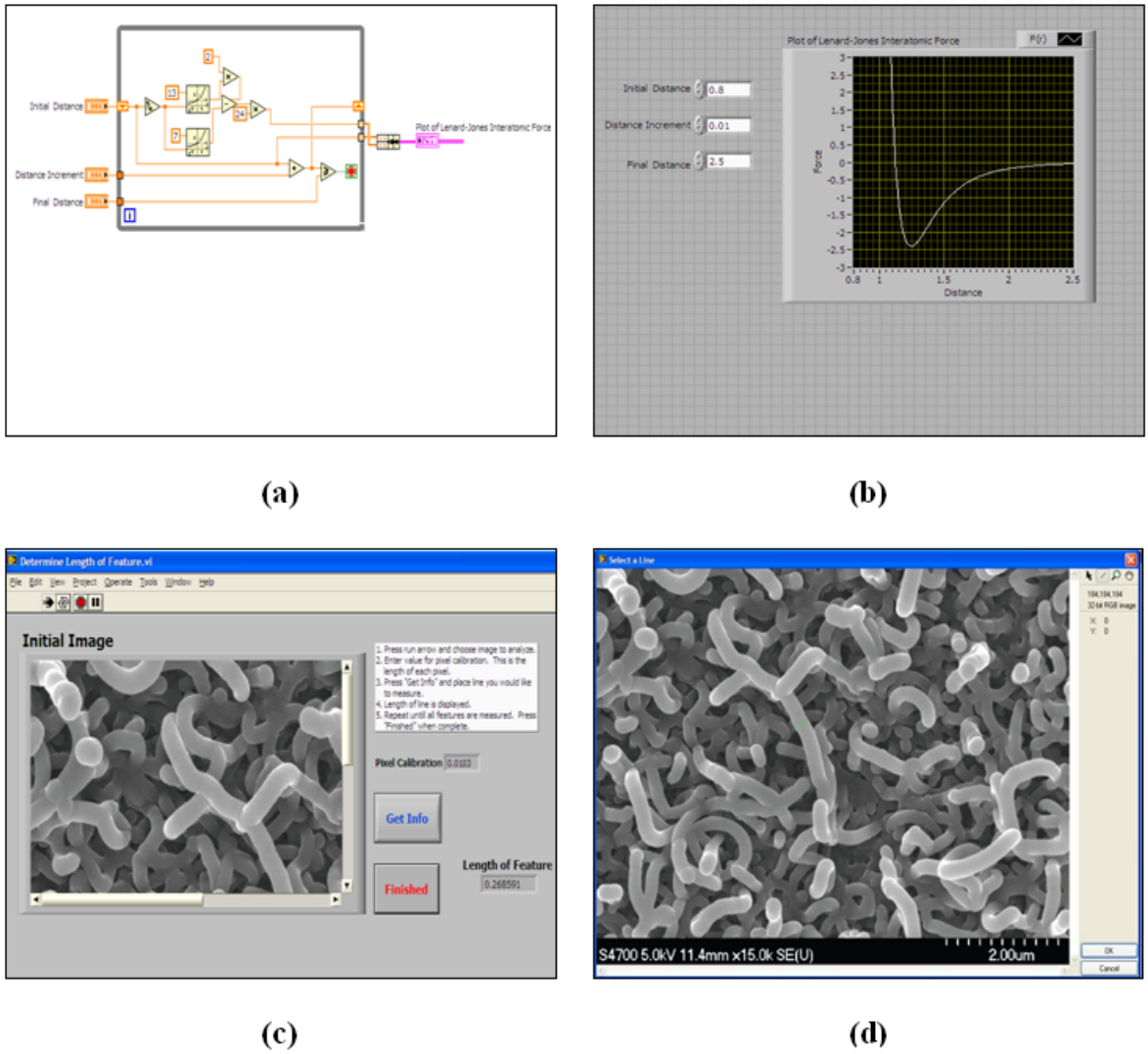

Figure 10.10: LabVIEW activities developed for hands-on exercises involving plotting of Lennard-Jones interatomic force. (a) represents the LabVIEW block diagram and (b) shows the front panel showing the attractive (negative) and repulsive (positive) natures of the interaction force between two atoms with respect to the separation distance between them; (c) and (d) represent the exercise using LabVIEW VISION toolkit used by students to calculate the dimension (diameter, length) of a carbon nanotube.

intended engineering major.

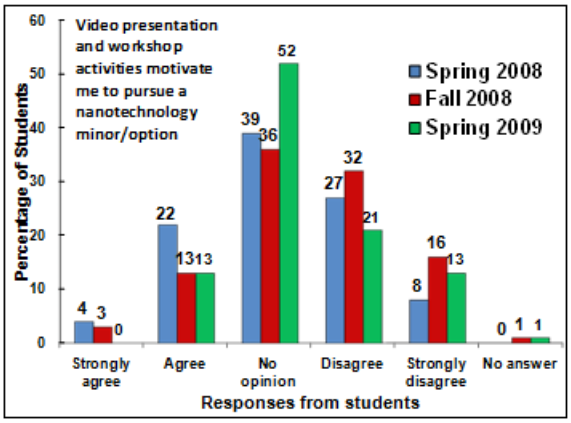

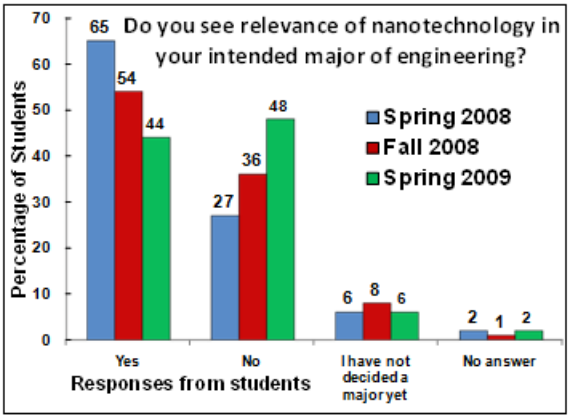

Figure 10.11: Student responses to post-module survey (Spring '08, N=49; Fall '08, N=314; Spring '09, N=66).

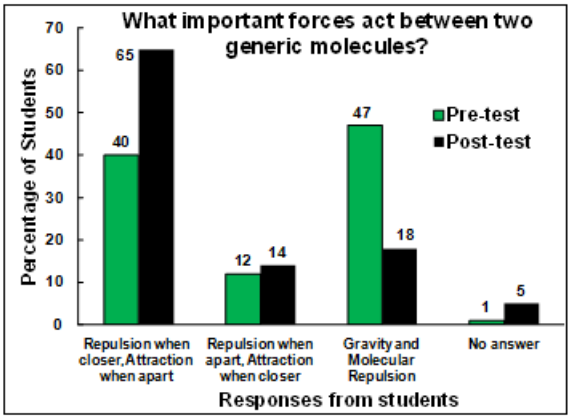

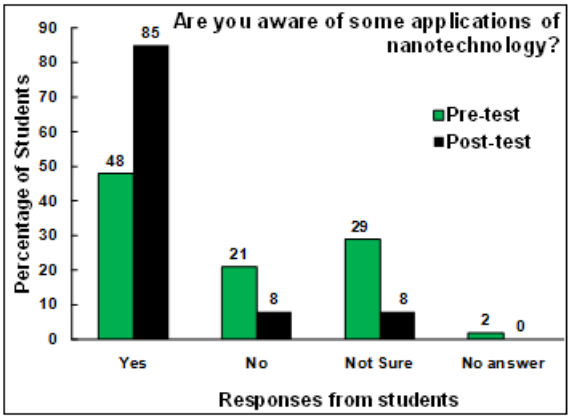

Figure 10.12: Student responses to key questions asked of them during the pre-test (N=149) and again during the post-test (N=66) of the Spring '09 module implementation.

The results of the pre-and post-tests administered in the 2009 spring semester presented in Figure 10.12 showed significant improvement in the student misconceptions that were also observed during the previous semesters. Compared to 48% students in the pre-test, about 85% appeared to have developed an awareness of various nanotechnology applications.

Since 149 students took the pre-test and 66 participated in the post-test, there were at least 35 students who participated in both tests. (Thus at least 53% of the students partici-

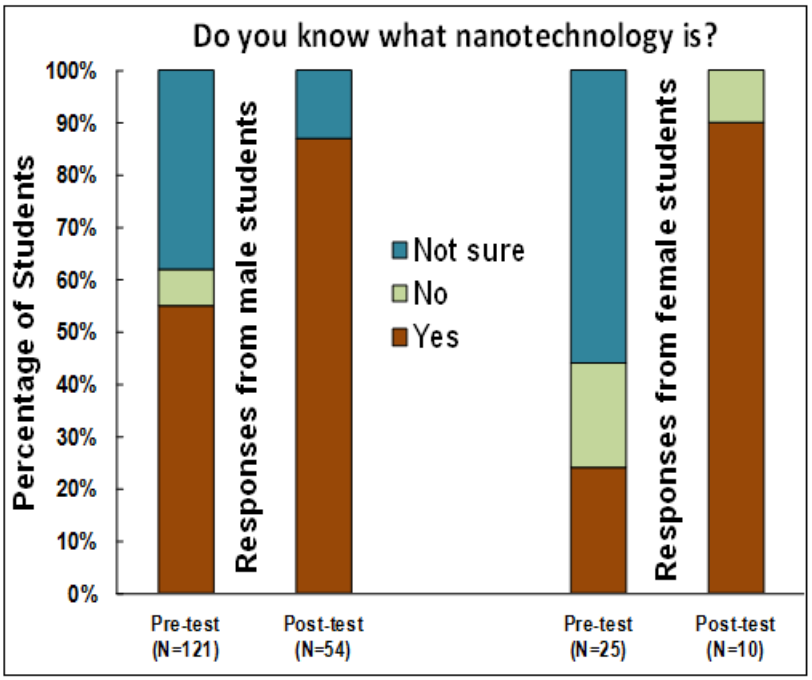

Figure 10.13: Students' interest in nanotechnology assessed according to their gender.

pated in both tests.) This leads us to assume that the results reflect a significant improvement in the students' understanding of nanotechnology concepts. Student responses were analyzed to observe the influence of self-reported gender on their nanotechnology learning experiences. As shown in Figure 10.13, 55% of male students and 20% of females expressed awareness of nanotechnology concepts in the pre-test. We do not have data to support either way whether this difference in prior knowledge between males and females is a function of their high school experiences. However, the post-test results showed that 85% students in both groups communicated knowledge of these concepts. This represents statistically significant increase in proportion of students, both males and females, demonstrating awareness of nanotechnology concepts at a significance level (α) of 0.001. We acknowledge the small data samples as a limitation of this study. It may be noted that students' participation in the pre-and post-tests was on a voluntary basis. This did affect students' participation rate particularly on the post-test since this was implemented toward the end of the semester when students get busy in wrapping up various course projects, assignments, reports, etc. Also, Tablet PC

/DyKnow based formative assessment technique seems to have a great potential in developing a feedback-loop in classroom and analysis of students' responses indicate positive learning experiences as a result of these technologies.

10.5 Recommendations

We have described a collaborative project between two engineering departments and an interdisciplinary university research institute at Virginia Tech to creating a nanotechnology option based on the well established spiral theory. The option includes nanotechnology topics with increasing levels of complexity. We have provided details regarding the development of a freshman module that has been taught to approximately 1800 students. We found that a video presentation covering nanotechnology fundamentals for freshmen that exceeds twenty minutes in length is not well received by students and that students are eager to observe an actual nanotechnology experiment. The LabVIEW software offers a suitable environment to develop hands-on analysis activities for nanotechnology concepts. However, these activities should emphasize nanotechnology concepts more than the LabVIEW concepts. While we realize the benefit of hands-on activities in a laboratory setting to enhance the learning, the size of our program prevents us from doing so. Following instruction, about 18% freshmen expressed interest in pursuing a nanotechnology option.

We are currently discussing a number of issues, e.g., (1) Are the current educational tools available to a typical engineering educator good enough to teach concepts associated with emerging technologies which are highly interdisciplinary in nature? (2) Is the hands-on learning paradigm a good and feasible one for all kinds of learning? How do we teach our students the power of abstraction especially when it comes to emerging technologies? (3) How can we take advantage of the information technology skills of today's students (e.g., through their social networking, web browsing, online communication, and other habits) to facilitate the learning of emerging technology concepts. We continue to explore these and other questions and welcome input and participation from our readers. Interested readers are also encouraged to contact the authors to obtain additional information about our nanotechnology curriculum. Further, this education theory based curriculum development work motivated authors

to successfully pursue another grant under the ethics education in science and engineering (EESE) program of the NSF. A spiral approach is considered to weave ethics instruction throughout the undergraduate curriculum in this EESE grant and authors have conducted workshops for faculty and graduate students for wider dissemination of this approach. A comprehensive survey is implemented in the entire College of Engineering for assessing the status of ethics instruction both in undergraduate and graduate curricula.

Acknowledgment

We acknowledge the support of the National Science Foundation through Grant 0741364. We thank all EngE 1024 instructors and graduate teaching assistants who helped us in implementing the nanotechnology module for the entire freshman class, Mr. Steve McCartney of NCFL, ICTAS, and Video/Broadcast Services, both at Virginia Tech, for helping us develop the nanotechnology experiment video, and to Dr. Terry Wildman, Professor of Education Psychology at Virginia Tech, who introduced us to the spiral curriculum theory.

Chapter 11

What's next?

¨ Imagination will often carry us to worlds that never were. But without it we go nowhere. ¨
— Carl E. Sagan

11.1 Opportunities for future research

Several significant problems of fundamental interest, but with important insinuations, are inviting us to explore them. As mentioned earlier, our motivation for investigating the hydration and diffusion behavior of ionic solutions is driven by their thermochemical energy storage capabilities. It is well known that on hydration of dehydrated salts, nucleation effects play an important role in determining the energy release capabilities of the salt. Since we have described the mobility and structural orientations of $MgSO_4$ in details, it would be a worthwhile study to now look into the cooling of the heated dehydrated salt, and understand how different cooling rates influence the recrystallization of hydrated salt. While the study is of fundamental interest, accurate computations of the energy of desolvation can provide guidelines to suitably design and employ thermochemical energy storage and release mechanisms, for example to warm homes and offices.

The range of variation of thermal conductivity of carbon nanotubes (CNTs) and graphene sheets together with their large mechanical strength can be employed in transport of energy. In addition, being good conductors of electricity, armchair CNTs can be suitably employed as thermoelectrics. To increase the figure of merit for improved thermoelectric performance, the

reduction in phonon thermal conductivity by isotope substitution is one strategy, as discussed. Other possible avenues include using other elements as impurities, and understand how the difference in mass as well as the electronic configuration influences transport coefficients. Thermal conductivity will reduce not only by transfer of modes, but scattering mechanisms will become significant in such cases and influence motion of electrons and electric current.

Atomistic-continuum hybrid models have essentially focused on thermal transport processes that involves contributions of uncharged atoms. Extending such models to incorporate solid-solid and solid-fluid interactions that include interfacial effects due to charges in addition to contributions of lattice vibrations and layering of fluid on solid surfaces are important to characterize nanoscale devices across the molecular to the continuum scales. Typical examples of such systems include, but not limited to, motion of charged ions in an electrolytic solution between electrodes, where a comprehensive multiscale understanding of the transport is crucial to accurately estimate the energy storage and release for specific operations like in batteries.

Integrating education with research is important, and exposing undergraduate and even high school students to the current developments in technology is necessary. While the spiral model discussed earlier is one such approach, more nonlinear models that tailor the learning objectives along the lines of established pedagogies for students' learning are essential. Future opportunities lie in designing such novel curricula and courses, and understanding the effect of those of students' learning. These might pave way for new tools to improve the teaching practices for the latest advances in science and engineering.

Appendix A

Velocity profile for stagnation flow

From the continuity equation for an incompressible flow,

$$\nabla.\vec{u} = 0$$
$$\text{(for a 2D flow) } \frac{\partial u}{\partial x} + \frac{\partial v}{\partial y} = 0 \tag{A.1}$$

For small (x, y), from Taylor series expansion about the stagnation point, S$(x = 0, y = 0)$ where $u_{_S} = v_{_S} = 0$,

$$\begin{aligned} u(x,y) &= u_{_S} + \left(\frac{\partial u}{\partial x}\right)_{_S} x + \left(\frac{\partial u}{\partial y}\right)_{_S} y + ...\text{(neglecting higher order terms)} \\ &= 0 + \alpha x + \beta y, \text{ where } \alpha = \left(\frac{\partial u}{\partial x}\right)_{_S} \text{ and } \beta = \left(\frac{\partial u}{\partial y}\right)_{_S} \qquad \text{(A.2)} \\ v(x,y) &= v_{_S} + \left(\frac{\partial v}{\partial x}\right)_{_S} x + \left(\frac{\partial v}{\partial y}\right)_{_S} y + ...\text{(neglecting higher order terms)} \\ &= 0 + ax + by, \text{ where } a = \left(\frac{\partial v}{\partial x}\right)_{_S} \text{ and } b = \left(\frac{\partial v}{\partial y}\right)_{_S} \qquad \text{(A.3)} \end{aligned}$$

So $u = \alpha x + \beta y$, $v = ax + by$ when substituted in Equation A.1,

$$u = \alpha x + \beta y$$
$$v = ax - \alpha y \tag{A.4}$$

For an irrotational flow,

$$\nabla \times \vec{u} = 0$$
$$\text{(for a 2D flow) } \frac{\partial u}{\partial y} - \frac{\partial v}{\partial x} = 0 \tag{A.5}$$

Therefore,

$$u = \alpha x + \beta y$$
$$v = \beta x - \alpha y \tag{A.6}$$

For the stagnation flow problem shown in Figure 4.1, in the vicinity of the stagnation zone, $u(x_c, y_c) = -u(-x_c, y_c)$. Thus, $\beta = 0$ and

$$u = \alpha x$$
$$v = -\alpha y \tag{A.7}$$

Magnified versions of the Figures 4.2 and 4.3 in Chapter 4 are provided below.

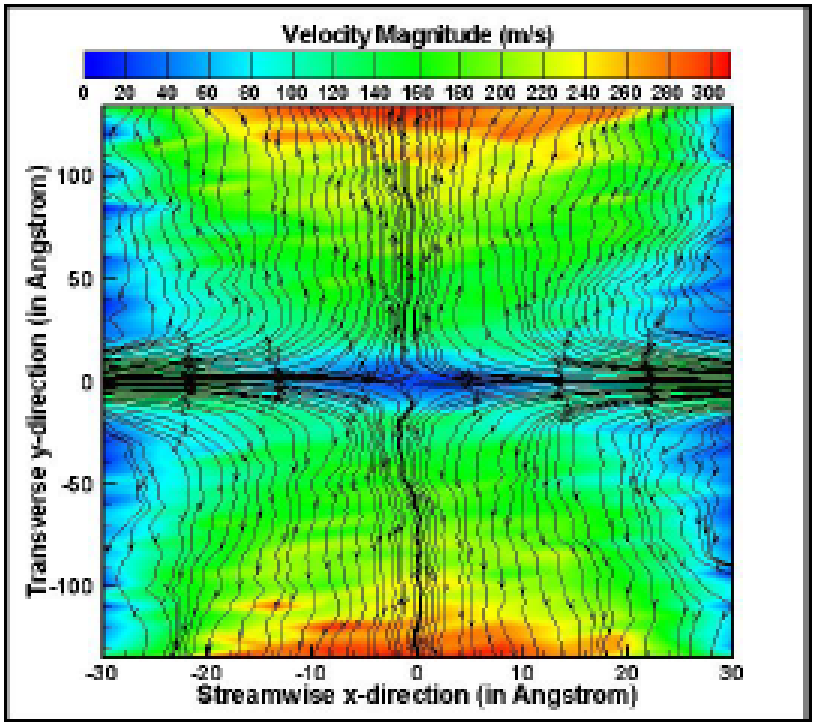

(a)

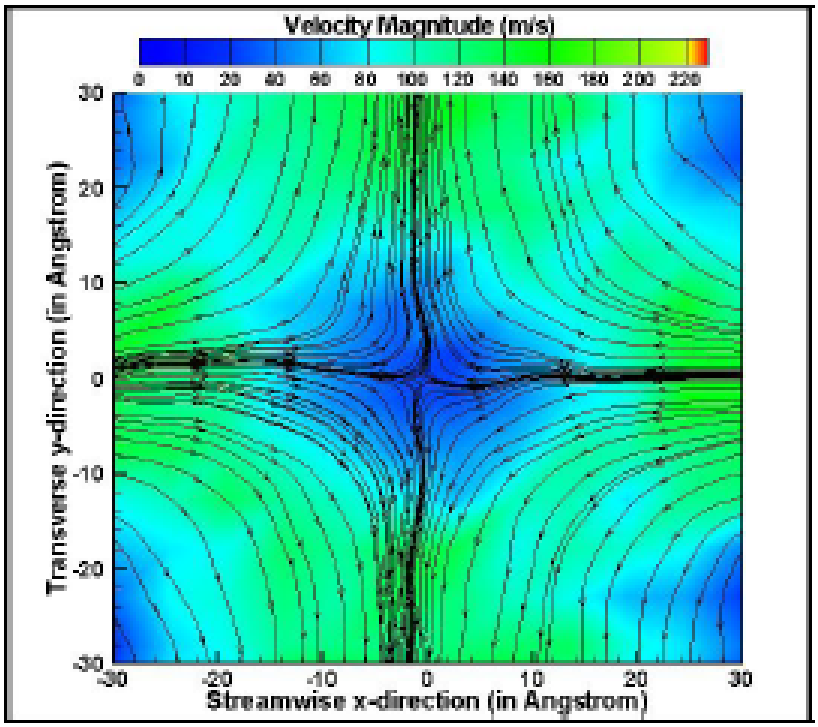

(b)

Figure A.1: Magnified version of Figures 4.2a and 4.2b.

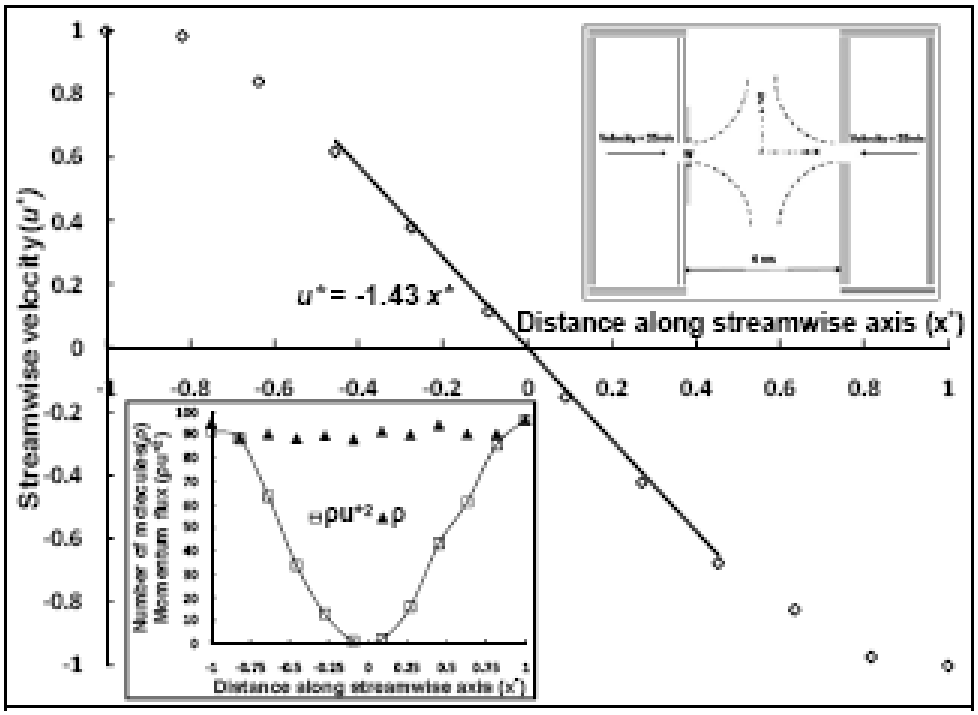

(a)

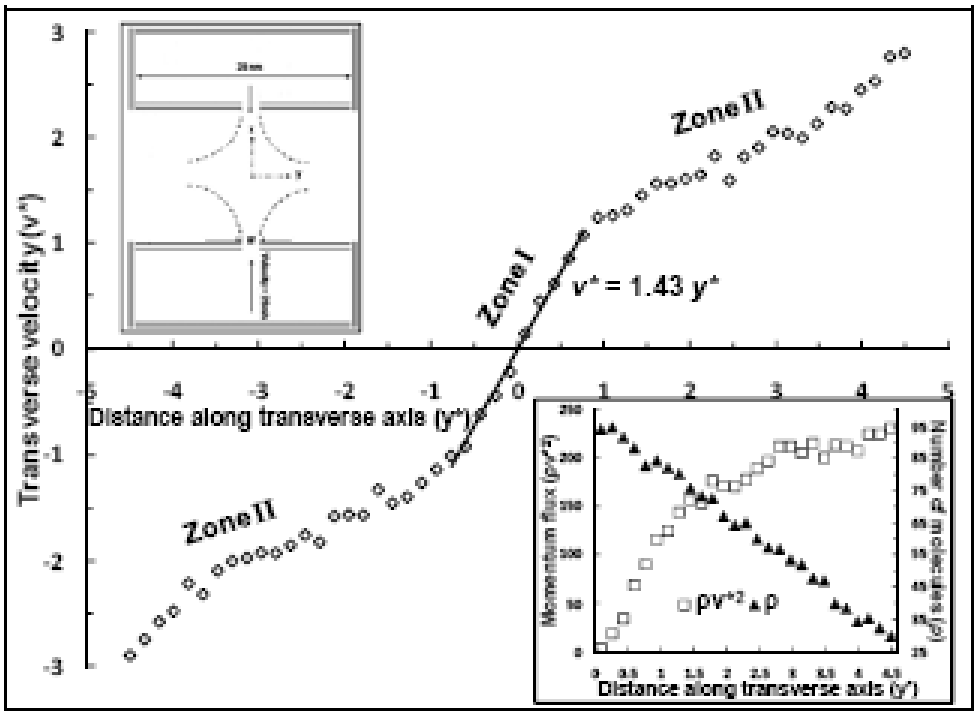

(b)

Figure A.2: Magnified version of Figure 4.3.

Appendix B

Pre-test and post-test questions

List of questions with the multiple choices for responses asked of students in the pre-test and post-test during the 2009 spring semester:

1. Your intended area of engineering is:

2. Gender (optional):

3. Do you know what nanotechnology is?
   Yes/No/Not Sure

4. Nanotechnology involves
   (a) Research and technology development involving structures with at least one dimension in approximately the 1-100 nanometer range (b) Creating and using structures, devices and systems that have novel properties and functions because of their nanometer scale dimensions (c) Ability to control or manipulate on the atomic scale All the above/Only a and b/Only b and c/ Only a and c/ None of these

5. What is a nanometer?
   10^{-12}m/10^{-10}m/10^{-9}m/10^{-6}m/10^{-4}m/Other

6. Typically, what is the value of an atom's diameter?
   10^{-12}m/10^{-11}m/10^{-10}m/10^{-9}m/10^{-8}m/10^{-6}m/Other

7. What influences an apple as it falls from a tree?

   The fluid drag on it from the surrounding air/Gravity/Gravity and fluid drag from the surrounding air/The earth's electric field/The earth's electric field and gravity and fluid drag/Sunspots/Sunspots and the earth's electric field and gravity and fluid drag

8. What important forces act on two different generic molecules as they approach each other?

   Attraction between molecules when they are far apart and repulsion between them as they come closer/Repulsion between molecules when they are far apart and attraction as they come closer/The gravitational force and the molecular repulsion between molecules

9. For how long do you think have scientists been formally working on nanotechnology?

   Last decade/last twenty years/last fifty years/last century/last millennium

10. Are you aware of some applications of nanotechnology?

    Yes/No/Not Sure

11. Nanotechnology can be used for the following applications:

    (a) Tissue Engineering (b) Water treatment/ filtration (c) Increasing energy (d) Semiconductor devices (e) Drug targeting All the above/Only a,b,c/Only a,c,d/Only b,c,e/Only a,d,e/Only a,b,d,e/None of these

12. What are the typical test samples/materials used in nanoscale experiments? Check all that apply

    Human hair/Carbon Nanotube/Silicon Nanotube/Gold Nanoparticles/Bacteria

Bibliography

Alaghemandi, M., Algaer, E., Böhm, M. C., and Müller-Plathe, F. The thermal conductivity and thermal rectification of carbon nanotubes studied using reverse non-equilibrium molecular dynamics simulations. *Nanotechnology*, 20(11):115704, 2009.

Alaghemandi, M., Schulte, J., Leroy, F., Müller-Plathe, F., and Böhm, M. On the correlation between thermal conductivity and bond length alternation in carbon nanotubes: a combined reverse-non equilibrium md-crystal orbital analysis. *Journal of Computational Chemistry*, 32:121–133, 2011.

Allen, M. P. and Tildesley, D. J. *Computer Simulation of Liquids*. Clarendon Press, Oxford, UK, 1987.

Anthony, T. R., Banholzer, W. F., Fleischer, J. F., Wei, L. H., Kuo, P. K., Thomas, R. L., and Pryor, R. W. Thermal-diffusivity of isotopically enriched C-12 diamond. *Physical Review B*, 42(2):1104–1111, 1990.

Antia, M., Herricks, T., and Rathod, P. K. Microfluidic modeling of cell-cell interactions in malaria pathogenesis. *Plos Pathogens*, 3(7):939–948, 2007.

Anwar, S. and Dhillon, H. Development of an on-line introduction to nanotechnology course: Issues and challenges. In *ASEE Annual Conference and Exposition, Conference Proceedings*, Pittsburg, PA, United States, 2008.

Ashcroft, N. and Mermin, N. *Solid State Physics*. Holt, Rinehart and Winston, New York, 1976.

Auerbach, S. M. Theory and simulation of jump dynamics, diffusion and phase equilibrium in nanopores. *International Reviews in Physical Chemistry*, 19(2):198, 2000.

Augustine, B. H., Reisner, B. A., and Caran, K. L. The nanoscience undergraduate education (NUE) program at James Madison University. In *Materials Research Society Symposium Proceedings*, San Francisco, CA, United States, 2006.

Balasubramanian, G., Banerjee, S., and Puri, I. K. Unsteady nanoscale thermal transport across a solid-fluid interface. *Journal of Applied Physics*, 104(6):064306, 2008.

Balasubramanian, G., Puri, I. K., and Ragab, S. A. Dynamics of impinging nanoscale jets. *Chemical Physics Letters*, 491(4-6):177–182, 2010a.

Balasubramanian, G., Murad, S., Kappiyoor, R., and Puri, I. K. Structure of aqueous $MgSO_4$ solution: Dilute to concentrated. *Chemical Physics Letters*, (in press), 2011.

Balasubramanian, G., Ghommem, M., Hajj, M. R., Wong, W. P., Tomlin, J. A., and Puri, I. K. Modeling of thermochemical energy storage by salt hydrates. *International Journal of Heat and Mass Transfer*, 53(25-26):5700–5706, 2010b.

Banerjee, S., Murad, S., and Puri, I. K. Preferential ion and water intake using charged carbon nanotubes. *Chemical Physics Letters*, 434(4-6):292–296, 2007.

Barrat, J. L. and Chiaruttini, F. Kapitza resistance at the liquid-solid interface. *Molecular Physics*, 101(11):1605–1610, 2003.

Bastea, S. Transport in a highly asymmetric binary fluid mixture. *Physical Review E*, 75(3), 2007.

Batra, R. C. and Spinello, D. Analysis of adiabatic shear bands in heat-conducting elastothermoviscoplastic materials by the meshless local Bubnov-Galerkin method. *Communications in Numerical Methods in Engineering*, 25:1019–1040, 2008.

Batra, R. C. and Zhang, G. M. SSPH basis functions for meshless methods, and comparison of solutions with strong and weak formulations. *Computational Mechanics*, 41(4):527–545, 2008.

Becker, B., Schelling, P. K., and Phillpot, S. R. Interfacial phonon scattering in semiconductor nanowires by molecular-dynamics simulation. *Journal of Applied Physics*, 99(12):123715, 2006.

Berendsen, H. J. C., Grigera, J. R., and Straatsma, T. P. The misssing term in effective pair potentials. *Journal of Physical Chemistry*, 91(24):6269–6271, 1987.

Berendsen, H., Postma, J., van Gunsteren, W., and Hermans, J. In Pullman, B., editor, *Intermolecular forces : proceedings of the Fourteenth Jerusalem Symposium on Quantum Chemistry and Biochemistry held in Jerusalem, Israel, April 13-16, 1981*. D. Reidel, Dordrecht, Holland; Boston, U.S.A., 1981.

Bickle, J., Iyer, S., Mantei, T., Papautsky, I., Schulz, M., Shanov, V., Smith, L., and Steckl, A. Integration of nanoscale science and technology into undergraduate curricula. In *2006 6th IEEE Conference on Nanotechnology, IEEE-NANO 2006*, Cincinnati, OH, United States, 2006.

Bonny, G., Pasianot, R. C., and Malerba, L. Fe-Ni many-body potential for metallurgical applications. *Modelling and Simulation in Materials Science and Engineering*, 17(2):025010, 2009.

Boukai, A. I., Bunimovich, Y., Tahir-Kheli, J., Yu, J. K., Goddard, W. A., and Heath, J. R. Silicon nanowires as efficient thermoelectric materials. *Nature*, 451(7175):168–171, 2008.

Brenner, D. W., Shenderova, O. A., Harrison, J. A., Stuart, S. J., Ni, B., and Sinnott, S. B. A second-generation reactive empirical bond order (REBO) potential energy expression for hydrocarbons. *Journal of Physics-Condensed Matter*, 14(4):783–802, 2002.

Bruner, J. *The Process of Education*. Harvard University Press, Cambridge, MA, USA, 1960.

Bruner, J. *The Culture of Education*. Harvard University Press, Cambridge, MA, 1996.

Cahill, D. G. Analysis of heat flow in layered structures for time-domain thermoreflectance. *Review of Scientific Instruments*, 75(12):5119–5122, 2004.

Cahill, D. G. and Watanabe, F. Thermal conductivity of isotopically pure and Ge-doped Si epitaxial layers from 300 to 550 K. *Physical Review B*, 70(23):235322, 2004.

Cahill, D. G., Ford, W. K., Goodson, K. E., Mahan, G. D., Majumdar, A., Maris, H. J., Merlin, R., and Phillpot, S. R. Nanoscale thermal transport. *Journal of Applied Physics*, 93(2):793–818, 2003.

Callaway, J. Model for lattice thermal conductivity at low temperatures. *Physical Review*, 113(4):1046–1051, 1959.

Cannon, W. R., Pettitt, B. M., and McCammon, J. A. Sulfate anion in water - Model structural, thermodynamic, and dynamic properties. *Journal of Physical Chemistry*, 98 (24):6225–6230, 1994.

Challis, L. J. Kapitza resistance and acoustic transmission across boundaries at high frequencies. *Journal of Physics C: Solid State Physics*, 7(3):481–495, 1974.

Chandra, A. Effects of ion atmosphere on hydrogen-bond dynamics in aqueous electrolyte solutions. *Physical Review Letters*, 85(4):771, 2000.

Chandrasekhar, J. and Jorgensen, W. L. The nature of dilute solutions of sodium-ion in water, methanol and tetrahydrofuran. *Journal of Chemical Physics*, 77(10):5089, 1982.

Chang, C. W., Fennimore, A. M., Afanasiev, A., Okawa, D., Ikuno, T., Garcia, H., Li, D. Y., Majumdar, A., and Zettl, A. Isotope effect on the thermal conductivity of boron nitride nanotubes. *Physical Review Letters*, 97(8):085901, 2006.

Chang, T., Jaroonsiriphan, P., and Xuemei, S. Integrating nanotechnology into undergraduate experience: A web-based approach. *International Journal of Engineering Education*, 18(5):557–65, 2002.

Chantrenne, P. Multiscale simulations: application to the heat transfer simulation of sliding solids. *International Journal of Material Forming*, 1(1):31–37, 2008.

Chantrenne, P., Barrat, J. L., Blase, X., and Gale, J. D. An analytical model for the thermal conductivity of silicon nanostructures. *Journal of Applied Physics*, 97(10):104318, 2005.

Chaplin, M. F. In Lynden-Bell, R. M., Morris, S. C., Barrow, J. D., Finney, J. L., and Charles L. Harper, J., editors, *Water of Life: The Unique Properties of H_2O*. CRC Press, Boca Raton, FL, USA, 2010.

Chaudhuri, D., Chaudhuri, A., and Sengupta, S. Heat conduction through a trapped solid: The effect of structural changes on the thermal conductance. *Journal of Physics-Condensed Matter*, 19(15):152201, 2007.

Chen, G. Particularities of heat conduction in nanostructures. *Journal of Nanoparticle Research*, 2(2):199–204, 2000a.

Chen, G. Phonon heat conduction in nanostructures. *International Journal of Thermal Sciences*, 39(4):471–480, 2000b.

Chen, G. Nanoscale heat transfer and nanostructured thermoelectrics. *IEEE Transactions on Components and Packaging Technologies*, 29(2):238–246, 2006.

Chen, G., Narayanaswamy, A., and Dames, C. Engineering nanoscale phonon and photon transport for direct energy conversion. *Superlattices and Microstructures*, 35(3-6):161–172, 2004.

Chen, G. *Nanoscale energy transport and conversion : A parallel treatment of electrons, molecules, phonons, and photons*. Oxford University Press, Oxford; New York, 2005.

Chen, J., Zhang, G., and Li, B. W. Tunable thermal conductivity of $Si_{1-x}Ge_x$ nanowires. *Applied Physics Letters*, 95(7):073117, 2009.

Chen, J., Zhang, G., and Li, B. W. Remarkable reduction of thermal conductivity in silicon nanotubes. *Nano Letters*, 10(10):3978–3983, 2010.

Cheng, S., Zhao, Y. H., Wang, Y. M., Li, Y., Wang, X. L., Liaw, P. K., and Lavernia, E. J. Structure modulation driven by cyclic deformation in nanocrystalline NiFe. *Physical Review Letters*, 104(25):255501, 2010.

Chevalier, J., Tillement, O., and Ayela, F. Rheological properties of nanofluids flowing through microchannels. *Applied Physics Letters*, 91(23), 2007.

Chevalier, J., Tillement, O., and Ayela, F. Structure and rheology of SiO_2 nanoparticle suspensions under very high shear rates. *Physical Review E*, 80(5), 2009.

Choi, Y. S., Kim, S. J., and Kim, M. U. Molecular dynamics of unstable motions and capillary instability in liquid nanojets. *Physical Review E*, 73(1):016309, 2006.

Chow, T. S. Viscosities of concentrated dispersions. *Physical Review E*, 48(3):1977–1983, 1993.

Chu, S. C. and Song, S. L. An undergraduate nanotechnology course for classes of multi-discipline students in Taiwan. In *Materials Research Society Symposium Proceedings*, San Francisco, CA, United States, 2006.

Clark, W. M., DiBiasio, D., and Dixon, A. G. Project-based, spiral curriculum for introductory courses in ChE. Part 1. Curriculum design. *Chemical Engineering Education*, 34(3): 222–227, 2000.

Cowan, P., Morrison, H., and McBride, E. Evidence of a spiral curriculum using a mathematical problem-solving tool. *Interactive Learning Environments*, 6(3):205–24, 1998.

Dai, C. F. and Chang, R. Y. Molecular dynamics simulation of thread break-up and formation of droplets in nanoejection system. *Molecular Simulation*, 35(4):334–341, 2009.

Darabi, J. Micro- and nanoscale heat transfer: Challenges and opportunities. *Heat Transfer Engineering*, 23(2):1–2, 2002.

Das, S. K., Putra, N., and Roetzel, W. Pool boiling characteristics of nano-fluids. *International Journal of Heat and Mass Transfer*, 46(5):851–862, 2003.

Davey, A. Boundary-layer flow at a saddle point of attachment. *Journal of Fluid Mechanics*, 10:593–610, 1961.

Daw, M. S., Foiles, S. M., and Baskes, M. I. The Embedded-Atom Method: A review of theory and applications. *Materials Science Reports*, 9(7-8):251–310, 1993.

DiBiasio, D., Comparini, L., Dixon, A. G., and Clark, W. M. A project-based spiral curriculum for introductory courses in ChE: Part 3. Evaluation. *Chemical Engineering Education*, 35(2):140–146, 2001.

Dismukes, J. P., Ekstrom, E., Steigmeier, E. F., Kudman, I., and Beers, D. S. Thermal and electrical properties of heavily doped Ge-Si alloys up to 1300 degrees K. *Journal of Applied Physics*, 35(10):2899–2907, 1964.

Dixon, A. G., Clark, W. M., and Dibiasio, D. Project-based, spiral curriculum for introductory courses in ChE. Part 2. Implementation. *Chemical Engineering Education*, 34(4): 296–303, 2000.

Donadio, D. and Galli, G. Atomistic simulations of heat transport in silicon nanowires. *Physical Review Letters*, 102(19):195901, 2009.

Dong, J. J., Sankey, O. F., and Myles, C. W. Theoretical study of the lattice thermal conductivity in Ge framework semiconductors. *Physical Review Letters*, 86(11):2361–2364, 2001.

Dupuis, A. and Koumoutsakos, P. Effects of atomistic domain size on hybrid lattice Boltzmann-molecular dynamics simulations of dense fluids. In *15th International Conference on Discrete Simulation of Fluid Dynamics*, Geneva, Switzerland, 2006.

Dupuis, A., Kotsalis, E. M., and Koumoutsakos, P. Coupling lattice Boltzmann and molecular dynamics models for dense fluids. *Physical Review E*, 75(4):046704, 2007.

Easteal, A. J., Price, W. E., and Woolf, L. A. Hydration models for trivalent metal-ion solutions - Diffusion of Fe(III) and 3HHO and shear viscosities in Iron(III) Perchlorate solutions at 298 K. *Journal of Physical Chemistry*, 93(21):7517–7520, 1989.

Eastman, J. A., Phillpot, S. R., Choi, S. U. S., and Keblinski, P. Thermal transport in nanofluids. *Annual Review of Materials Research*, 34:219–246, 2004.

Eggers, J. Dynamics of liquid nanojets. *Physical Review Letters*, 89(8):084502, 2002.

Elizondo, L. L., Cid, A., and Hernandez, M. Main features of the curriculum 2001 at the Ignacio A. Santos School of Medicine, Monterrey, Mexico. In *6th annual meeting of the International Association of Medical Science Educators*, Jalisco, Mexico, 2002.

Emel'yanov, M. I. Self-diffusion of water molecules in aqueous solutions of electrolytes: II. Bromides and Iodides of metals. *Journal of Structural Chemistry*, 6(2):273, 1965.

Emel'yanov, M. I., Nikiforov, E. A., and Kucheryavenko, N. S. Self-diffusion of water molecules in aqueous solutions of electrolytes: IV. Hydration of the hydroxonium ion H_3O^+. *Journal of Structural Chemistry*, 9(6):852, 1969.

Faltin, H. A. *The magnetic and electrical properties of permalloy-carbon thin film multilayers.* PhD thesis, College of William and Mary, 2000.

Fan, G. J., Fu, L. F., Choo, H., Liaw, P. K., and Browning, N. D. Uniaxial tensile plastic deformation and grain growth of bulk nanocrystalline alloys. *Acta Materialia*, 54(18): 4781–4792, 2006.

Fang, T. H., Chang, W. J., and Liao, S. C. Simulated nanojet ejection process by spreading droplets on a solid surface. *Journal of Physics - Condensed Matter*, 15(49):8263–8270, 2003.

Fang, T. H., Chang, W. J., and Liao, S. C. Effects of temperature and aperture size on nanojet ejection process by molecular dynamics simulation. *Microelectronics Journal*, 35 (9):687–691, 2004.

Fisher, E. and Mahajan, R. L. Midstream modulation of nanotechnology research in an academic laboratory. In *American Society of Mechanical Engineers International Mechanical Engineering Congress and Exposition*, Chicago, Illinois, 2006.

Freund, J. B. The atomic detail of an evaporating meniscus. *Physics of Fluids*, 17(2):022104, 2005.

Galli, G. and Donadio, D. Thermoelectric materials: Silicon stops heat in its tracks. *Nature Nanotechnology*, 5(10):701–702, 2010.

Gao, B. and Liu, Z. F. A first principles study on the solvation and structure of $SO_4^{2-}(H_2O)$(n), n=6-12. *Journal of Chemical Physics*, 121(17):8299–8306, 2004.

Geballe, T. H. and Hull, G. W. Isotopic and other types of thermal resistance in Germanium. *Physical Review*, 110(3):773–775, 1958.

Gingold, R. A. and Monaghan, J. J. Smoothed particle hydrodynamics - Theory and application to non-spherical stars. *Monthly Notices of the Royal Astronomical Society*, 181(2): 375–389, 1977.

Gonzalez, M. A. and Abascal, J. L. F. The shear viscosity of rigid water models. *Journal of Chemical Physics*, 132(9), 2010.

Guajardo-Cuellar, A., Go, D. B., and Sen, M. Evaluation of heat current formulations for equilibrium molecular dynamics calculations of thermal conductivity. *Journal of Chemical Physics*, 132(10):104111, 2010.

Guardia, E. and Padro, J. A. Molecular dynamics simulation of single ions in aqueous solutions: Effects of the flexibility of the water molecules. *The Journal of Physical Chemistry*, 94(15):6049–6055, 1990.

Guardia, E., Sese, G., Padro, J. A., and Kalko, S. G. Molecular dynamics simulation of Mg^{2+} and Ca^{2+} ions in water. *Journal of Solution Chemistry*, 28(10):1113–1126, 1999.

Gupta, V., Joseph, B., Alcanter, N., Toomey, R., and Sunol, R. A spiral curriculum for chemical engineering. In *Proceedings of the Annual Meeting of the AIChE*, Philadelphia, PA, 2008.

Hadjiconstantinou, N. G. Hybrid atomistic-continuum formulations and the moving contact-line problem. *Journal of Computational Physics*, 154(2):245–265, 1999.

Hadjiconstantinou, N. G. and Patera, A. T. Heterogeneous atomistic-continuum representations for dense fluid systems. In *6th International Conference on Discrete Models for Fluid Mechanics*, Boston, MA, USA, 1996.

Hadjiconstantinou, N. G. and Patera, A. T. Heterogeneous atomistic-continuum representations for dense fluid systems. *International Journal of Modern Physics C*, 8(4):967–976, 1997.

Haile, J. *Molecular Dynamics Simulation Elementary Methods*. John Wiley & Sons, New York, USA, 1997.

Hanasaki, I., Yonebayashi, T., and Kawano, S. Molecular dynamics of a water jet from a carbon nanotube. *Physical Review E*, 79(4):046307, 2009.

Hegab, H., Palmer, J., and Napper, S. Development of a nanosystems engineering degree. In *Innovations in Engineering Education 2005: Mechanical Engineering Education, Mechanical Engineering Technology Department Heads*, Orlando, FL, United States, 2005.

Henderson, J. R. and Vanswol, F. On the interface between a fluid and a planar wall - Theory and simulations of a hard-sphere fluid at a hard wall. *Molecular Physics*, 51(4):991–1010, 1984.

Hess, B., Kutzner, C., van der Spoel, D., and Lindahl, E. GROMACS 4: Algorithms for highly efficient, load-balanced, and scalable molecular simulation. *Journal of Chemical Theory and Computation*, 4(3):435–447, 2008.

Heyes, D. M. and March, N. H. Theoretical approaches to thermal conductivity in liquids. *Physics and Chemistry of Liquids*, 33(2):65–83, 1996.

Hochbaum, A. I., Chen, R. K., Delgado, R. D., Liang, W. J., Garnett, E. C., Najarian, M., Majumdar, A., and Yang, P. D. Enhanced thermoelectric performance of rough silicon nanowires. *Nature*, 451(7175):163–167, 2008.

Holz, M., Heil, S. R., and Sacco, A. Temperature-dependent self-diffusion coefficients of water and six selected molecular liquids for calibration in accurate H-1 NMR PFG measurements. *Physical Chemistry Chemical Physics*, 2(20):4742, 2000.

Hu, M., Goicochea, J. V., Michel, B., and Poulikakos, D. Thermal rectification at water/functionalized silica interfaces. *Applied Physics Letters*, 95(15):51903, 2009.

Hu, M., Giapis, K., Goicochea, J., Zhang, X., and Poulikakos, D. Significant reduction of thermal conductivity in Si/Ge core-shell nanowires. *Nano Letters*, 11:618–623, 2011.

Hu, Z. Sustainable nanotechnology education for engineers. In *ASEE Annual Conference and Exposition, Conference Proceedings*, Pittsburg, PA, United States, 2008.

Hughes, A. J. The Einstein relation between relative viscosity and volume concentration of suspensions of spheres. *Nature*, 173(4414):1089–1090, 1954.

Humphrey, W., Dalke, A., and Schulten, K. VMD: Visual molecular dynamics. *Journal of Molecular Graphics*, 14(1):33–38, 1996.

Huxtable, S., Cahill, D. G., Fauconnier, V., White, J. O., and Zhao, J. C. Thermal conductivity imaging at micrometre-scale resolution for combinatorial studies of materials. *Nature Materials*, 3(5):298–301, 2004.

Incropera, F. P. *Fundamentals of heat and mass transfer*. John Wiley, Hoboken, NJ, 2007.

in't Veld, P. J., Petersen, M. K., and Grest, G. S. Shear thinning of nanoparticle suspensions. *Physical Review E*, 79(2), 2009.

Inyushkin, A. V. Thermal conductivity of isotopically modified silicon: Current status of research. *Inorganic Materials*, 38(5):427–433, 2002.

Jaksic, N. A nanotechnology experiment for undergraduate engineering programs: Carbon nanotube production using electric discharge machining. In *ASEE Annual Conference and Exposition, Conference Proceedings*, Pittsburg, PA, United States, 2008.

Jayaraman, P., Lohani, V., Bradley, G., Dooley, J., and Griffin, O. Enhancement of an engineering curriculum through international experiences. In *ASEE Annual Conference and Exposition, Conference Proceedings*, Pittsburg, PA, United States, 2008.

Jiang, J. W., Lan, J. H., Wang, J. S., and Li, B. W. Isotopic effects on the thermal conductivity of graphene nanoribbons: Localization mechanism. *Journal of Applied Physics*, 107 (5):054314, 2010.

Jobic, H., Smirnov, K. S., and Bougeard, D. Inelastic neutron scattering spectra of zeolite frameworks - Experiment and modeling. *Chemical Physics Letters*, 344(1-2):147–153, 2001.

Johnson, R. A. and Oh, D. J. Analytic embedded atom method model for BCC metals. *Journal of Material Research*, 4(5):1195–1201, 1989.

Jolley, K. and Gill, S. P. A. Modelling transient heat conduction in solids at multiple length and time scales: A coupled non-equilibrium molecular dynamics/continuum approach. *Journal of Computational Physics*, 228(19):7412–7425, 2009.

Jorgensen, W. L., Chandrasekhar, J., Madura, J. D., Impey, R. W., and Klein, M. L. Comparison of simple potential functions for simulating liquid water. *Journal of Chemical Physics*, 79(2):926–935, 1983.

Kalweit, M. and Drikakis, D. Coupling strategies for hybrid molecular-continuum simulation methods. In *Colloquium on Micro- and Nano-Scale Flows - Advancing the Engineering Science and Design*, Glasgow, Scotland, 2006.

Kalweit, M. and Drikakis, D. Multiscale methods for micro/nano flows and materials. *Journal of Computational and Theoretical Nanoscience*, 5(9):1923–1938, 2008.

Kapitza, P. L. The study of heat transfer in helium II. *Journal of Physics, USSR*, 4:181, 1941.

Kazan, M., Guisbiers, G., Pereira, S., Correia, M. R., Masri, P., Bruyant, A., Volz, S., and Royer, P. Thermal conductivity of silicon bulk and nanowires: Effects of isotopic composition, phonon confinement, and surface roughness. *Journal of Applied Physics*, 107 (8):083503, 2010.

Keblinski, P., Phillpot, S. R., Choi, S. U. S., and Eastman, J. A. Mechanisms of heat flow in suspensions of nano-sized particles (nanofluids). *International Journal of Heat and Mass Transfer*, 45(4):855–863, 2002.

Keeler, J. *Understanding NMR spectroscopy.* John Wiley and Sons Ltd., West Sussex, UK, 2005.

Khare, R., Keblinski, P., and Yethiraj, A. Molecular dynamics simulations of heat and momentum transfer at a solid-fluid interface: Relationship between thermal and velocity slip. *International Journal of Heat and Mass Transfer*, 49(19-20):3401–3407, 2006.

Kittel, C. *Introduction to Solid State Physics*. John Wiley & Sons, Hoboken, NJ, USA, 2005.

Klemens, P. G. The scattering of low-frequency lattice waves by static imperfections. *Proceedings of the Physical Society of London Section A*, 68(12):1113–1128, 1955.

Klemens, P. G. Thermal resistance due to point defects at high temperatures. *Physical Review*, 119(2):507–509, 1960.

Knott, T. W., Lohani, V. K., Griffin Jr, O. H., Loganathan, G. V., Ade, G. T., and Wildman, T. M. Bridges for engineering education: Exploring ePortfolios in engineering education at Virginia Tech. In *ASEE Annual Conference Proceedings*, Salt Lake City, UT, United States, 2004.

Knott, T. W., Lohani, V. K., Loganathan, G. V., Adel, G. T., Wolfe, M. L., Paretti, M. C., Mallikarjunan, K., Wildman, T. M., Muffo, J. A., and Griffin Jr, O. H. Using electronic portfolios in a large engineering program. In *ASEE Annual Conference and Exposition, Conference Proceedings*, Portland, OR, United States, 2005.

Kremer, R. K., Graf, K., Cardona, M., Devyatykh, G. G., Gusev, A. V., Gibin, A. M., Inyushkin, A., Taldenkov, A., and Pohl, H. J. Thermal conductivity of isotopically enriched Si-28: Revisited. *Solid State Communications*, 131(8):499–503, 2004.

Krotenko, V. T., Dorosh, A. K., Ivanitskii, P. G., Bulavin, L. A., Slisenko, V. I., and Vasilkevich, A. A. Neutron studies of self-diffusion of water molecules in electrolyte solutions. *Journal of Structural Chemistry*, 33(1):64, 1992.

Kulkarni, A. J. and Zhou, M. Size-dependent thermal conductivity of zinc oxide nanobelts. *Applied Physics Letters*, 88(14):141921, 2006.

Lee, J. H., Galli, G. A., and Grossman, J. C. Nanoporous Si as an efficient thermoelectric material. *Nano Letters*, 8(11):3750–3754, 2008.

Lee, S.-J. J., Allen, E. L., and He, L. A "bottom-up" approach to engineering education in nanotechnology. In *Materials Research Society Symposium Proceedings*, San Francisco, CA, United States, 2006.

Lemmon, E., McLinden, M., and Friend, D. Thermophysical properties of fluid systems. *NIST Chemistry WebBook, http://webbook.nist.gov*, NIST Standard Reference Database Number 69, retrieved February 1, 2009.

Li, D. Y., Wu, Y., Fan, R., Yang, P. D., and Majumdar, A. Thermal conductivity of Si/SiGe superlattice nanowires. *Applied Physics Letters*, 83(15):3186–3188, 2003.

Li, L., Ungar, T., Wang, Y. D., Morris, J. R., Tichy, G., Lendvai, J., Yang, Y. L., Ren, Y., Choo, H., and Liaw, P. K. Microstructure evolution during cold rolling in a nanocrystalline Ni-Fe alloy determined by synchrotron X-ray diffraction. *Acta Materialia*, 57(17):4988–5000, 2009.

Libby, P. Heat and mass transfer at a general three-dimensional stagnation point. *AIAA Journal*, 5(3):507–517, 1967.

Liu, J., Chen, S. Y., Nie, X. B., and Robbins, M. O. A continuum-atomistic simulation of heat transfer in micro- and nano-flows. *Journal of Computational Physics*, 227(1):279–291, 2007.

Liu, J., Chen, S. Y., Nie, X. B., and Robbins, M. O. A continuum-atomistic multi-timescale algorithm for micro/nano flows. *Communications in Computational Physics*, 4(5):1279–1291, 2008.

Lo, J., Lohani, V., and Griffin, O. Full implementation of a new format for freshman engineering course at Virginia Tech. In *ASEE Annual Conference and Exposition, Conference Proceedings*, Chicago, IL, United States, 2006.

Lohani, V., Mullin, J., Lo, J., and Griffin, H. Implementation of international activities in a freshman engineering course. In *2006 ASEE Global Colloquium on Engineering Education*, Rio de Janeiro, Brazil, 2006a.

Lohani, V. K. In Natarajan, R. and Anandakrishnan, M., editors, *XXI Century Priorities in Engineering Education*. Indian Society for Technical Education (ISTE), Macmillan Publishers India Ltd., New Delhi, India, 2010.

Lohani, V. K., Kachroo, P., Chandrachood, S., Zephirin, T., Loganathan, G. V., and Lo, J. L. Mechatronics experiment in a freshman year course. In *2006 International Conference on Engineering Education (iCEE06)*, Puerto Rico, 2006b.

Lohani, V. K., Castles, R., Lo, J., and Griffin, H. Tablet PC applications in a large engineering program. *Computers in Education Journal*, 18(1):52–63, 2008a.

Lohani, V. K., Delgoshaei, P., and Green, C. Integrating LABVIEW and realtime monitoring into engineering instruction. In *Proceedings of 2009 Annual Conference of ASEE*, Austin, TX, 2009a.

Lohani, V. K., Puri, I. K., Balasubramanian, G., Case, S. W., and Mahajan, R. L. Development and implementation of a nanotechnology module into a large freshman engineering course. In *Annual Conference of the American Society for Engineering Education*, Austin, TX, USA, 2009b.

Lohani, V. K., Wolfe, M., Wildman, T., Connor, J., Mallikarjunan, K., Avent, Y., and Morris, S. Reformulating general engineering and biological systems engineering at Virginia Tech. In *Proceedings of the NSF/IREE program*, 2009c.

Lohani, V., Castles, R., Lo, J., and Griffin, O. Tablet PC applications in a large engineering program. In *ASEE Annual Conference and Exposition, Conference Proceedings*, Honolulu, HI, United States, 2007.

Lohani, V., Castles, R., Johri, A., Spangler, D., and Kibler, D. Analysis of tablet PC based learning experiences in freshman to junior level engineering courses. In *ASEE Annual Conference and Exposition, Conference Proceedings*, Pittsburg, PA, United States, 2008b.

Lohani, V. K., Mallikarjunan, K., Wolfe, M. L., Wildman, T., Connor, J., Muffo, J., Lo, J., Knott, T. W., Loganathan, G. V., Goff, R., Chang, M., Cundiff, J., Adel, G., Agblevor, F., Gregg, M., Vaughan, D., Fox, E., Griffin, H., and Mostaghimi, S. Work in progress - Spiral

curriculum approach to reformulate engineering curriculum. In *Proceedings - Frontiers in Education Conference, FIE*, Indianapolis, IN, United States, 2005a.

Lohani, V. K., Sanders, M., Wildman, T., Connor, J., Mallikarjunan, K., Dillaha, T., Muffo, J., Knott, T. W., Lo, J., Loganathan, G. V., Adel, G., Wolfe, M. L., Goff, R., Gregg, M., Chang, M., Agblevor, F., Vaughan, D., Cundiff, J., Fox, E., Griffin, H., and Magliaro, S. From BEEVT to DLR- NSF supported engineering education projects at Virginia Tech. In *ASEE Annual Conference and Exposition, Conference Proceedings*, Portland, OR, United States, 2005b.

Lokotosh, T. V., Malomuzh, N. P., and Pankratov, K. N. Thermal motion in water plus electrolyte solutions according to quasi-elastic incoherent neutron scattering data. *Journal of Chemical and Engineering Data*, 55(5):2021–2029, 2010.

Lucy, L. B. Numerical approach to testing of fission hypothesis. *Astronomical Journal*, 82 (12):1013–1024, 1977.

Lukes, J. R., Li, D. Y., Liang, X. G., and Tien, C. L. Molecular dynamics study of solid thin-film thermal conductivity. *Journal of Heat Transfer-Transactions of the ASME*, 122 (3):536–543, 2000.

Lummen, N. and Kraska, T. Investigation of the formation of iron nanoparticles from the gas phase by molecular dynamics simulation. *Nanotechnology*, 15(5):525–533, 2004.

Majumdar, A. Nanoengineering: Promises and challenges. *Microscale Thermophysical Engineering*, 4(2):77–82, 2000.

Malani, A., Ayappa, K. G., and Murad, S. Effect of confinement on the hydration and solubility of NaCl in water. *Chemical Physics Letters*, 431(1-3):88–93, 2006.

Malani, A., Murad, S., and Ayappa, K. G. Hydration of ions under confinement. *Molecular Simulation*, 36(7-8):579–589, 2010.

Mark, P. and Nilsson, L. Structure and dynamics of the TIP3P, SPC, and SPC/E water models at 298 K. *Journal of Physical Chemistry A*, 105(43):9960, 2001.

Maruyama, S. and Kimura, T. A study on thermal resistance over a solid-liquid interface by the molecular dynamics method. *Thermal Science and Engineering*, 7(1):63–68, 1999.

Maruyama, S., Igarashi, Y., Taniguchi, Y., and Shiomi, J. Anisotropic heat transfer of single-walled carbon nanotubes. *Journal of Thermal Science and Technology*, 1(2):138–148, 2006.

Masoumi, N., Sohrabi, N., and Behzadmehr, A. A new model for calculating the effective viscosity of nanofluids. *Journal of Physics D-Applied Physics*, 42(5), 2009.

McCall, D. W. and Douglass, D. C. The effect of ions on the self-diffusion of water. I. Concentration dependence. *Journal of Physical Chemistry*, 69(6):2011, 1965.

Mendelev, M. I., Han, S., Srolovitz, D. J., Ackland, G. J., Sun, D. Y., and Asta, M. Development of new interatomic potentials appropriate for crystalline and liquid iron. *Philosophical Magazine*, 83(35):3977–3994, 2003.

Mendelson, M., Kuleck, G., Sanny, J., Bulman, J., Roe, J., Ula, N., Noorani, R., and Stupar, J. Teaching and evaluating a new nanotechnology undergraduate course. In *ASEE Annual Conference Proceedings*, Salt Lake City, UT, United States, 2004.

Mingo, N., Stewart, D. A., Broido, D. A., and Srivastava, D. Phonon transmission through defects in carbon nanotubes from first principles. *Physical Review B*, 77(3):033418, 2008.

Mishin, Y., Mehl, M. J., and Papaconstantopoulos, D. A. Phase stability in the Fe-Ni system: Investigation by first-principles calculations and atomistic simulations. *Acta Materialia*, 53 (15):4029–4041, 2005.

Mitin, V., Vagidov, N., and Liu, X. Developing a lab course in nanotechnology for undergraduate engineering students. In *ASEE Annual Conference and Exposition, Conference Proceedings*, Pittsburg, PA, United States, 2008.

Mizan, T. I., Savage, P. E., and Ziff, R. M. Molecular dynamics of supercritical water using a flexible SPC model. *The Journal of Physical Chemistry*, 98(49):13067–13076, 1994.

Morelli, D. T., Heremans, J. P., and Slack, G. A. Estimation of the isotope effect on the

lattice thermal conductivity of group IV and group III-V semiconductors. *Physical Review B*, 66(19):195304, 2002.

Moseler, M. and Landman, U. Formation, stability, and breakup of nanojets. *Science*, 289 (5482):1165–1169, 2000.

Mountain, R. D. Solvation structure of ions in water. *International Journal of Thermophysics*, 28(2):536–543, 2007.

Müller-Plathe, F. A simple nonequilibrium molecular dynamics method for calculating the thermal conductivity. *Journal of Chemical Physics*, 106(14):6082–6085, 1997.

Mullin, J., Lo, J., Griffin, O., and Lohani, V. Sustainable development design projects for engineering freshmen. In *ASEE Annual Conference and Exposition, Conference Proceedings*, Chicago, IL, United States, 2006a.

Mullin, J., Lohani, V. K., and Lo, J. Work in progress: Introduction to engineering ethics through student skits in the freshman engineering program at Virginia Tech. In *Proceedings - Frontiers in Education Conference, FIE*, San Diego, CA, United States, 2006b.

Mullin, J., Kim, J., Lohani, V., and Lo, J. Sustainable energy design projects for engineering freshmen. In *ASEE Annual Conference and Exposition, Conference Proceedings*, Honolulu, HI, United States, 2007.

Munetoh, S., Motooka, T., Moriguchi, K., and Shintani, A. Interatomic potential for Si-O systems using Tersoff parameterization. *Computational Materials Science*, 39(2):334–339, 2007.

Murad, S. and Puri, I. K. Nanoscale jet collision and mixing dynamics. *Nano Letters*, 7(3): 707–712, 2007a.

Murad, S. and Puri, I. K. Dynamics of nanoscale jet formation and impingement on flat surfaces. *Physics of Fluids*, 19:128102, 2007b.

Murad, S. and Puri, I. K. Molecular simulation of thermal transport across hydrophilic interfaces. *Chemical Physics Letters*, 467(1-3):110–113, 2008a.

Murad, S. and Puri, I. K. Thermal transport across nanoscale solid-fluid interfaces. *Applied Physics Letters*, 92(13):133105, 2008b.

Murad, S. and Puri, I. K. Thermal transport through a fluid-solid interface. *Chemical Physics Letters*, 476(4-6):267–270, 2009a.

Murad, S. and Puri, I. K. Thermal transport through superlattice solid-solid interfaces. *Applied Physics Letters*, 95(5):051907, 2009b.

Murakawa, A., Ishii, H., and Kakimoto, K. An investigation of thermal conductivity of silicon as a function of isotope concentration by molecular dynamics. *Journal of Crystal Growth*, 267(3-4):452–457, 2004.

Namburu, P. K., Kulkarni, D. P., Dandekar, A., and Das, D. K. Experimental investigation of viscosity and specific heat of silicon dioxide nanofluids. *Micro & Nano Letters*, 2(3): 67–71, 2007.

Nie, X. B., Chen, S. Y., E, W. N., and Robbins, M. O. A continuum and molecular dynamics hybrid method for micro- and nano-fluid flow. *Journal of Fluid Mechanics*, 500:55–64, 2004a.

Nie, X. B., Chen, S. Y., and Robbins, M. O. Hybrid continuum-atomistic simulation of singular corner flow. *Physics of Fluids*, 16(10):3579–3591, 2004b.

Nitzan, A. Chemistry - Molecules take the heat. *Science*, 317(5839):759–760, 2007.

N'Tsoukpoe, K. E., Liu, H., Le Pierres, N., and Luo, L. G. A review on long-term sorption solar energy storage. *Renewable & Sustainable Energy Reviews*, 13(9):2385–2396, 2009.

Obst, S. and Bradaczek, H. Molecular dynamics study of the structure and dynamics of the hydration shell of alkaline and alkaline-earth metal cations. *Journal of Physical Chemistry*, 100(39):15677–15687, 1996.

Oconnell, S. T. and Thompson, P. A. Molecular dynamics-continuum hybrid computations: A tool for studying complex fluid flows. *Physical Review E*, 52(6):R5792–R5795, 1995.

Ohara, T. Contribution of intermolecular energy transfer to heat conduction in a simple liquid. *Journal of Chemical Physics*, 111(21):9667–9672, 1999.

Ohara, T. and Suzuki, D. Intermolecular energy transfer at a solid-liquid interface. *Microscale Thermophysical Engineering*, 4(3):189–196, 2000.

Oostenbrink, C., Villa, A., Mark, A. E., and Van Gunsteren, W. F. A biomolecular force field based on the free enthalpy of hydration and solvation: The GROMOS force-field parameter sets 53A5 and 53A6. *Journal of Computational Chemistry*, 25(13):1656–1676, 2004.

Pernot, G., Stoffel, M., Savic, I., Pezzoli, F., Chen, P., Savelli, G., Jacquot, A., Schumann, J., Denker, U., Monch, I., Deneke, C., Schmidt, O. G., Rampnoux, J. M., Wang, S., Plissonnier, M., Rastelli, A., Dilhaire, S., and Mingo, N. Precise control of thermal conductivity at the nanoscale through individual phonon-scattering barriers. *Nature Materials*, 9(6): 491–495, 2010.

Philibert, J. *Atom Movements : Diffusion and Mass Transport in Solids*. Editions de Physique, Les Ulis, France, 1991.

Plekhanov, V. G. Isotope effects in lattice dynamics. *Physics-Uspekhi*, 46(7):689–715, 2003.

Plimpton, S. Fast parallel algorithms for short-range molecular-dynamics. *Journal of Computational Physics*, 117(1):1–19, 1995.

Pollack, G. L. Kapitza resistance. *Reviews of Modern Physics*, 41(1):48–81, 1969.

Pop, E. Energy dissipation and transport in nanoscale devices. *Nano Research*, 3(3):147–169, 2010.

Poulikakos, D., Arcidiacono, S., and Maruyama, S. Molecular dynamics simulation in nanoscale heat transfer: A review. *Microscale Thermophysical Engineering*, 7(3):181–206, 2003.

Pozhar, L. A. Structure and dynamics of nanofluids: Theory and simulations to calculate viscosity. *Physical Review E*, 61(2):1432–1446, 2000.

Pozhar, L. A., Kontar, E. P., and Hu, M. Z. C. Transport properties of nanosystems: Viscosity of nanofluids confined in slit nanopores. *Journal of Nanoscience and Nanotechnology*, 2(2): 209–227, 2002.

Prasher, R., Phelan, P. E., and Bhattacharya, P. Effect of aggregation kinetics on the thermal conductivity of nanoscale colloidal solutions (nanofluid). *Nano Letters*, 6(7):1529–1534, 2006a.

Prasher, R., Song, D., Wang, J. L., and Phelan, P. Measurements of nanofluid viscosity and its implications for thermal applications. *Applied Physics Letters*, 89(13), 2006b.

Puri, I. K. and Seshadri, K. Extinction of diffusion flames burning diluted methane and diluted propane in diluted air. *Combustion and Flame*, 65(2):137–150, 1986.

Raju, V. and Muthuswamy, P. Nanotechnology applications: Issues in implementing engineering technology curriculum. In *ASEE Annual Conference and Exposition, Conference Proceedings*, Portland, OR, United States, 2005.

Rao, A. M., Richter, E., Bandow, S., Chase, B., Eklund, P. C., Williams, K. A., Fang, S., Subbaswamy, K. R., Menon, M., Thess, A., Smalley, R. E., Dresselhaus, G., and Dresselhaus, M. S. Diameter-selective Raman scattering from vibrational modes in carbon nanotubes. *Science*, 275(5297):187–191, 1997.

Robson, V., Muffo, J., and Lohani, V. The little engineer that could: Background, attitudinal, and academic predictors of student success. In *Association for Institutional Research Annual Forum*, Chicago, IL, 2006.

Robson, V., Lohani, V. K., and Muffo, J. In Kelly, W. E., editor, *Assessment in Engineering Programs: Evolving Best Practices*. Association for Institutional Research, Tallahassee, FL, 2008.

Robson, V., Lohani, V., and Bateman, T. Foundational predictors of success in the collegiate engineering program. In *ASEE Annual Conference and Exposition, Conference Proceedings*, Honolulu, HI, United States, 2007.

Rodríguez Fernández-Alba, A. *Chromatographic-mass Spectrometric Food Analysis for Trace Determination of Pesticide Residues*. Elsevier, Boston, MA, USA, 2005.

Samvedi, V. and Tomar, V. The role of interface thermal boundary resistance in the overall thermal conductivity of Si-Ge multilayered structures. *Nanotechnology*, 20(36):365701, 2009.

Sanchez-Portal, D., Artacho, E., Soler, J. M., Rubio, A., and Ordejon, P. Ab initio structural, elastic, and vibrational properties of carbon nanotubes. *Physical Review B*, 59(19):12678–12688, 1999.

Sandhu, A. Nanofluid viscosity: Against the flow. *Nature Nanotechnology*, 2007.

Savic, I., Mingo, N., and Stewart, D. A. Phonon transport in isotope-disordered carbon and boron-nitride nanotubes: Is localization observable? *Physical Review Letters*, 101(16): 165502, 2008.

Sayle, R. A. and Milnerwhite, E. J. RASMOL - Biomolecular graphics for all. *Trends in Biochemical Sciences*, 20(9):374–376, 1995.

Sazonov, A. M., Olevskii, V. M., Porai-Koshits, A. B., Skobolev, V. N., and Shmuilovich, G. A. Concentration dependence of the self-diffusion coefficients of water in electrolyte solutions. *Journal of Structural Chemistry*, 14(6):972, 1973.

Schelling, P. K., Phillpot, S. R., and Keblinski, P. Comparison of atomic-level simulation methods for computing thermal conductivity. *Physical Review B*, 65(14):144306, 2002.

Schelling, P. K., Phillpot, S. R., and Keblinski, P. Kapitza conductance and phonon scattering at grain boundaries by simulation. *Journal of Applied Physics*, 95(11):6082–6091, 2004.

Schlichting, H. *Boundary Layer Theory*. McGraw-Hill, New York, USA, 1968.

Schultz, F. S. Undergraduate nanoscience and nanotechnology programs at University of Wisconsin-Stout. In *2007 NSTI Nanotechnology Conference and Trade Show - NSTI Nanotech 2007, Technical Proceedings*, Santa Clara, CA, United States, 2007.

Sciortino, F., Geiger, A., and Stanley, H. E. Network defects and molecular mobility in liquid water. *Journal of Chemical Physics*, 96(5):3857–3865, 1992.

Sellan, D. P., Landry, E. S., Turney, J. E., McGaughey, A. J. H., and Amon, C. H. Size effects in molecular dynamics thermal conductivity predictions. *Physical Review B*, 81(21): 214305, 2010.

Shao, Q., Huang, L. L., Zhou, J., Lu, L. H., Zhang, L. Z., Lu, X. H., Jiang, S. Y., Gubbins, K. E., and Shen, W. F. Molecular simulation study of temperature effect on ionic hydration in carbon nanotubes. *Physical Chemistry Chemical Physics*, 10(14):1896–1906, 2008.

Shapter, J. G., Ford, M. J., Maddox, L. M., and Waclawik, E. R. Teaching undergraduates nanotechnology. *International Journal of Engineering Education*, 18(5):512–18, 2002.

Shapter, J. G., Hale, P., Maddox, L. M., Ford, M. J., and Waclawik, E. R. Teaching undergraduates nanotechnology. In *Materials Research Society Symposium Proceedings*, San Francisco, CA, United States, 2004.

Shin, H., Oschwald, M., Micci, M. M., and Yoon, W. Influence of thermodynamic state on nanojet break-up. *Nanotechnology*, 16(12):2838–2845, 2005.

Shin, H. H. and Yoon, W. S. Non-equilibrium molecular dynamics simulation of nanojet injection with adaptive-spatial decomposition parallel algorithm. *Journal of Nanoscience and Nanotechnology*, 8(7):3661–3673, 2008.

Shin, H. H., Suh, D., and Yoon, W. S. Non-equilibrium molecular dynamics of nanojet injection in a high pressure environment. *Microfluidics and Nanofluidics*, 5(4):561–570, 2008.

Shiomi, J. and Maruyama, S. Heat conduction of single-walled carbon nanotube isotope superlattice structures: A molecular dynamics study. *Physical Review B*, 74(15):155401, 2006.

Snyder, G. J. and Toberer, E. S. Complex thermoelectric materials. *Nature Materials*, 7(2): 105–114, 2008.

Stevens, R. J., Zhigilei, L. V., and Norris, P. M. Effects of temperature and disorder on thermal boundary conductance at solid-solid interfaces: Nonequilibrium molecular dynamics simulations. *International Journal of Heat and Mass Transfer*, 50(19-20):3977–3989, 2007.

Stewart, D. A., Savic, I., and Mingo, N. First-principles calculation of the isotope effect on boron nitride nanotube thermal conductivity. *Nano Letters*, 9(1):81–84, 2009.

Stillinger, F. H. and Weber, T. A. Computer simulation of local order in condensed phases of Silicon. *Physical Review B*, 31(8):5262–5271, 1985.

Stojanovic, N., Maithripala, D. H. S., Berg, J. M., and Holtz, M. Thermal conductivity in metallic nanostructures at high temperature: Electrons, phonons, and the Wiedemann-Franz law. *Physical Review B*, 82(7):075418, 2010.

Stuart, S. J., Tutein, A. B., and Harrison, J. A. A reactive potential for hydrocarbons with intermolecular interactions. *Journal of Chemical Physics*, 112(14):6472–6486, 2000.

Suryanarayana, C. Nanocrystalline materials. *International Materials Reviews*, 40(2):41–64, 1995.

Suryanarayana, C. and Koch, C. C. Nanocrystalline materials - Current research and future directions. *Hyperfine Interactions*, 130(1-4):5–44, 2000.

Swartz, E. T. and Pohl, R. O. Thermal-boundary resistance. *Reviews of Modern Physics*, 61 (3):605–668, 1989.

Tahan, C., Ricky, L., Zenner, G. M., Ellison, K. D., Crone, W. C., and Miller, C. A. Nanotechnology and society: A discussion-based undergraduate course. *American Journal of Physics*, 74(5):443–8, 2006.

Tan, Z. W., Wang, J.-S., and Gan, C. K. First-principles study of heat transport properties of graphene nanoribbons. *Nano Letters*, 11(1):214–219, 2011.

Tang, J. Y., Wang, H. T., Lee, D. H., Fardy, M., Huo, Z. Y., Russell, T. P., and Yang, P. D. Holey silicon as an efficient thermoelectric material. *Nano Letters*, 10(10):4279–4283, 2010.

Tang, Q. H. A molecular dynamics simulation: The effect of finite size on the thermal conductivity in a single crystal silicon. *Molecular Physics*, 102(18):1959–1964, 2004.

Tao, W. Q. and He, Y. L. Recent advances in multiscale simulations of heat transfer and fluid flow problems. *Progress in Computational Fluid Dynamics*, 9(3-5):150–157, 2009.

Tavman, I., Turgut, A., Chirtoc, M., Schuchmann, H., and Tavman, S. Experimental investigation of viscosity and thermal conductivity of suspensions containing nanosized ceramic particles. *Archives of Materials Science and Engineering*, 34(2):99–104, 2008.

Tersoff, J. New empirical approach for the structure and energy of covalent systems. *Physical Review B*, 37(12):6991–7000, 1988.

Tersoff, J. Modeling solid-state chemistry - Interatomic potentials for multicomponent systems. *Physical Review B*, 39(8):5566–5568, 1989.

Thome, J. R. The new frontier in heat transfer: Microscale and nanoscale technologies. *Heat Transfer Engineering*, 27(9):1–3, 2006.

van der Spoel, D., Lindahl, E., Hess, B., Groenhof, G., Mark, A. E., and Berendsen, H. J. C. GROMACS: Fast, flexible, and free. *Journal of Computational Chemistry*, 26(16): 1701–1718, 2005.

van Essen, V. M., Zondag, H. A., Gores, J. C., Bleijendaal, L. P. J., Bakker, M., Schuitema, R., van Helden, W. G. J., He, Z., and Rindt, C. C. M. Characterization of $MgSO_4$ hydrate for thermochemical seasonal heat storage. *Journal of Solar Energy Engineering-Transactions of the ASME*, 131(4):041014, 2009.

Vchirawongkwin, V., Rode, B. M., and Persson, I. Structure and dynamics of sulfate ion in aqueous solution - An ab initio QMCF MD simulation and large angle X-ray scattering study. *Journal of Physical Chemistry B*, 111(16):4150–4155, 2007.

Venerus, D. C., Buongiorno, J., Christianson, R., Townsend, J., Bang, I. C., Chen, G., Chung, S. J., Chyu, M., Chen, H. S., Ding, Y. L., Dubois, F., Dzido, G., Funfschilling, D., Galand, Q., Gao, J. W., Hong, H. P., Horton, M., Hu, L. W., Iorio, C. S., Jarzebski, A. B., Jiang,

Y. R., Kabelac, S., Kedzierski, M. A., Kim, C., Kim, J. H., Kim, S., McKrell, T., Ni, R., Philip, J., Prabhat, N., Song, P. X., Van Vaerenbergh, S., Wen, D. S., Witharana, S., Zhao, X. Z., and Zhou, S. Q. Viscosity measurements on colloidal dispersions (nanofluids) for heat transfer applications. *Applied Rheology*, 20(4), 2010.

Venkatasubramanian, R., Siivola, E., Colpitts, T., and O'Quinn, B. Thin-film thermoelectric devices with high room-temperature figures of merit. *Nature*, 413(6856):597–602, 2001.

Volz, S., Saulnier, J. B., Chen, G., and Beauchamp, P. Computation of thermal conductivity of Si/Ge superlattices by molecular dynamics techniques. *Microelectronics Journal*, 31 (9-10):815–819, 2000a.

Volz, S., Saulnier, J. B., Chen, G., and Beauchamp, P. Molecular dynamics of heat transfer in Si/Ge superlattices. *High Temperatures-High Pressures*, 32(6):709–714, 2000b.

Wagner, G., Flekkoy, E., Feder, J., and Jossang, T. Coupling molecular dynamics and continuum dynamics. In *Europhysics Conference on Computational Physics (CCP 2001)*, Aachen, Germany, 2001.

Wang, B. X., Zhou, L. P., and Peng, X. F. A fractal model for predicting the effective thermal conductivity of liquid with suspension of nanoparticles. *International Journal of Heat and Mass Transfer*, 46(14):2665–2672, 2003.

Wang, C. S., Chen, J. S., Shiomi, J., and Maruyama, S. A study on the thermal resistance over solid-liquid-vapor interfaces in a finite-space by a molecular dynamics method. *International Journal of Thermal Sciences*, 46(12):1203–1210, 2007a.

Wang, J. H. Effect of ions on the self-diffusion and structure of water in aqueous electrolytic solutions. *The Journal of Physical Chemistry*, 58(9):686–692, 1954.

Wang, X. Q. and Mujumdar, A. S. A review of nanofluids - Part I :Theoretical and numerical investigations. *Brazilian Journal of Chemical Engineering*, 25(4):613–630, 2008.

Wang, X. W., Xu, X. F., and Choi, S. U. S. Thermal conductivity of nanoparticle-fluid mixture. *Journal of Thermophysics and Heat Transfer*, 13(4):474–480, 1999.

Wang, Y., Jiang, W., Yan, T., and Voth, G. A. Understanding ionic liquids through atomistic and coarse-grained molecular dynamics simulations. *Accounts of Chemical Research*, 40 (11):1199, 2007b.

Wark, D. M. and Kohen, D. P. A spiral curriculum for hypnosis training. *American Journal of Clinical Hypnosis*, 45(2):119–128, 2002.

Werder, T., Walther, J. H., and Koumoutsakos, P. Hybrid atomistic-continuum method for the simulation of dense fluid flows. *Journal of Computational Physics*, 205(1):373–390, 2005.

Wijesinghe, H. S. and Hadjiconstantinou, N. G. A hybrid atomistic-continuum formulation for unsteady, viscous, incompressible flows. *CMES-Computer Modeling in Engineering & Sciences*, 5(6):515–526, 2004.

Winkelmann, K., Mantovani, J., and Brenner, J. A nanotechnology laboratory course for 1st year students. In *AIChE Annual Meeting, Conference Proceedings*, Cincinnati, OH, United States, 2005.

Wolfe, M., Wildman, T., Mallikarjunan, K., Lohani, V. K., and Connor, J. In Roy, R., editor, *Engineering Education: Perspectives, Issues and Concerns*. Shipra Publications, New Delhi, India, 2009.

Xue, L., Keblinski, P., Phillpot, S. R., Choi, S. U. S., and Eastman, J. A. Two regimes of thermal resistance at a liquid-solid interface. *Journal of Chemical Physics*, 118(1):337–339, 2003.

Xue, L., Keblinski, P., Phillpot, S. R., Choi, S. U. S., and Eastman, J. A. Effect of liquid layering at the liquid-solid interface on thermal transport. *International Journal of Heat and Mass Transfer*, 47(19-20):4277–4284, 2004.

Yang, N., Zhang, G., and Li, B. W. Ultralow thermal conductivity of isotope-doped silicon nanowires. *Nano Letters*, 8(1):276–280, 2008a.

Yang, Y. W., Liu, X. J., and Yang, J. P. Nonequilibrium molecular dynamics simulation for size effects on thermal conductivity of Si nanostructures. *Molecular Simulation*, 34(1): 51–55, 2008b.

Yu, J. K., Mitrovic, S., Tham, D., Varghese, J., and Heath, J. R. Reduction of thermal conductivity in phononic nanomesh structures. *Nature Nanotechnology*, 5(10):718–721, 2010.

Zhang, G. and Li, B. W. Thermal conductivity of nanotubes revisited: Effects of chirality, isotope impurity, tube length, and temperature. *Journal of Chemical Physics*, 123(11): 114714, 2005.

Zhang, G. M. and Batra, R. C. Symmetric smoothed particle hydrodynamics (SSPH) method and its application to elastic problems. *Computational Mechanics*, 43(3):321–340, 2009.

Zhang, H., Lee, G., Fonseca, A., Borders, T., and Cho, K. Isotope effect on the thermal conductivity of graphene. *Journal of Nanomaterials*, 2010:537657, 2010.

Zhang, Q. Y., Chan, K. Y., and Quirke, N. Molecular dynamics simulation of water confined in a nanopore of amorphous silica. *Molecular Simulation*, 35(15):1215–1223, 2009.